

AERODYNAMIC FLOW CHARACTERIZATION OF MICRO AIR VEHICLES
USING FLOW VISUALIZATION METHODS

By

MICHAEL JON SYTSMA

A THESIS PRESENTED TO THE GRADUATE SCHOOL
OF THE UNIVERSITY OF FLORIDA IN PARTIAL FULFILLMENT
OF THE REQUIREMENTS FOR THE DEGREE OF
MASTER OF SCIENCE

UNIVERSITY OF FLORIDA

2006

Copyright 2006

by

Michael J Sytsma

To my parents.

ACKNOWLEDGMENTS

I thank every person involved in my project. Special thanks go to Dr. Peter Ifju for supporting me and giving me this opportunity. I thank Dr. Louis Cattafesta and Dr. Bruce Carroll for the use of their equipment, and for their guidance in experimental aerodynamics. I thank Dr. Jill Peterson for the use of one of her lasers.

I thank Ron Brown Sr. for his guidance in machining and fabrication. His help was instrumental in the creation of tens of gadgets and gismos necessary for my research. I thank Mike Braddock, the SAE and Mini Baja teams for their assistance in machining and fabrication. I thank Kyu-ho Lee for all his guidance in MAV technology. I thank *Sapphire* for giving me the will to work harder, may she rest in peace, and I thank *Sapphire II* for giving me a second chance.

Finally, I thank my parents for their amazing support through six long years of college. Their assistance and love has held me up through my decisions good and bad. You two are great and I owe you my success.

TABLE OF CONTENTS

	<u>page</u>
ACKNOWLEDGMENTS	iv
LIST OF TABLES	vii
LIST OF FIGURES	viii
ABSTRACT	xiv
CHAPTER	
1 INTRODUCTION	1
Micro Air Vehicles	1
MAV Research	2
Motivation and Overview	3
2 LITERATURE SURVEY	5
3 WIND TUNNEL CHARACTERIZATION	11
Wind Tunnel Description	11
Test Section Description	12
Motor Description	13
Sting Balance and Mounting Arm Description	15
Wind tunnel control computer	16
Flow Characterization Experiment	16
Hot-wire Calibration	17
Data Sampling	21
Automatic data sampling	21
Data sampling hardware and settings	22
Post Processing	23
Results	25
Small test section results	25
Large test section results	28
Discussion of Error	25
Conclusions and Recommendations	31
Sting Balance Vibrational Analysis	32

4	WIND TUNNEL EXPERIMENTATION.....	51
	Overview of Experiments	51
	Loads Determination	51
	Flow Visualization.....	52
	Surface oil flow visualization.....	52
	Laser based flow visualization	53
	Overview	54
	Model Selection.....	54
	Loads Determination and Analysis.....	59
	Experimental Setup	60
	Loads Data.....	62
	Discussion of Loads Data.....	62
	Vibrational Exploration	64
	Selection of AOAs of Interest	66
	Oil Surface Flow Visualization	66
	Experimental Setup	67
	Results and Discussion.....	69
	Discussion of Results	71
	Laser Based Flow Visualization	71
	Basic Experimental Setup.....	71
	Continuous Laser Flow Visualization	72
	Rigid wing chord wise visualization	72
	Rigid wing span wise visualization.....	74
	Comparison of Rigid and PR Wings	82
	Pulsed Laser Visualization	84
	Particle image velocimetry.....	85
	Pulsed laser visualization	89
	Conclusions	89
5	CONCLUSION.....	119
	Wind Tunnel Survey Conclusion.....	119
	Flow Visualization Conclusion.....	119
	Future Work.....	120
APPENDIX		
A	HIGH SPEED WIND TUNNEL CHARACTERIZATION.....	124
	Small Test Section Results	124
	Large Test Section Results	127
	LIST OF REFERENCES.....	131
	BIOGRAPHICAL SKETCH	134

LIST OF TABLES

<u>Table</u>	<u>page</u>
4-1 Reasoning behind selection of AOAs of interest	91

LIST OF FIGURES

<u>Figure</u>	<u>page</u>
1-1 An 11.5 cm wingspan UF MAV.	4
1-2 Planform of rigid wing (A), BR wing (B), and PR wing (C).....	4
2-1 CFD model and grid, courtesy of Viieru.....	8
2-2 CFD streamlines prepared along center span location at a velocity of 10 m/s and AOA of 6° (A), and 15° (B), courtesy of Viieru.....	8
2-3 CFD Streamlines and pressure distributions at a velocity of 10 m/s and AOA of 6° (A), and 15° (B), courtesy of Viieru.....	9
2-4 CFD streamlines indicating growth of wingtip vortex size and strength at a velocity of 10 m/s and AOA of 6° (A), and 15° (B), courtesy of Viieru.....	9
2-5 PR wing effective airfoil 40 cm out from center span, wind tunnel velocities of 0 m/s (A), 10 m/s (B), 13 m/s (C), courtesy of Stanford [28].	10
2-6 BR wing effective airfoil 40cm out from center span, wind tunnel velocities of 0 m/s (A), 10 m/s (B), 13 m/s (C), courtesy of Stanford [28].	10
3-1 ELD Model 407B wind tunnel with small test section installed, photo reprinted with permission of ELD, Inc.	34
3-2 Large test section installed in wind tunnel loop, downstream of both plenum and straight walled diffuser.....	35
3-3 Wind tunnel control interface.....	35
3-4 Aerolab balance connected to angle arm in large test section with MAV wing model mounted.	36
3-5 Model arm for small test section constructed from 2.5 cm outer diameter steel tube.	36
3-6 Equipment structure, SCXI frame (top), servo motor and encoder (middle), servo control hardware and Heise (bottom), large test section (right).	37
3-7 Low profile jaw attached to model (left) and Aerolab balance (right).....	37

3-8	Coordinate system used for turbulence and velocity profile determination.....	37
3-9	VXI frame and computer showing data as it was being gathered automatically.	38
3-10	Wind tunnel traversing ceiling installed on top of small test section.....	38
3-11	Hot-wire probe mounted to probe holder inside small test section. Axial fan housing is visible through the window.....	39
3-12	Wind tunnel control voltage vs. wind tunnel origin velocity for small test section.....	39
3-13	Small (A) and large (B) test section hot-wire calibrations.....	40
3-14	PSD plots for 10 m/s (Channel 1) and 50 Ω terminator (Channel 3) data taken at the (0,0,0) point.	41
3-15	Centerline Global RMS and PSD Turbulence variation over different velocities for X = -1.22 m.....	41
3-16	Velocity contour across test section at X = 0 m. Black squares are data sampling locations.	42
3-17	RMS turbulence contour across small test section at X = 0 m. Black squares are data sampling locations.	42
3-18	Picture of probe holder extending through traverse ceiling brush seal.	43
3-19	Velocity contours across test section at X = -1.22 m location. Black squares are data sampling locations.	43
3-20	RMS turbulence contours across test section at X = -1.22 m location. Black squares are data sampling locations.	44
3-21	Centerline Global RMS and PSD Turbulence variation over different velocities at X locations.....	44
3-22	Mean velocity variation over X along centerline of large test section at a (0,0,0) velocity of 10 m/s.....	45
3-23	Turbulence variation over X along centerline of large test section at a (0,0,0) velocity of 10 m/s.....	45
3-24	Variation of velocity across Y direction for (0,0,0) velocity of 10 m/s, Z = 0.0 m, X = 0.0, -1.22 m.	46
3-25	Variation of global RMS turbulence across Y direction for (0,0,0) velocity of 10 m/s, Z = 0.0 m, X = 0.0, -1.22 m.....	46

3-26	Variation of velocity across Z direction for (0,0,0) velocity of 10 m/s, Y = 0.0 m, X = 0.0, -1.22 m.	47
3-27	Variation of global RMS turbulence across Z direction for (0,0,0) velocity of 10 m/s, Y = 0.0 m, X = 0.0, -1.22 m.	47
3-28	Variation of velocity across Y = Z direction for (0,0,0) velocity of 10 m/s, X = 0.0, -1.22 m.	48
3-29	Variation of global RMS turbulence across Y = Z direction for (0,0,0) velocity of 10 m/s, X = 0.0, -1.22 m.	48
3-30	Servo unit (right), axial spring (center), AOA encoder (top), and feed through to test section (left).	49
3-31	Vibrational analysis experimental setup with laser displacement sensor (left) and shaker (right).	49
3-32	PSD plot for vibration of tip of balance with and without model.	50
4-1	ProEngineer rendering of model having LAR Zimmerman planform.	91
4-2	Plot of normalized airfoil used on 2004 competition MAVs.	91
4-3	Planform of rigid wing (A), BR wing (B), and PR wing (C).	92
4-4	MAV rigid wing model with sting mount attached and edges sanded.	92
4-5	Variation of lift coefficient over AOA at origin velocity of 10 m/s.	93
4-6	Variation of drag coefficient over AOA at origin velocity of 10 m/s.	93
4-7	Variation of moment coefficient over AOA at origin velocity of 10 m/s.	94
4-8	Lift vs. drag coefficient at origin velocity of 10 m/s.	94
4-9	Power spectral density plot of strain gage signal (black) and baseline signal (blue) at an AOA of 18° and wind tunnel velocity of 10 m/s.	95
4-10	Average power of predominant modes at V = 10 m/s.	95
4-11	Oil surface flow visualization of wing at AOA of 0° and wind tunnel velocity of 10 m/s.	96
4-12	Oil surface flow visualization of wing at A) AOA of 5° and B) AOA of 10° and wind tunnel velocity of 10 m/s.	96
4-13	Oil surface flow visualization of wing at AOA of 16° and wind tunnel velocity of 10 m/s.	97

4-14	Oil surface flow visualization of wing at A) AOA of 18.4° and B) AOA of 21° and wind tunnel velocity of 10 m/s.	97
4-15	Oil surface flow visualization of wing at A) AOA of 23° and B) AOA of 30° and wind tunnel velocity of 10 m/s.	98
4-16	Diagram of span wise laser flow visualization setup.	98
4-17	Diagram of chord wise laser flow visualization setup.	99
4-18	Diagram of chord wise visualization with laser sheet directed at very TE of wing.	99
4-19	Line seeder apparatus inside large test section.	100
4-20	View of camera in small test section looking from perspective of seeder.	100
4-21	Images of vortex evolution for a rigid wing with a wind tunnel velocity of 10 m/s, AOA = 0° (A), 5° (B), 10° (C), 16° (D), 18.5° (E), 18.9° (F), 21° (G), 23° (H), 30° (I).	101
4-22	Gathering accurate AOA measurement before taking pictures. Camera is top right, and laser sheet is on minimum dispersion and full power. Photo courtesy Bob Bird.	102
4-23	Flow visualization mosaic of center span of wing at a wind tunnel velocity of 10 m/s, AOA = 0°.	103
4-24	Flow visualization mosaic of center span of wing at a wind tunnel velocity of 10 m/s, AOA = 5°.	104
4-25	Flow visualization mosaic of center span of wing at a wind tunnel velocity of 10 m/s, AOA = 10°.	105
4-26	Flow visualization mosaic of center span of wing at a wind tunnel velocity of 10 m/s, AOA = 16°.	106
4-27	Flow visualization mosaic of center span of wing at a wind tunnel velocity of 10 m/s, AOA = 18.4°.	107
4-28	Flow visualization mosaic of center span of wing at a wind tunnel velocity of 10 m/s, AOA = 18.8°.	108
4-29	Flow visualization mosaic of center span of wing at a wind tunnel velocity of 10 m/s, AOA = 21°.	109
4-30	Flow visualization mosaic of center span of wing at a wind tunnel velocity of 10 m/s, AOA = 22°.	110

4-31	Flow visualization mosaic of center span of wing at a wind tunnel velocity of 10 m/s, AOA = 23°.....	111
4-32	Flow visualization mosaic of center span of wing at a wind tunnel velocity of 10 m/s, AOA = 25°.....	112
4-33	Flow visualization mosaic of center span of wing at a wind tunnel velocity of 10 m/s, AOA = 30°.....	113
4-34	Image of LE of wing indicating decreasing downward slope of LE toward wing tips.....	114
4-35	Diagram of laser sheet directed 40 mm from center span location.....	114
4-36	Leading edge visualizations of rigid wing (left column) and PR wing (right column) visualizations 40 mm out from center span at V = 10 m/s and AOA of 10° (A,B), 12° (C,D), 14° (E,F), 16° (G, H), 18° (I, J), 20° (K, L).....	115
4-37	Velocity ratio contours for rigid (A), BR (B), and PR (C) wings at AOA of 15° and wind tunnel velocity of 10 m/s. Images obtained 40 mm from center span of wing.....	116
4-38	Streamlines generated in Matlab superimposed on top of images gathered using PIV camera. Images are rigid (A), BR (B), and PR (C) wings at AOA of 15° and wind tunnel velocity of 10 m/s. Images obtained 40 mm from center span of wing.....	117
4-39	Pulsed laser flow visualization of rigid (A) and PR (B) wings at AOA of 12° and V of 10 m/s.....	118
5-1	Lift and drag coefficient curves with characteristic flow regimes indicated.	122
5-2	Changes in air flow patterns along center span based off of laser based flow visualization. A) Long and bottom side separation, B) Long separation only, bottom side attached, C) Formation of short LE separation bubble which sheds turbulent wake, D) LE short bubble sheds detached turbulent wake, E) LE bubble is burst and flow is fully detached from surface.....	123
A-1	Centerline mean velocity variation across X.....	124
A-2	Centerline turbulence variation across X.....	125
A-3	Velocity contour across test section at X = 0 m and V = 51 m/s. Black squares are data sampling locations.	125
A-4	RMS turbulence contour across small test section at X = 0 m and V = 51 m/s. Black squares are data sampling locations.....	126

A-5	Velocity contour across test section at $X = -1.22$ m and $V = 51$ m/s. Black squares are data sampling locations.	126
A-6	RMS turbulence contour across small test section at $X = -1.22$ m and $V = 51$ m/s. Black squares are data sampling locations. Possible errors present in top corners.	127
A-7	Variation of velocity across Y direction for (0,0,0) velocity of 26 m/s, $Z = 0.0$ m, $X = 0.0, -1.22$ m	127
A-8	Variation of global RMS turbulence across Y direction for (0,0,0) velocity of 26 m/s, $Z = 0.0$ m, $X = 0.0, -1.22$ m.....	128
A-9	Variation of velocity across Z direction for (0,0,0) velocity of 26 m/s, $Y = 0.0$ m, $X = 0.0, -1.22$ m.	128
A-10	Variation of global RMS turbulence across Z direction for (0,0,0) velocity of 26 m/s, $Y = 0.0$ m, $X = 0.0, -1.22$ m.	129
A-11	Variation of velocity across $Y = Z$ direction for (0,0,0) velocity of 26 m/s, $X = 0.0, -1.22$ m.	129
A-12	Variation of global RMS turbulence across $Y = Z$ direction for (0,0,0) velocity of 26 m/s, $X = 0.0, -1.22$ m.	130

Abstract of Thesis Presented to the Graduate School
of the University of Florida in Partial Fulfillment of the
Requirements for the Degree of Master of Science

AERODYNAMIC FLOW CHARACTERIZATION OF MICRO AIR VEHICLES
USING FLOW VISUALIZATION METHODS

By

Michael Jon Sytsma

August 2006

Chair: Peter Ifju

Cochair: Bruce Carroll

Major Department: Mechanical and Aerospace Engineering

Micro Air Vehicles (MAVs) are a very interesting field to those who study aerodynamics because of their intrinsic low aspect ratio and low Reynolds number wings. The flow effects have been extensively studied to the extent of loads determination, computational fluid dynamics (CFD) analysis, and dynamic deformations. Many MAV vehicles have been designed showing different technological innovations, and several MAV designs have been sold and are in mass production. The exact characteristics of air flow over University of Florida's (UF's) MAV wings, however, has not received so much attention. Significant efforts have been made to model UF MAV aerodynamics using CFD methods, but little effort has been applied to detailed experimental flow determination.

UF's Mechanical and Aerospace Engineering (MAE) department has recently acquired a low speed, low turbulence wind tunnel. A flow characterization experiment

was performed in the tunnel to determine its velocity and turbulence profiles for two speeds of interest, and with two test sections. The tunnel had centerline turbulence levels less than 0.1% in the small test section and 0.2% in the large test section. The boundary layer present on the large test section reduced its core flow area to nearly the same size as the small test section, making it less useful for testing large models. The small test section would be the best one to use for MAV research.

An investigation of MAV wings using qualitative flow visualization techniques was performed on rigid, batten reinforced (BR), and perimeter reinforced (PR) wing only models. This investigation was intended to guide future quantitative research. The flow separation behavior around a rigid wing was determined using oil surface and laser sheet flow visualization methods. The rigid wing was shown to have long laminar separation off a position of high camber at low angles of attack (AOA), and as AOA increased a leading edge (LE) short separation bubble formed. The LE bubble appeared to decrease drag and change the pitching moment of the wing. Comparisons between the PR and rigid wing showed that the PR wing had a LE bubble which formed at lower AOA than the rigid wing. Two dimensional particle image velocimetry (PIV) analysis was performed on all three wings and highlighted differing pressure profiles. It was realized that three dimensional PIV will be necessary to determine accurate pressure distributions.

The visualizations showed that UF MAV wings are not designed as efficiently as they could be. There remains room for improvement in separation control and stability analysis with separation in mind. Furthermore, separation behavior should be studied with the intent of creating smaller aircraft.

CHAPTER 1 INTRODUCTION

The rapid progress in the miniaturization of electronics has led to a multitude of possibilities. In the world of aircraft, electronics have brought the capability of removing a pilot from the aircraft entirely. Unmanned aerial vehicles (UAVs) have been of great value to the United States armed forces and as research vehicles. UAVs have shown a trend for reduced size over piloted aircraft. No longer bound to the needs of a mortal pilot, the designers of UAVs have the freedom of sizing the aircraft to suit the mission, not the crew.

It is advantageous from a cost perspective to create small aircraft due to the decreased cost of materials and manpower required for construction. Smaller aircraft also have a greater maneuverability, and they require shorter runways for takeoff and landing. The miniaturization of autopilot systems has created the ability to control a complex aircraft using a very small amount of electrical power and space. Small aircraft pose less of a damage liability in the case of a crash in domestic arenas, and they are less of a financial and human loss in military arenas. As such UAVs have become an important subset of aircraft [1, 2].

Micro Air Vehicles

Micro air vehicles (MAVs) are defined as UAVs which have a maximum dimension limited to 15.2 cm and maximum flight speeds on the order of 15 m/s. In order to achieve a maximum payload within the given size constraints, wing surface area must be maximized. Maximizing the wing area also decreases wing loading and tends to

increase flight duration. Maximization of wing area given dimensional constraints leads to a circular shape which yields most area for a given maximum dimension [3, 4]. Such wings have very low aspect ratios (LARs).

MAVs are often designed as flying wings to remove the necessity of a horizontal stabilizer and its accompanying increase in vehicle length and weight. Flying wings require a reflexed airfoil which generates a zero pitching moment under flight [4]. The reflex of an airfoil is the trailing edge curvature beneath the mean chord line which creates negative lift in the area and opposes the pitching moment of the wing. Successful MAV aircraft have been configured as tractor or pusher configurations, and the whole slew of geometric design variables have been used.

The specific design constraints of a MAV favor a LAR reflexed wing [3, 5]. The University of Florida's (UF's) MAV Team has used a LAR reflexed wing in several International Micro Air Vehicle Competitions (IMAVCs) with great success [3, 4, 5]. The IMAVC is a yearly event in which university teams and individuals design mission-specific MAVs and compete in several competitions. The IMAVC rules favor the minimization of aircraft dimensions and successful completion of each mission, and the UF MAV Team has won first place in this competition eight times. An 11.5 cm wingspan MAV used in the 2005 IMAVC is shown in Figure 1-1.

MAV Research

A significant body of work has been published on the properties of MAV wings and aircraft. Early studies on MAVs illuminated the basic characteristics of low Reynolds number (Re) flows [6]. MAV wings of varying geometries have been extensively studied using computational fluid dynamics (CFD) modeling, and MAV wings and aircraft have also been subject to extensive wind tunnel testing [4, 7, 8, 9].

The inherent deforming design of the UF MAV has led to studies of the deformation under flight and the development of wings with enhanced lifting properties [7]. The UF MAV wing design which was used in the IMAVC [3, 4, 5] was studied extensively by Albertani [7] using loads and displacement analysis, however no recent research has focused on the experimental aerodynamic flow properties of the UF MAV wing design.

Motivation and Overview

The UF Mechanical and Aerospace Engineering (MAE) Department has recently acquired a low-speed low-turbulence wind tunnel from Engineering Laboratory Design Corporation. The wind tunnel will be used for future work on MAVs and other projects, and hence the flow field of the tunnel turbulence and velocity field must be sufficiently characterized for it to yield useful results. The characterization of the wind tunnel will represent the first portion of this thesis.

Research into the loads characteristics of UF's perimeter reinforced (PR) wing showed that it differed in its loading behavior from a batten reinforced (BR) or rigid wing. The three wing types are shown in Figure 1-2. The PR wing was shown by Albertani to have enhanced lifting capabilities and handling characteristics at low speeds [3, 7]. Unpublished CFD performed by Viieru showed separation behavior on the top and bottom sides of a wing only model. The CFD results also highlighted behavior of the wing tip vortices. It was of interest to study the experimental flow characteristics of the different types of UF MAV wings in an attempt to determine why they behaved differently. It was also interesting to determine how well the CFD data compared to actual experimental results.

The second chapter of this thesis will be an overview of relevant MAV research. The third chapter of this thesis will present a hot-wire turbulence and velocity analysis of

the wind tunnel flow field and a vibrational characterization of the model arm and sting balance. The fourth chapter will detail the experiments performed on representative MAV wings and their results. The fifth chapter will present conclusions and offer recommendations about future MAV research.

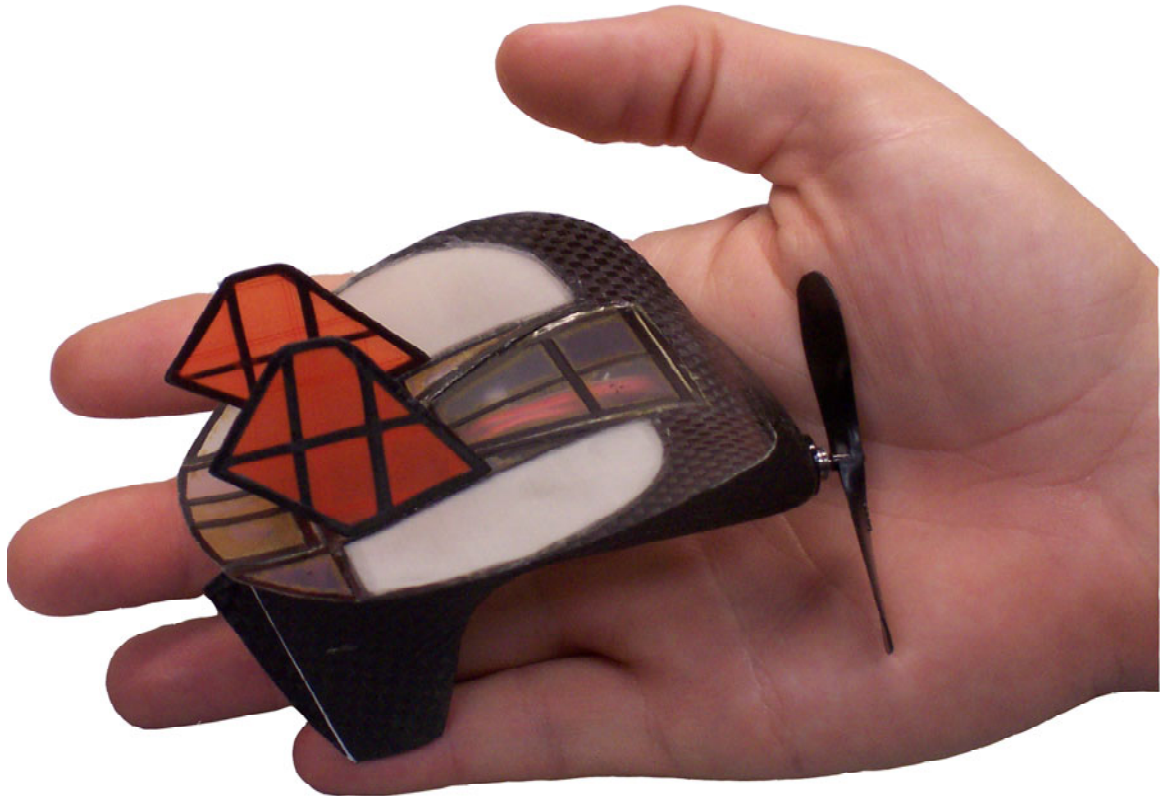


Figure 1-1. An 11.5 cm wingspan UF MAV.

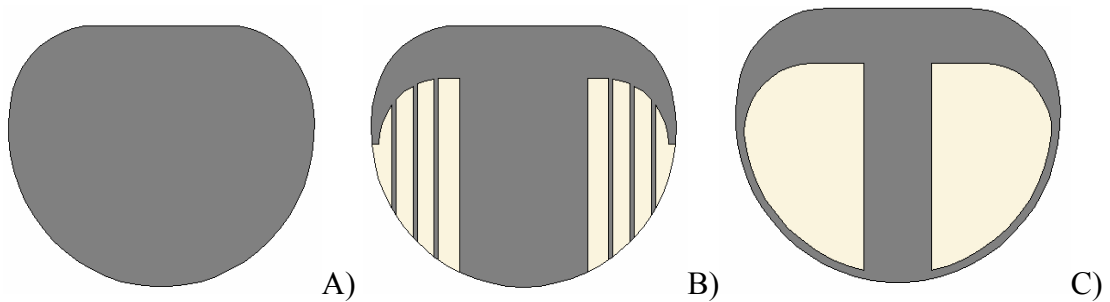


Figure 1-2. Planform of rigid wing (A), BR wing (B), and PR wing (C).

CHAPTER 2 LITERATURE SURVEY

Early work on the aerodynamic characteristics of micro air vehicle (MAV) wings by Carmichael shows that MAVs operating in the Reynolds number (Re) range from 70,000 to 200,000 can benefit from the low drag induced from laminar flows provided that laminar separation does not occur [6]. Laminar separation occurs when flow with a laminar boundary layer encounters an adverse pressure gradient of sufficient strength to cause separation [6,10,11,12]. On a low Re wing laminar separation effects can cause a phenomenon known as a laminar or transitional separation bubble. The terms laminar and transitional are used interchangeably in the literature regarding low Re separation bubbles, and for the remainder of this thesis will only be referred to as laminar separation bubbles, separation bubbles, or just bubble. A separation bubble is formed when the laminar separation creates a laminar free shear layer which acts as a dividing streamline. The laminar shear layer transitions from a laminar to a turbulent nature and the resulting momentum mixing causes the flow to reattach in a turbulent boundary layer [1,11]. The flow above the shear layer travels at a high velocity, while the recirculation flow below is of a much lower velocity.

Two types of laminar bubbles have been categorized by researchers, a ‘short’ and a ‘long’ bubble. The long bubble has separated flow over much of the airfoil, often beginning at a position of high camber and ending near the TE. The long bubble is often defined as covering 15% to 45 % of the chord or more [1]. Long bubbles may not reattach in the case of very low Re because the transition to turbulence does not occur

quickly enough to cause turbulent reattachment [2,13]. The short bubble is often formed off the LE and is usually on the order of 2 % to 3% of the chord in length. The short bubble tends to be formed at higher angle of attack (AOA) and lift coefficient while the long bubble typically exists for moderate AOA and lift coefficient [8,12].

The length of the two types of bubbles are generally linearly proportional to their thickness, and increasing turbulence levels in the tunnel tends to decrease bubble thickness [9, 10]. The bubble behavior is inherently unsteady, and in some cases the flow will have an oscillatory reattachment behavior [12]. The long and short bubbles are typically characterized by a constant pressure distribution applied along the airfoil [10,12]. The formation of the separation bubbles are path dependent, hence significant hysteresis in the lift curve will often exist for low Re airfoils [11].

Unlike traditional airfoil theory in which an airfoil may be expected to have similar non-dimensional pressure fields at high Re, a low Re wing with laminar separation bubbles can be expected to have vastly different pressure fields fully dependent on Re and path [10]. Traditional methods at creating flow turbulence such as trip strips and surface grit have proven effective at reducing separation drag at Re over 100,000, however below a Re of 30,000 turbulators have low effectiveness [11, 14, 15]. The Re range between the two values is an area where drag reductions are possible, but hysteresis effects may increase drag [2]. Most of the studies above involved 2D airfoils which had thicknesses of 4 % or greater. The University of Florida (UF) MAV wing design, however, is a low aspect ratio (AR), fully three dimensional (3D) wing. The wing's thickness is about 0.3 % due to its single surface undercambered plate design.

Unpublished computational fluid dynamics (CFD) studies performed by Dragos Viieru at UF showed laminar separation behavior of very thin MAV wings [Information obtained through personal communication]. A moving grid, 3D, unsteady, incompressible Navier-Stokes solver was used with laminar and turbulence modeling to simulate the airflow over a MAV wing. Figure 2-1 is a graphic showing the grid and model used by the solver. The design of the wing was identical to wings built for International MAV Competitions (IMAVC's), and it was modeled as rigid.

The wing had recirculation effects as shown in Figure 2-2. The CFD results showed that at low AOA the flow on the bottom side of the wing is recirculating. It also appeared that a recirculating region reminiscent of a long separation bubble was present on the top side of the wing extending from the mid-chord to an attachment point not quite all the way to the trailing edge (TE). CFD analysis performed on a different model with a higher AR showed that the recirculation effects were only present on the inboard portions of the wing (Figure 2-3). The pressure distribution over the surface of the wing was also presented in Figure 2-3, and it was shown that the wing tip vortices cause extra lift due to the low pressure they apply at the wing tips. The size and strength of the wing tip vortices was also shown to increase as AOA increased [8, 16] (Figure 2-5).

UF MAVs are built with both rigid and flexible wings. It was shown that a flexible wing greatly reduces a pilot's workload and aids in gust suppression [3, 4, 5]. Such factors are very important for the fielding of an effective and reliable MAV [4]. Loads wind tunnel tests highlighted enhanced lifting capabilities of the perimeter reinforced (PR) wing over a conventional batten reinforced (BR) or rigid wing [7]. Visual image correlation methods allowed Bret Stanford to obtain 3-D deformation maps of the flexible

wings under load [personal correspondence, UF 2006]. Figure 2-5 shows the changing shape of the effective airfoil of the PR wing under increasing loading and AOA. Figure 2-6 shows that the BR wing maintains its airfoil shape but is subject to rotation.

The previous research into the UF MAV designs served as motivation to determine the airflow properties through experimental methods in the newly installed wind tunnel. Experiments were tailored to address issues raised by previous UF MAV research such as separation type and location, and the nature of the wing tip vortices. The difference in flow properties between a rigid and PR wing were also investigated in an attempt to explain the different loading properties.

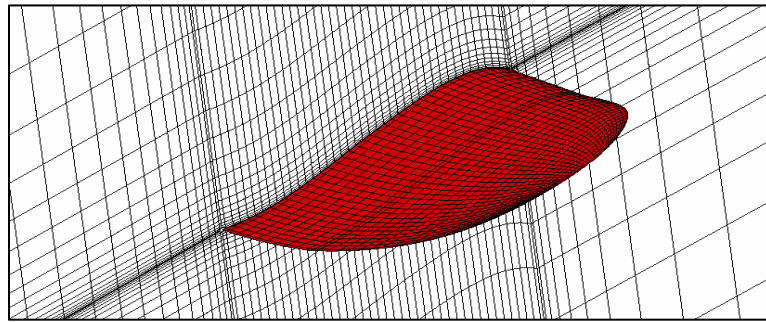


Figure 2-1. CFD model and grid, courtesy of Viieru.

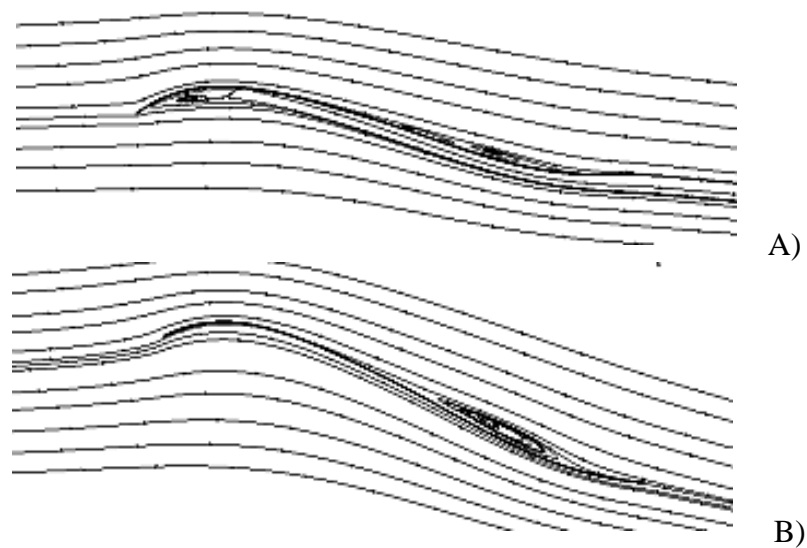


Figure 2-2. CFD streamlines prepared along center span location at a velocity of 10 m/s and AOA of 6° (A), and 15° (B), courtesy of Viieru.

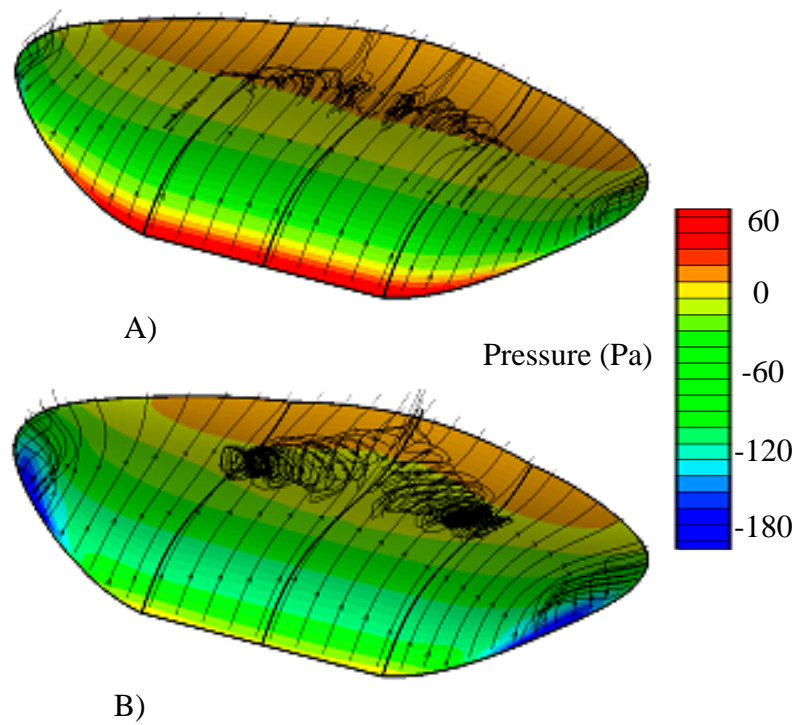


Figure 2-3. CFD Streamlines and pressure distributions at a velocity of 10 m/s and AOA of 6° (A), and 15° (B), courtesy of Viieru.

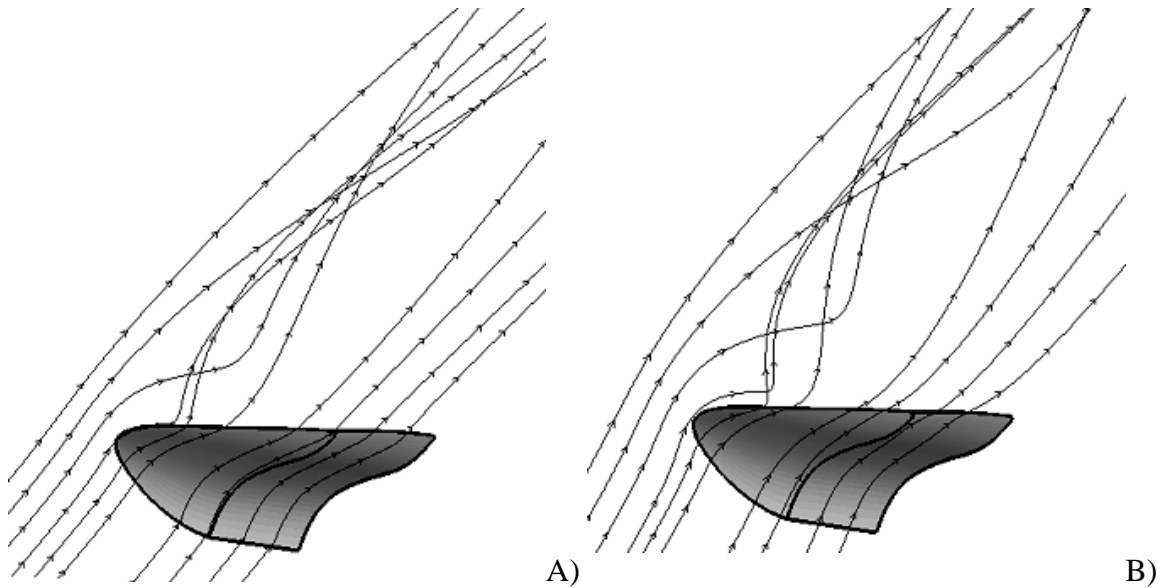


Figure 2-4. CFD streamlines indicating growth of wingtip vortex size and strength at a velocity of 10 m/s and AOA of 6° (A), and 15° (B), courtesy of Viieru.

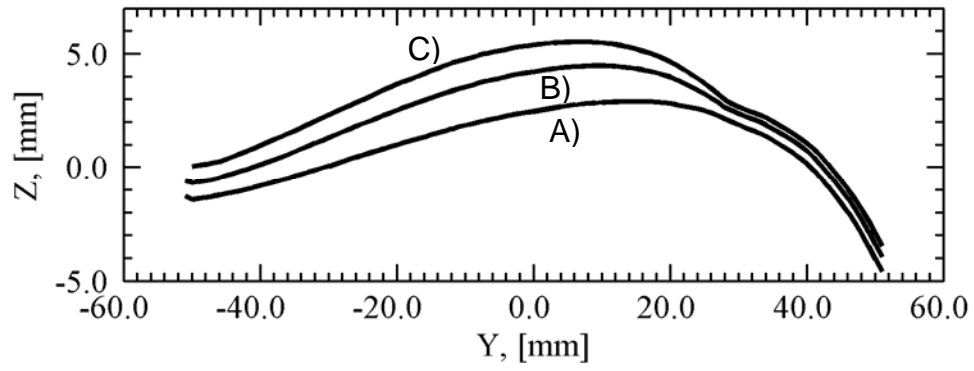


Figure 2-5. PR wing effective airfoil 40 cm out from center span, wind tunnel velocities of 0 m/s (A), 10 m/s (B), 13 m/s (C), courtesy of Stanford [28].

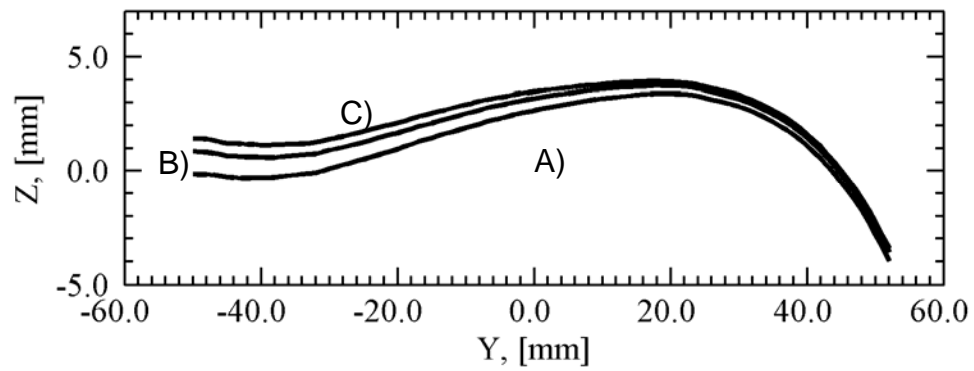


Figure 2-6. BR wing effective airfoil 40cm out from center span, wind tunnel velocities of 0 m/s (A), 10 m/s (B), 13 m/s (C), courtesy of Stanford [28].

CHAPTER 3 WIND TUNNEL CHARACTERIZATION

This chapter will detail the flow field characterization of the newly installed Engineering Laboratory Design (ELD) 407B wind tunnel. A single component hot-wire anemometer was used to find velocity profile information and determine the detailed turbulence profile for the tunnel. The vibrational characteristics of the sting balance and angle of attack (AOA) arm will also be discussed.

Wind Tunnel Description

The ELD model 407B wind tunnel is a recirculating type tunnel installed in room 125 of MAE-A, UF building 725 (Figure 3-1). The tunnel has two test sections which may be exchanged by changing the streamwise location of a straight walled diffuser. The ‘small’ test section has inner dimensions of 0.61 m x 0.61 m x 2.44 m and has listed velocity capability ranging from 3 m/s to 91.4 m/s. The small test section is installed downstream of the flow screens and plenum and is upstream of the straight walled diffuser. The ‘large’ test section has inner dimensions of 0.838 m x 0.838 m x 2.44 m and has listed velocity capability ranging from 2 m/s to 45 m/s. The large test section is installed by connecting the straight walled diffuser to the plenum and is downstream of both, as shown in Figure 3-2.

The 2 stage axial fan is driven by an in-line electric motor powered by three phase 440 V at 60 Hz. The motor is controlled by a Toshiba Model H7 variable frequency drive (VFD). The wind tunnel displaces a footprint of 10.6 m x 3.5 m, is 2.4 m high, and weighs 4227 kg.

Test Section Description

The two test sections are designed to be mated with different upper walls, or ceilings to suit multiple experiment types. One ceiling for the wind tunnel is a traversing 3 degree of freedom (DOF) ceiling controlled by stepper motors which allow instruments to be accurately placed in the flow field. The traversing ceiling was used to control the location of the hot-wire probe in the turbulence and velocity characterization experiment. The traverse has a resolution of 1575 steps per centimeter. The tunnel also has one 12.7 cm thick aluminum plate and one 9.5 cm thick framed optical glass window which are used as ceiling pieces. The pieces are designed to be placed atop the large test section and fit over the small test section. These ceiling pieces were used for the flow visualization experiments discussed later in this thesis. The last component is a variable area ceiling which fits atop the small test section only. The variable area ceiling could be used to apply pressure gradients to the flow, but its use will not be discussed in this thesis.

The horizontal sides of the test sections consist of two interchangeable panels per side. The panels on operator side are optical glass windows in frames and have gas cylinders and hinges allowing the windows to be raised and lowered easily. The other side panels consists of a 12.7 cm thick aluminum plate with a 10.2 cm hole centered to allow a model arm to pass through. The hole has a precision machined plate which fits in the hole to make the inner surface flush when necessary. The other panel is an optical glass window in a frame similar to the operator side windows, except it is unhinged without gas cylinders. The windows have latches which hold them down and keep them firm against foam rubber seals to prevent gas exchange. Each test section has its own separately sized side panels.

The floor of the test sections are also interchangeable plates. Each test section has two 2.54 cm thick clear acrylic sheets which act as the floor. Each test section also has a single 12.7 cm thick aluminum plate with a 30.5 cm hole and flush fitting cover plate for instrumentation and visibility.

Motor Description

The wind tunnel's in-line electric motor is designed to be cooled by air flowing through the tunnel. The tunnel has a heat exchanger installed downstream of the motor and upstream of the test section. Coolant fluid flow rate through the heat exchanger is set from a servo actuated control valve. The valve is adjusted by a thermal control unit connected to a thermocouple just downstream of the heat exchanger. The system adjusts coolant fluid flow rate to match a user's desired test section temperature. The documentation states that 150 liters a minute of 7° C water are required to maintain thermal control within the tunnel for all velocities.

The tunnel was not installed with dedicated water flow, so a garden hose connects a spigot and the control valve, and the bottom of the heat exchanger runs to a drain in the floor. The garden hose was issued an average flow rate of 20 liters a minute of 21° C water. This flow rate is incapable of maintaining a constant, safe temperature at higher tunnel speed settings, however the temperature varies by no more than 0.5° C when the tunnel is operated at the micro air vehicle (MAV) flight speeds of 6 m/s to 15 m/s. The fiberglass reinforced plastic (FRP) construction of the tunnel limits the maximum wind tunnel temperature to 60° C. Beyond this temperature the FRP will soften and damage may occur. However, the available cooling water flow is useful for reducing the tunnel temperature after short, high speed runs.

The wind tunnel motor is controlled by a VFD which outputs a constant frequency power signal between 1.5 and 60 Hz. The VFD and servo control valve are operated from a control box mounted on the plenum. The control panel of the wind tunnel is shown in Figure 3-3. The unit on left side of Figure 3-3 is the temperature control with desired (green) and current (red) temperatures shown. The unit on the right commands the VFD with a frequency input, currently set at 0.0 Hz. The panel accepts both manual frequency settings and a 0 V to 10V wind tunnel control voltage. The control panel determines the correct frequency to drive the motor at based off a linear scaling of the analog wind tunnel control voltage input.

Alternating current (ac) motors will spin at a constant velocity when supplied with a constant frequency, if not overloaded. It was hypothesized that a constant wind tunnel control voltage would yield a constant mean velocity, and a wind tunnel control VI was created in LabVIEW to test this hypothesis. Pressure measurements of velocity using a pitot-static probe showed that the measured velocity was nearly constant at a given wind tunnel control voltage. The VI was programmed to average one hundred measurements over a second and to output a standard deviation. Both test sections had a velocity standard deviation of 0.02 m/s, or less, for speeds corresponding to wind tunnel input voltages ranging from 0.4 V to 7 V. The wind tunnel motor operates poorly at very low speeds and often trips its internal circuit breaker. The wind tunnel temperature rises rapidly, as fast as 15° C a minute, at high speeds indicating a rapid density change that could not register quickly enough on the installed thermocouple or added RTD to allow for accurate velocity determination. As such there are errors inherent in the pressure based velocity computation at high speeds.

Sting Balance and Mounting Arm Description

The wind tunnel also has a 6 component sting balance produced by Aerolab. The balance is an Aerolab model 01-15 and is suitable for testing MAVs (Figure 3-4). The balance has been calibrated to be sensitive enough to detect the minimum loads produced by MAVs, for example drag was calibrated down to 0.01 N, about 40 % of the very minimum drag expected from a MAV [7]. The balance is connected to a National Instruments (NI) SCXI 1000 frame with several data acquisition modules installed. The modules serve to control the wind tunnel fan motor, the angle of attack arm for positioning the sting balance, and read the strain gage voltages off the balance. A detailed description of the balance and data acquisition system, including sensitivity and accuracy analysis, is provided by Albertani [7].

The balance is mounted on a custom fabricated low profile arm within the wind tunnel. A separate arm has been fabricated for the small and large test sections. The arm curves well behind the model in an attempt to affect the airflow as little as possible. The arm for the small test section is 60 cm behind a model's position while the arm for the large test section is 70 cm behind the model. The location of the model may also be adjusted along slots in the model arm. The large test section setup is shown in Figure 3-4, and the arm for the small test section is shown in Figure 3-5. The arm extends through the hole in the side of the test section to a servo system mounted on a structure (Figure 3-6). The structure contains the SCXI frame, servo unit and control hardware. A Heise model PM differential pressure transducer rated at 12.7 cm and 127 cm of water, with a ± 0.002 % sensitivity and a ± 0.01 % repeatability, is also mounted onto the frame. The Heise is used to report the pressure difference from a pitot-static tube, and the pressure tubes are connected to both modules. With both modules, the Heise can report velocities

up to 45 m/s. A Net Scanner absolute pressure transducer rated at 254 cm of water with a ± 0.05 % full scale system accuracy is used to report higher velocities.

The wind tunnel models are mounted to the sting balance via a low profile jaw arrangement (Figure 3-7). If necessary the sting balance may be removed and replaced with a dummy balance which is a rod of stainless steel the size and length of the actual balance. Due to the geometry of the model arms the maximum AOA possible with the small test section is 38° , and 52° with the large test section.

Wind tunnel control computer

The wind tunnel is controlled by a Dell Precision 650 dual processor Xeon 3.06 GHz computer. The computer is responsible for interfacing with the SCXI frame, Heise, test section ceiling traverse, and any other laboratory equipment necessary for an experiment. The computer has LabVIEW and Matlab installed. LabVIEW VI codes exist to sample data from the sting balance, control the model arm, control the wind tunnel velocity, move the traverse, sample data from the Heise, and post process data.

Flow Characterization Experiment

This section details the experimental setup used to obtain velocity and turbulence profiles for the ELD 407B wind tunnel. This experimental setup was fundamentally the same for the large and small test sections. Each profiling experiment consisted of hot-wire calibration, data sampling, and data analysis. The calibration of the hot-wire was performed every time the hot-wire system was restarted to ensure consistent results. Data sampling and analysis were performed automatically by a series of Matlab codes. The codes output the (X,Y,Z) location of the probe, average velocity, and turbulence calculated via several methods. A diagram of the coordinate system is shown in Figure 3-8.

Hot-wire Calibration

The wind tunnel velocity at an origin point was calibrated versus wind tunnel control voltage using a pitot-static probe. The voltage output from the monitor port of the hot-wire system was then calibrated against wind tunnel control voltage at the same origin point. These calibrations were used to formulate a calibration which related the hot-wire output voltage to a hot-wire velocity.

A Dantec StreamLine constant temperature anemometry (CTA) frame and control computer were used to drive a single axis hot-wire probe in the wind tunnel. The Dantec CTA system was configured to output a voltage corresponding to velocity measured by the hot-wire probe, and none of the internal functions of the CTA frame's internal signal filters or processing units were used. The CTA frame only contained a module for a single axis hot-wire, and it did not contain the Streamline Temperature Module which would allow for measurement of fast temperature changes. The CTA frame was configured to output an analog voltage to an external data acquisition device.

The voltage output from the CTA frame was run to a Hewlett Packard VXI BUS E1421B Mainframe with a HP 1433A DAQ card installed (Figure 3-9). The voltages read by the VXI frame were sampled using a Matlab code which also controlled sampling settings. The code instructed the VXI frame to sample, download, and save the data to the computer. Figure 3-9 shows the VXI frame in the process of automatically sampling data.

The hot-wire probe's output voltage had to be calibrated against velocity. The CTA frame used an automatic precision bridge unit which balanced a Wheatstone bridge each time a hot-wire probe was changed into run mode. The hot-wire probe could not be removed from the probe hanger or disconnected once the Dantec hardware was changed

to run mode because of the risk of breaking the probe. The hot-wire also had to be calibrated each time the system was restarted because the automatic bridge could initialize to a different impedance every time the system was switched on, changing the output voltage of the system.

The CTA system included a calibration venturi type wind tunnel which would ordinarily be used to calibrate the hot-wire probe, however the calibration unit did not have a method to control the temperature of the flow. The calibration unit was stated to have turbulence levels of 2 % and used an internal differential pressure sensor for velocity measurement. Methods exist to correlate a hot-wire calibration to a run condition at a different temperature, but a different way of solving the problem was used which would not involve any error due to a temperature correction.

It was possible to achieve a steady state temperature less than $55^{\circ} \pm 1^{\circ} \text{C}$ if the wind tunnel control velocity were kept beneath 7.0 V, hence it was decided to calibrate the hot-wire based off of a calibrated wind tunnel velocity. The wind tunnel had previously shown a 0.02 m/s standard deviation in velocity calculated using a pitot-static probe, and the constant elevated temperatures did not vary from day to day. As such, it was considered a reasonable choice to calibrate the probe in the tunnel.

The traversing ceiling was installed on top of the test section being examined (Figure 3-10). The ceiling was designed to move a probe holder capable of supporting either a pitot-static probe or a hot-wire probe (Figure 3-11). Experiments were performed with both probes attached simultaneously, but the aerodynamic interference between the probes caused the experiments to be unrepeatable and inaccurate. As such, velocity data had to be gathered from each probe separately.

The traverse was controlled so that the pitot-static probe was centered in the Y and Z directions within the test section. The tip of the probe was traversed so it would lie in a Y-Z plane 0.305 m downstream of the entrance to the test section. This location centered in Y-Z and 0.305 m downstream from the entrance to the test section was referenced as (0,0,0). The X positive direction was chosen to be in the upstream direction. The Z direction was chosen to be positive in the down position, and this caused the Y direction to be positive pointing away from the operator side windows of the tunnel (Figure 3-8).

The wind tunnel control voltage was increased by 0.25 V for a range from 0 V to 10V. One thousand pressure measurements were gathered at each voltage. The temperature of the flow was gathered downstream of the pitot-static probe along the centerline. These measurements were averaged and used to compute the (0,0,0) velocity corresponding to the wind tunnel control voltage. The 0.5 V and lower wind tunnel control voltage settings produced unsteady pressure fluctuations, and hence the velocities corresponding to a wind tunnel control voltage setting of 0.5V or less calculated were inaccurate. Above a voltage setting of 0.5 V, however, velocity was shown to increase linearly with control voltage. The standard deviation of the 1000 velocity measurements was calculated to be less than 0.02 m/s for wind tunnel settings less than 4.0 V. The wind tunnel control voltage vs. origin velocity calibration is shown in Figure 3-12.

Above a 4.0 V wind tunnel control setting, the thermal changes in the tunnel became an issue. A steady state temperature was obtainable up to a wind tunnel setting of 7.0 V, but beyond this control voltage the temperature rose above 55° C, at which point the tunnel's velocity was lowered by the operator and the temperature allowed to decrease. For the cases with steady temperatures the value of temperature was noted and

included in velocity computation. For the cases of rapidly growing temperatures the initial and ending temperatures were noted.

Once a calibration between wind tunnel control voltage and (0,0,0) pressure based velocity was established the hot-wire probe was attached to the probe hanger and traversed to the (0,0,0) location. The wind tunnel control voltage was increased by 0.25 V over a range from 0.0 V to 4.0 V while the tunnel maintained the same temperature. The wind tunnel control voltage was then increased by 0.5 V from 4.0 V to 7.0 V, each time allowing the tunnel to come to a thermal equilibrium. It was discovered that the thermal equilibrium temperatures of the tunnel varied less than 0.2° C from run to run during this experiment; hence the hot-wire calibration in the tunnel appeared to be a reasonable method.

The voltage from the hot-wire system was sampled 512,000 times over 60 seconds and averaged. This voltage measurement was found to be highly repeatable, varying by no more than a corresponding velocity of 0.01 m/s, as long as the tunnel temperature did not vary by more than 0.5° C. Averages of voltages obtained at the same temperature were shown to differ by no more than 0.1 %.

At wind tunnel control voltages above 7.0 V the hot-wire voltage was sampled while the temperature was in a similar range as the temperatures during the pitot-static calibration. In all cases above 7.0 V the temperature increased rapidly toward a maximum cutoff temperature of 55° C. The 4 wire resistance temperature device installed in the tunnel was noted to have a rather slow time constant hence the exact, time dependent variations in flow temperature could not be determined. The thermocouple upstream of the test section was also noted to have a slow time constant, and its

resolution was 1° C. During a high speed run, both temperature sensors would report different temperatures unless steady state had been achieved. This introduced error into the experiment, and velocity data above the speed corresponding to 7.0 V are likely to be erroneous. The data was still gathered for completeness and to possibly highlight trends.

The two calibrations were applied to generate hot-wire voltage vs. wind tunnel origin velocity curves for each test section. Figure 3-13 shows representative calibration data across a wide range of tunnel velocities. It should be noted that calibrations obtained for set-speed tunnel measurements centered around the desired velocity in more detail.

Data Sampling

The requested locations of the hot-wire probe were entered into a code which automatically traversed the probe's location, sampled data at that location, and saved the data in a format which preserved the location data. After the locations were sampled another code was used to automatically convert the hot-wire voltages sampled in the code to equivalent velocities. The code calculated the turbulence of the location using multiple methods and saved the resulting data.

Automatic data sampling

The traversing ceiling was driven by 3 stepper motors. The stepper motors were controlled by a 3 axis Velmex VXM stepper motor control unit. The control unit was connected to the wind tunnel control computer. A separate computer controlled the VXI frame. Both computers were connected to UF's local intranet and were assigned static Internet Protocol (IP) addresses.

A LabVIEW code was written which automatically traversed the probe through a prescribed set of points within the tunnel. This code was executed on the wind tunnel control computer. After the traverse had moved to a data sampling point, the code used

IP to contact the computer attached to the VXI frame and send the computer the (X,Y,Z) location of the probe. The recipient code then executed the Matlab code which sampled the hot-wire voltage data. The data from the sample was automatically saved with the (X,Y,Z) probe location data to aid in post processing.

Data sampling hardware and settings

An eight-channel breakout box was connected to the 16 bit HP 1433A card in the VXI frame. Channels 1 and 2 were connected to each other using a cable tee. Both channels were connected to the monitor line of the Dantec hot-wire system. Channel 3 was connected with a 50 Ω terminator to monitor signal noise. All cables were high quality shielded coaxial cables using Bayonet Neill Concelman (BNC) 50 Ω shielded radio frequency connectors. The Matlab code passed settings information to the VXI frame which instructed it to sample both time and power spectra data from the three channels.

Channels 1 and 3 were ac coupled at 1 Hz using the HP 1433A built in high pass filter. The direct current (dc) value of hot-wire voltage was sampled on channel 2 with a range of ± 5.0 V, leading to a voltage resolution of $1.5 \text{ E-}4$ V. The sampling range of channels 1 and 3 was ± 0.05 V, leading to a voltage resolution of $1.5 \text{ E-}6$ V, for all measurements except those near the walls of the wind tunnel in the boundary layers. Boundary layer voltages were sampled at ± 0.1 V, leading to a voltage resolution of $3.0 \text{ E-}6$ V. The voltages were sampled at a frequency of 16,000 Hz in blocks of 2048 samples. The data were sampled at this rate to ensure that a frequency span of 7.8 Hz to 6250 Hz was represented. Below 7.8 Hz the variation in velocity was most likely due to unsteadiness which was not related to turbulence [27]. 250 blocks of data were sampled to yield 512,000 samples at each (X,Y,Z) location. These settings produced a spectral

frequency span of 6250 Hz with 6.1 Hz/bin in 1024 bins. These settings were chosen because they adequately represented most of the power spectral density (PSD) of the voltage data. Figure 3-14 is a PSD plot of a 10 m/s measurement at the (0,0,0) point and a PSD plot of the channel 3 50 Ω terminator which showed noise internal to the VXI. A signal spike at 1 and 1100 Hz was common to both signals, but its overall intensity was so small that it did not significantly contribute to the PSD turbulence values.

Post Processing

A set of Matlab codes were written to post process the hot-wire voltage data. Each Matlab data file corresponding to a (X,Y,Z) location was loaded into memory. The hot-wire voltage to velocity calibration was directly applied to each data point in the time series data. The PSD distribution was derived from the autospectra which was output from the VXI frame. The data was calculated using a Hamming window with a 50 % overlap. The calibration was then used to determine the magnitude of velocity variation represented in the PSD data. The code effectively converted voltage data at each sampling (X,Y,Z) location into velocity data.

Parseval's theorem applied to an infinite length signal, as shown in equation 3.1, may be used to relate PSD and root mean square (RMS) data [18]. The integral of the magnitude of the square of the time data should equal to the integral of the PSD calculated from the time data. Equation 3.2 is the definition of the RMS. One definition of turbulence is that the root mean square (RMS) value of the variation component of the velocity signal be divided by a reference velocity [19]. According to this information the square root of the summed PSD data should yield the same value as the RMS for an ac coupled signal such as that produced by channel 1 (Equation 3.3). Indeed, PSD and RMS

calculations applied against the voltage information matched to numerical precision limits.

$$\int_{-\infty}^{\infty} |f(t)|^2 dt = \int_{-\infty}^{\infty} \Phi(\omega) d\omega \quad (3.1)$$

$$f_{RMS} = \sqrt{\frac{1}{T_2 - T_1} \int_{T_1}^{T_2} f(t)^2 dt} \quad (3.2)$$

$$f_{RMS} = \sqrt{\frac{1}{(T_2 - T_1)} \int_{\omega_1}^{\omega_2} \Phi(\omega) d\omega} \quad (3.3)$$

The method by which the voltage information was converted into velocity information was therefore capable of highlighting possible errors in the hot-wire calibration. The series of dc voltages from channel 2 was converted to velocity using a Matlab script which used the function spline to convert hot-wire voltage to velocity based off of the hot-wire voltage vs. tunnel control voltage and (0,0,0) velocity vs. control voltage. The mean of this velocity series was calculated, indicating the steady velocity at that (X,Y,Z) point. The small variations in ac fluctuations of channel 1 could not be directly applied using the dc method. Instead, the slope of the hot-wire voltage vs. (0,0,0) velocity curve was found at the mean velocity calculated from the channel 2 data. This slope was squared and multiplied against the voltage PSD data to yield velocity PSD data. Any difference in the PSD calculated turbulence vs. the RMS calculated turbulence would show both numerical precision and calibration errors.

Local and global turbulence values were then calculated defined as follows. Local turbulence was defined as the turbulent variation divided by the local velocity, while global turbulence was defined as turbulent variation divided by some reference velocity. These two methods were used to highlight turbulence levels in the boundary layer. The variational component, remaining constant for a measurement, divided by the lower mean

velocity in the boundary layer will yield a larger value for turbulence than the global method. For the global turbulence calculations the reference velocity was chosen to be the velocity at the (0,0,0) point in the wind tunnel, and the local velocity was obtained from channel 2.

The turbulence and velocity data were sorted and saved referenced to (X,Y,Z) locations. The data was then plotted in TecPlot and Excel to yield plots representing variations in turbulence and velocity over distance in the tunnel.

Results

Velocity and turbulence profiles were gathered from each test section at two (0,0,0) set velocities. The velocities of interest were 10 m/s, and the velocity corresponding to a wind tunnel control voltage of 5.0 V. A speed of 10 m/s was chosen because that was anticipated as the most useful velocity for the analysis of MAVs. The (0,0,0) velocity corresponding to a wind tunnel control voltage of 5.0 V, 50.0 m/s for the small test section and 27.0 m/s for the large test section, was chosen because it represented a reasonable upper limit on the long term wind tunnel run speed. This setting allowed the tunnel to maintain thermal equilibrium and stay below 45° C.

Small test section results

Velocity and turbulence distributions across the small test section will be presented for an origin velocity of 10 m/s. The distributions for an origin velocity of 51 m/s followed the same trends as those for 10 m/s. The plots for the 51 m/s are presented in Appendix A. Profile information was sampled at $X = 0.0$ m and $X = -1.22$ m because any MAV model tested would lie between those two X values in the test section.

A global RMS and PSD turbulence vs. velocity plot was prepared along the $Y = Z = 0.0$ m centerline of the tunnel at $X = -1.22$ m (Figure 3-15). The data was originally

sampled at two X locations, but the data for the $X = 0$ m location was determined to be inaccurate due to a mistake in the experimental procedure. The mistake was not discovered until after the ceiling was removed from the test section, and hence was not able to be corrected. Figure 3-15 highlights the difference between PSD and RMS turbulence values. At low speeds there is a substantial difference in PSD and RMS turbulence while at higher speeds there is good agreement. At 85 m/s there is again discrepancy due to changes in thermal equilibrium. The RMS and PSD turbulence values followed the same trends with a small offset, hence further results will be presented showing the RMS turbulence only.

The data sampling for the small test section was fully automated, and a large number of data points could be obtained with no user intervention. This ease of data sampling allowed for a full grid of samples to be taken across the test section, and contour plots were prepared in TecPlot representing the velocity and turbulence variation across the test section.

Figure 3-16 shows the velocity variation across the test section at the $X = 0$ m location. It was noticed that the profile was roughly symmetric about the Y-axis, but the very center had a velocity deficit on the order of 2 %. This flow pattern is characteristic of entrance regions and must be considered when performing tests in this test section [20]. It appeared that the operator side of the test section was flowing faster than the inward facing side, but the variation was on the order of 1 %. The velocity along the top of the test section appeared to be much lower, especially in the corners, than a fully symmetrical profile. The probe was traversed to within 0.635 cm of the wall, and barely any effects of the boundary layer were seen.

The RMS turbulence profile at $X = 0$ m is shown in Figure 3-17. This data also shows a profile that is roughly symmetric around Y , however the turbulence profile across the top of the test section clearly showed that something was awry with the measurements. The lower corners showed an expected increase in turbulence, but a reason for the high turbulence across the top of the test section had to be determined.

A likely culprit to the unexpected velocity and turbulence variations is highlighted in Figure 3-18. The probe holder which attached the traverse to the hot-wire probe extended through the ceiling of the traverse through a brush seal. The seal consisted of two rows of very dense brush material which allowed solid objects to pass through but resisted airflow. The ceiling actually moved across the whole test section in the Y direction, hence all measurements taken toward the top of the test section were affected by the surface being brush and not smooth plastic.

In order to prevent airflow from crossing the brush seal, duct tape was applied to cover the entire top and bottom side of the seal for the tests on the large test section. This error was not caught in time to retake the small test section data, and hence the data for the $X = -1.22$ m reflects the same behavior. Very little airflow crossed the seal under run conditions, however it was believed that the texture of the brush was responsible for creating turbulence that altered the local nature of the boundary layer and velocity profile. Figures 3-19 and 3-20 show the velocity and turbulence contours at the $X = -1.22$ m location. The growth of the boundary layer was evident in the turbulence plot, and the asymmetry in velocity across Y was also evident. The boundary layer effect in the lower corners extended as far as 40 cm into the flow, and the turbulence and velocity asymmetries at the top of the test section were still present. The intensity of the velocity asymmetry, however, was calculated to be on the order of a 4 % difference, indicating a

potential problem for MAV measurements. The centerline velocity deficit was still present but was less severe than at the $X = 0$ m case.

Large test section results

Velocity and turbulence distributions across the large test section will be presented for an origin velocity of 10 m/s. The distributions for an origin velocity of 27 m/s followed the same trends as those for 10 m/s. The plots for the 27 m/s are presented in Appendix A. Profile information was sampled at $X = 0.0$ m and $X = 1.22$ m because any MAV model tested would lie between those two X values in the test section.

A global RMS turbulence vs. velocity plot was prepared along the $Y = Z = 0.0$ m/s centerline of the tunnel (Figure 3-21). The data was sampled at two X locations, and it was noted that the downstream X location had an increased level of turbulence over the upstream location. The turbulence distributions followed the same basic trends with respect to velocity.

The traversing ceiling when installed on the large test section would often malfunction when traversing across the Y direction. The stepper motor did not have any feedback mechanism, and while moving the motor would often be overloaded. The motor would receive the commands to complete its motion, but no motion would occur. This behavior did not occur on the small test section at all, and a different data sampling method was devised to gather points of interest. Instead of a fully automated data sampling interface, the probe had to be moved to the desired location in the tunnel. When the motor locked up, measurements were taken of the probe's (X, Y, Z) location, and the probe was commanded to move until it reached a desired location. The Y axis motor would lock up even when the tunnel was not running, and was considered an

inherent design flaw in the traversing table. This problem severely limited the number of data points that could be gathered.

The velocity and turbulence variations were sampled across X at the centerline for a (0,0,0) velocity of 10 m/s. The centerline velocity decreased rapidly from its initial value at the beginning of the test section (Figure 3-22). 30 cm after the origin the velocity was at a minimum, but the velocity grew as the probe progressed downstream. This downstream increase in velocity is a natural consequence of continuity as the boundary layers grow toward a fully developed Poiseuille flow solution. The test section, however, has insufficient length for the flow to become fully developed. The turbulence levels are also shown to increase as the probe was traversed downstream (Figure 3-23). The turbulence is shown to almost double in intensity from the inlet to exit of the test section, hence test apparatus would be best placed upstream in the test section.

The velocity and turbulence variations across the Y axis were prepared for $Z = 0$ m and $X = 0.0, -1.22$ m, and at an origin velocity of 10 m/s. The velocity variation across Y was approximately symmetric, and a large boundary layer was present (Figure 3-24). The apparent thickness of the boundary layer was on the order of 9 cm at $X = 0.0$ m, and 11.5 cm at $X = -1.22$ m. This large boundary layer meant that the core flow of the large test section was only 2.0 to 6.0 cm larger than that in the small test section. It was noted that the velocity profile had a decreased velocity on the center compared with the outer limbs similar to the small test section. This is a sign of an inappropriately designed system, and is likely due to the straight walled diffuser's location downstream of the plenum and upstream of the test section. The large boundary layer had a significant effect on the turbulence levels near the walls (Figure 3-25). The inner region of the flow

had very low turbulence levels, but the effects of the boundary layer turbulence were present further in than the apparent boundary layers.

The velocity (Figure 3-26) and turbulence (Figure 3-27) variations across the Z-axis were then prepared for $Y = 0$ m and $X = 0.0, -1.22$ m at an origin velocity of 10 m/s. The velocity variation across Z was also approximately symmetric, and a large boundary layer was present. The variations across the Z-axis essentially mimicked those for the Y axis, indicating a symmetric profile.

The flow variation in the direction of one corner was then studied. The probe was traversed along a line on which $Y = Z$, and $X = 0.0$ m and $X = -1.22$ m. The data showed a slightly thicker boundary layer (Figure 3-28) and more widespread effects of turbulence toward the corner (Figure 3-29), but this was an expected corner effect.

Discussion of Error

The turbulent variation was calculated using the RMS and PSD methods. The difference in value between the two methods proved to be small but not negligible. The values differed by 6 % to 8 % at 10 m/s and 3 % to 5 % at a 5.0 V control setting. It was difficult to determine the effects of numerical precision, but it was noted that the hot-wire vs. velocity curve had a larger slope at the low speed than at the high speed. Inaccuracy in the calibrations would have more of an effect on a smaller slope than a larger slope because of the difference in divisor. As such errors were more likely to affect the high speed calculations of PSD turbulence, the RMS values were presented. Errors due to rapid temperature variation were likely at very high speeds.

The error between PSD and RMS methods was also noted to increase within the boundary layer. This effect is most likely due to the application of the slope calibration at a mean velocity to the PSD data. The mean velocity in the boundary layer was likely

fluctuating on a time scale which could not be gathered using the sampling settings. It was possible that the high pass filter may not have had adequate response which would tend to invalidate the RMS calculations. However, a separate RMS calculation was performed on the channel 2 data in boundary layer cases with different settings which validated the channel 1 RMS data.

Although the values served to reinforce the validity of each other by their near agreement, it was evident that RMS turbulence information obtained from channel 1 was less erroneous than PSD calculated data.

The brush seal at the top of the traversing table increased the turbulence in the area surrounding it and influenced the local velocity. Taping over the seal proved an effective method to decrease the affects on turbulence and velocity.

Conclusions and Recommendations

Based on the data several conclusions were drawn about the test sections. The large test section had a very thick boundary layer, on the order of 45 % of the tunnel's cross sectional area, at its entrance which increased in thickness substantially by the time it reached the exit. The size of the boundary layer served to reduce the core flow of the large test section to nearly the size of the small test section. This large boundary layer is certainly due to the straight walled diffuser preceding the test section. It is recommended that methods of decreasing boundary layer thickness be tested on the large test section to render more of its area to be usable as uniform velocity flow. Turbulators or vortilators could be installed in the straight walled diffuser to reduce the boundary layer thickness my maintaining flow attachment. The diffuser could also be modified to have suction along the wall to reduce boundary layer thickness. A better modification would be the construction of a plenum designed to mate directly with the large test section, and this

would also require the construction of a duct to fill the length previously occupied by the straight walled diffuser.

The turbulence levels in the core of the large test section were slightly higher than those in the small test section, but the large boundary layer and high turbulence at the walls of the large test section make the small test section a better choice for small wing span models. As such, the small test section will be used for most of the tests discussed in this thesis.

The data sampled above a wind tunnel control voltage of 7.0 V clearly contain error due to the rapidly changing temperature. The amount of error is difficult to quantify, and the trends are not necessarily to be trusted. After an adequate wind tunnel cooling system is installed the hot-wire tests should be repeated to yield valid results for the high speed range.

Sting Balance Vibrational Analysis

It was of interest to determine the vibrational characteristics of the sting balance and mounting arm. The mounting jaw of the balance was compliant in all its degrees of freedom, and it was suspected that this compliance could influence the flow characteristics of a model by allowing movement. The arm which the balance was attached to was also very compliant in rotation because it was attached to the servo unit through an axial spring (Figure 3-30).

The balance was necessarily compliant as the loads on the mount are sensed through strain gauges which measure the elastic strain of the balance. The axial spring was a necessary attachment between the arm and servo because the servo would often jump on startup. If the axial spring were not in place it is likely that the servo would damage itself performing such harsh maneuvers.

In order to determine the vibrational characteristics of the balance and arm, a NCDT Opto laser displacement sensor was connected to channel 1 of the VXI frame. The focus point of the sensor was directed at the upstream tip of the jaw used to hold models. The laser displacement sensor output ± 5.0 V depending on the distance from equilibrium, and its calibration was 1.0 V/mm. A time series was used to compute the natural frequency of the angle arm, while a PSD plot was prepared to determine the vibrational frequencies of the balance with and without a MAV wing model mounted.

The arm installed in the test section was first manually deflected, and the VXI frame was ordered to start gathering data. The arm was released and was allowed to oscillate until its motion had been damped out. The data from the experiment was trimmed to only include the oscillating period, and a code was used to calculate the difference between the peaks of the time history plot and determine a mean damped natural frequency with the wind tunnel turned off. The period of oscillation for the arm mounted in the small test section was 0.2101 s. The experiment was not tested with the tunnel turned on, but it was expected that aerodynamic flow would serve to damp the oscillation and decrease the damped frequency.

The vibrational characteristics of the balance were tested while mounted on the arm in the small test section. The vibration in the pitching direction was deemed the most important because pitching vibration would affect AOA. The laser displacement sensor was aligned under the jaw with and without a 15.2 cm wing model mounted. A shaker device was positioned beneath the downstream portion of the arm and controlled by a function generator. The function generator was ordered to perform a frequency sweep ranging from 10 Hz up to 10,000 Hz, and the VXI frame was configured to sample across multiple frequency spans. It was determined that most oscillation occurred at less than

300 Hz, so the function generator was reconfigured to sweep from 10 Hz to 300 Hz.

Figure 3-31 shows the experimental setup with the model mounted.

The VXI gathered 8192 samples with a voltage range of ± 5.0 V and a sampling frequency of 750 Hz, leading to a frequency span of 292.9 Hz. The resulting PSD plots for a plain balance and a model mounted is shown in Figure 3-32. It was noted that the balance alone had strong resonant frequencies at 51 Hz and 100 Hz while the case with the model had shifted natural frequencies of the balance and added a resonance at 36 Hz, presumably due to the model. The magnitude of the oscillation was dependent on the input from the shaker device, and it was noted that most of the 60 Hz line noise was obscured by the signal.

The vibrational frequencies of the balance and arm must be taken into consideration when performing experiments, as must the frequency associated with the model. Naturally, every model will be different and will have different vibrational characteristics, but this experiment served to highlight the predominant modes of the balance and show the general effects of the addition of a model.



Figure 3-1. ELD Model 407B wind tunnel with small test section installed, photo reprinted with permission of ELD, Inc.



Figure 3-2. Large test section installed in wind tunnel loop, downstream of both plenum and straight walled diffuser.



Figure 3-3. Wind tunnel control interface.



Figure 3-4. Aerolab balance connected to angle arm in large test section with MAV wing model mounted.



Figure 3-5. Model arm for small test section constructed from 2.5 cm outer diameter steel tube.

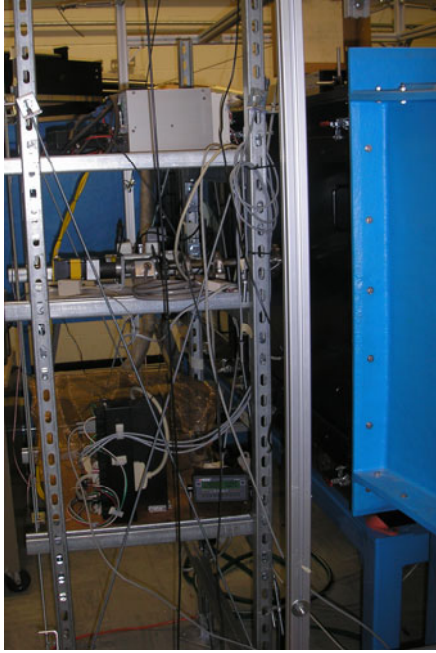


Figure 3-6. Equipment structure, SCXI frame (top), servo motor and encoder (middle), servo control hardware and Heise (bottom), large test section (right).



Figure 3-7. Low profile jaw attached to model (left) and Aerolab balance (right).

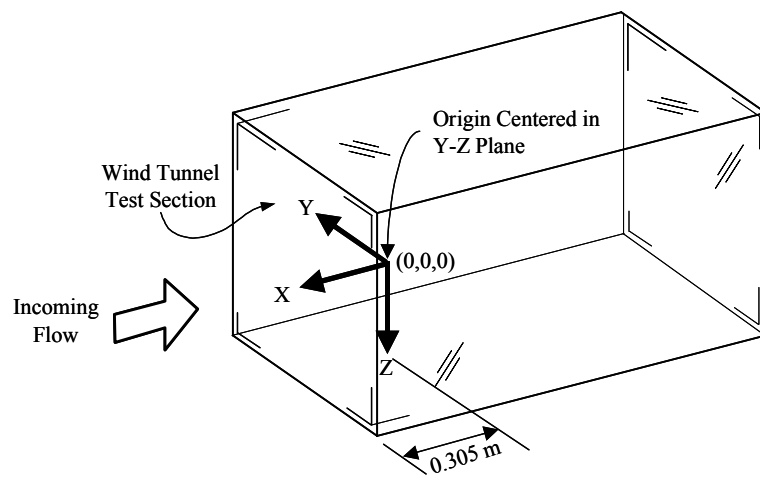


Figure 3-8. Coordinate system used for turbulence and velocity profile determination.



Figure 3-9. VXI frame and computer showing data as it was being gathered automatically.



Figure 3-10. Wind tunnel traversing ceiling installed on top of small test section.

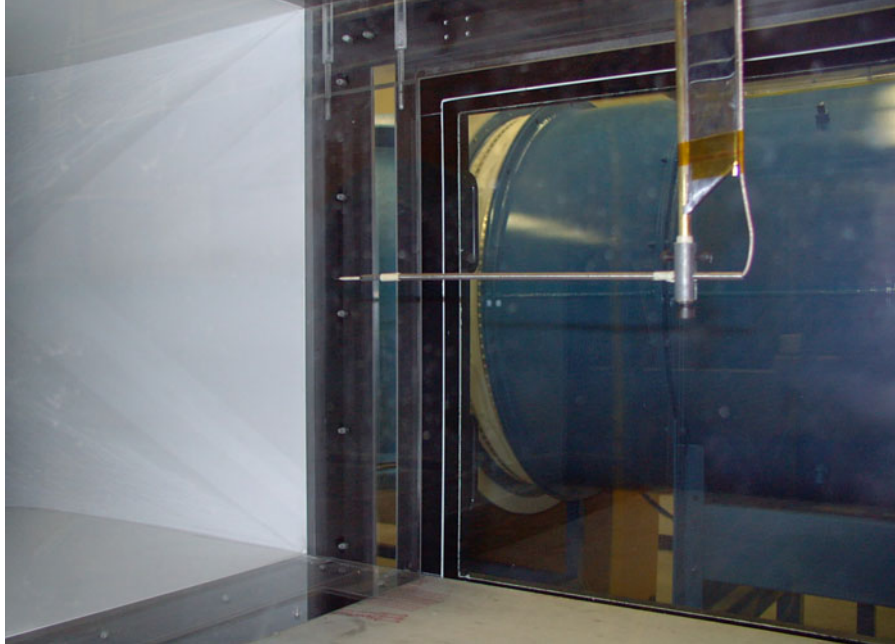


Figure 3-11. Hot-wire probe mounted to probe holder inside small test section. Axial fan housing is visible through the window.

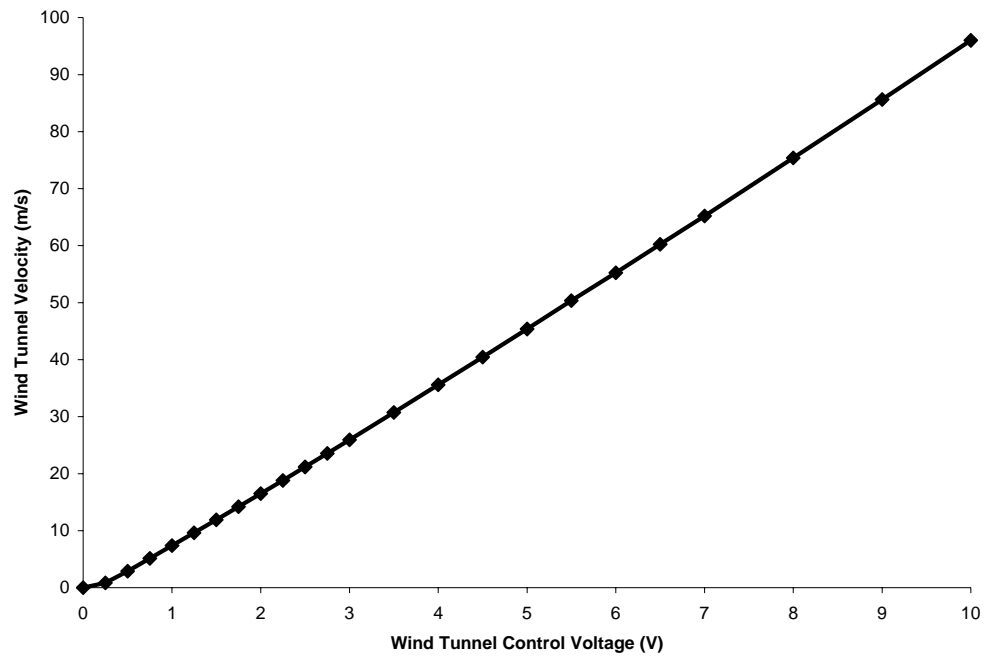
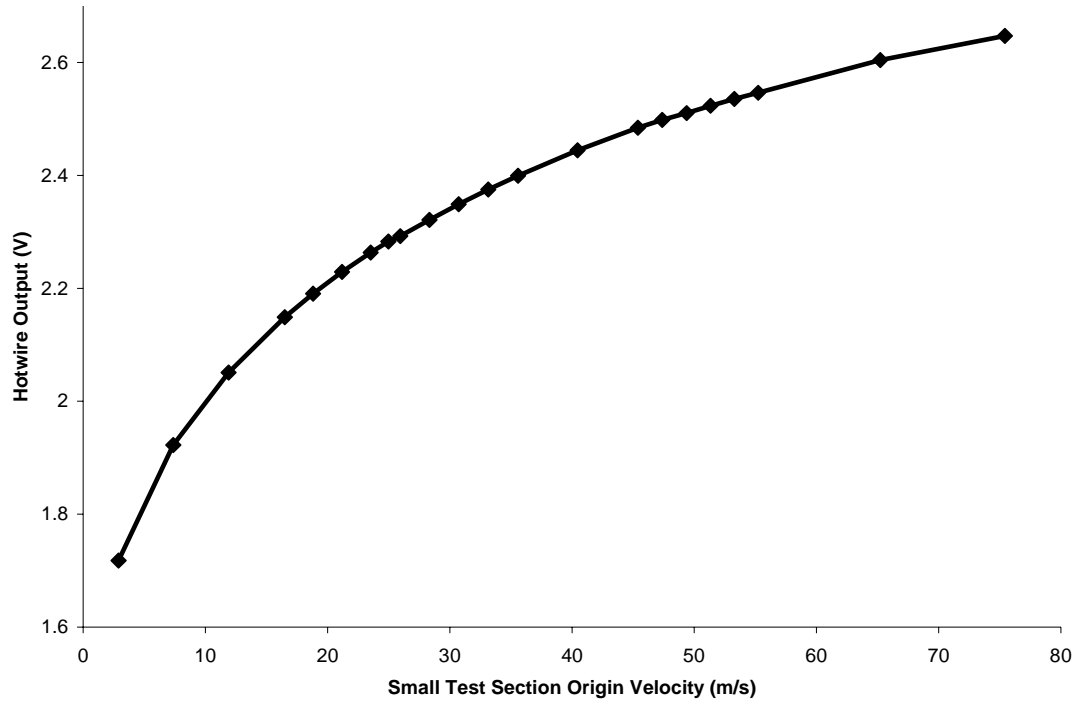
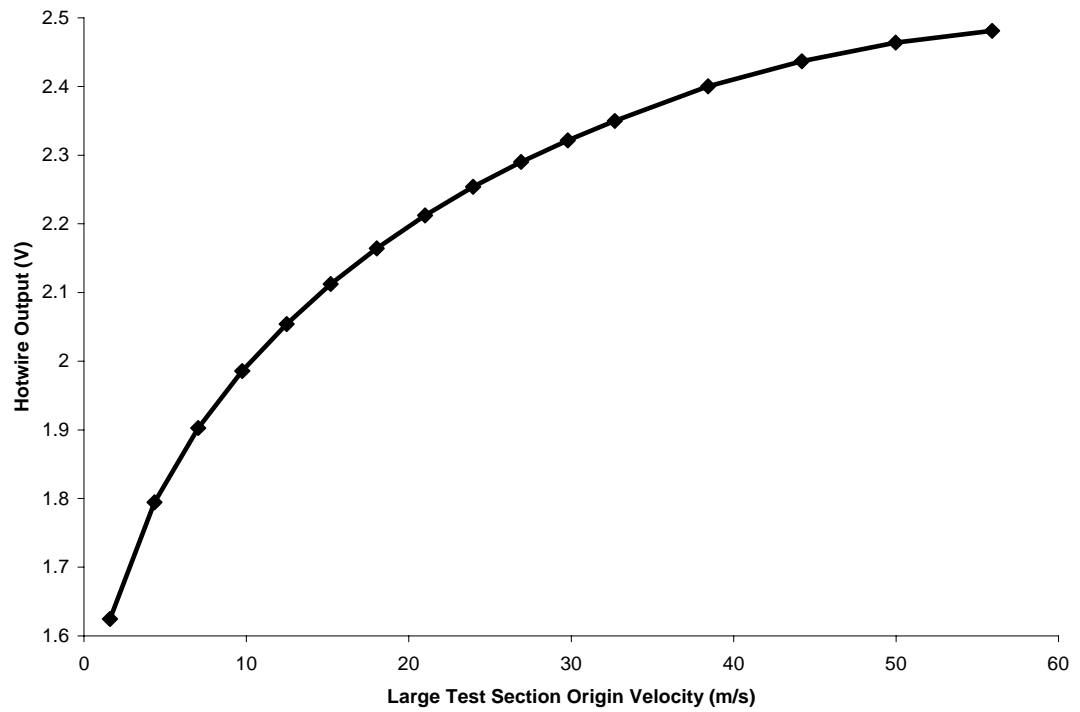


Figure 3-12. Wind tunnel control voltage vs. wind tunnel origin velocity for small test section.



A)



B)

Figure 3-13. Small (A) and large (B) test section hot-wire calibrations.

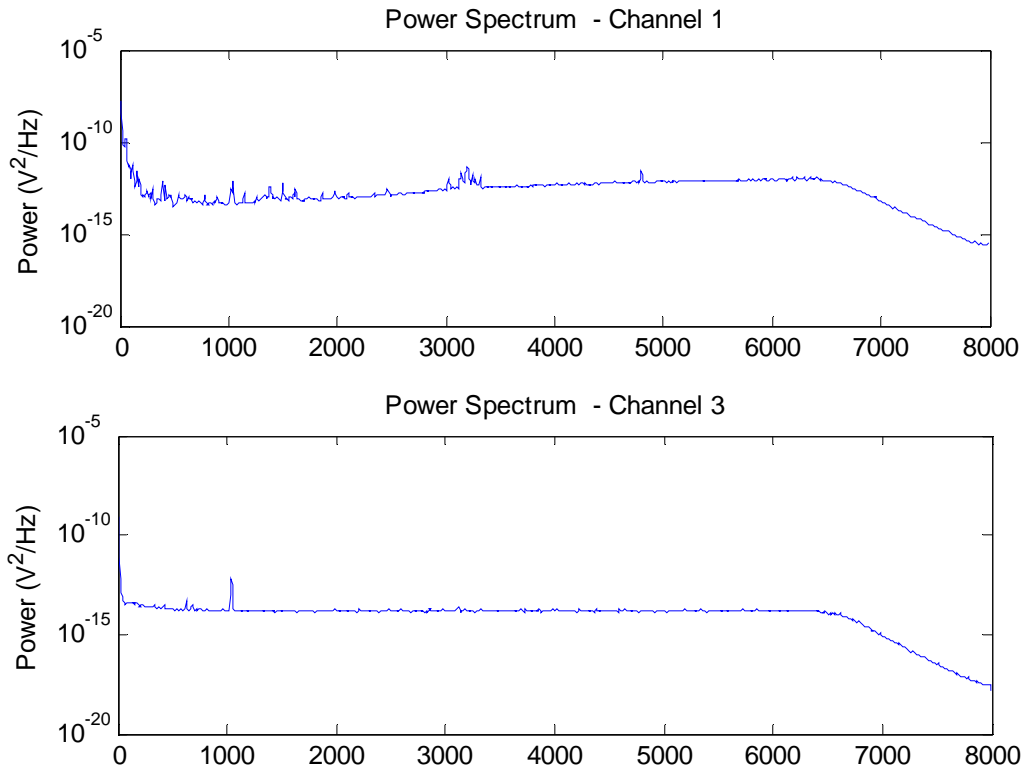


Figure 3-14. PSD plots for 10 m/s (Channel 1) and 50 Ω terminator (Channel 3) data taken at the (0,0,0) point.

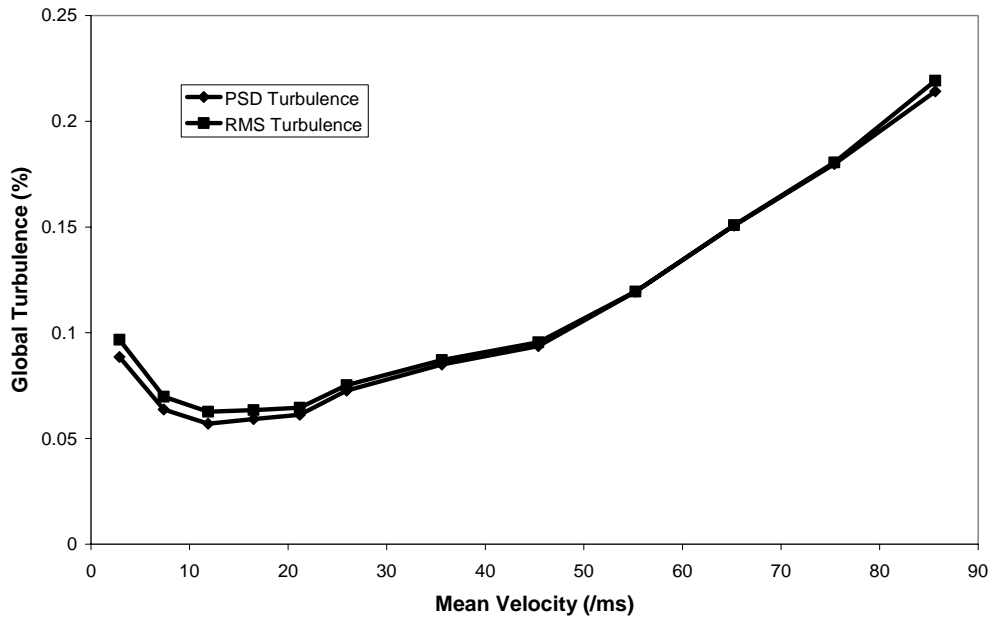


Figure 3-15. Centerline Global RMS and PSD Turbulence variation over different velocities for X = -1.22 m.

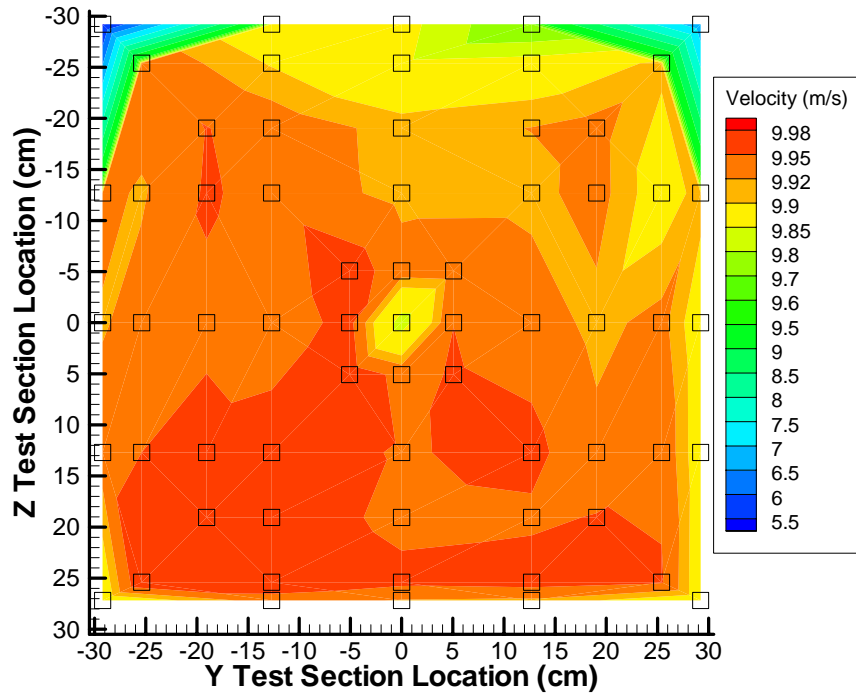


Figure 3-16. Velocity contour across test section at $X = 0$ m. Black squares are data sampling locations.

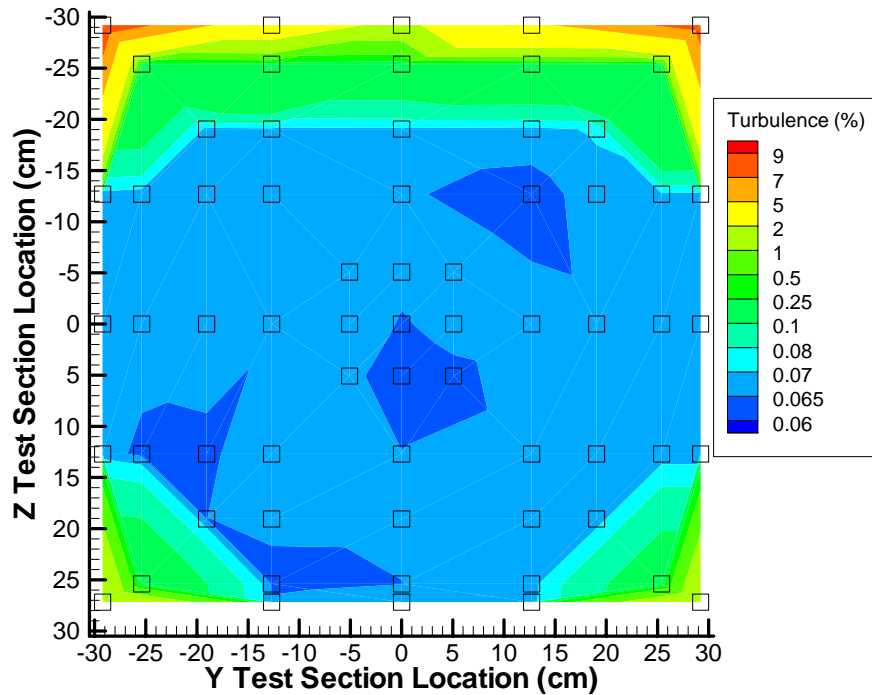


Figure 3-17. RMS turbulence contour across small test section at $X = 0$ m. Black squares are data sampling locations.

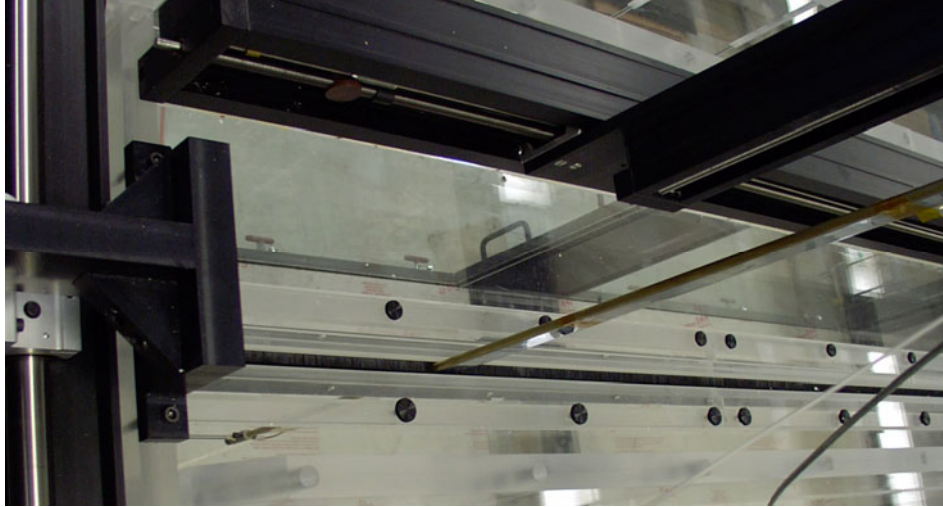


Figure 3-18. Picture of probe holder extending through traverse ceiling brush seal.

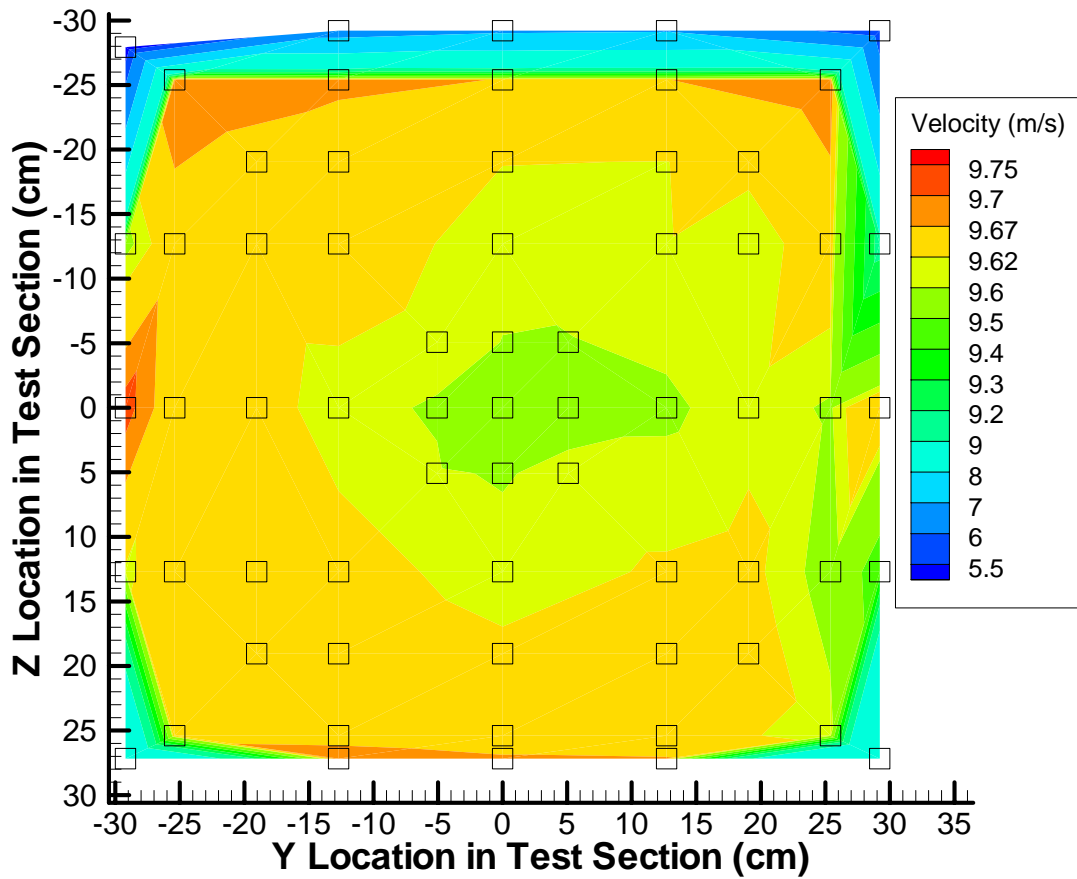


Figure 3-19. Velocity contours across test section at $X = -1.22$ m location. Black squares are data sampling locations.

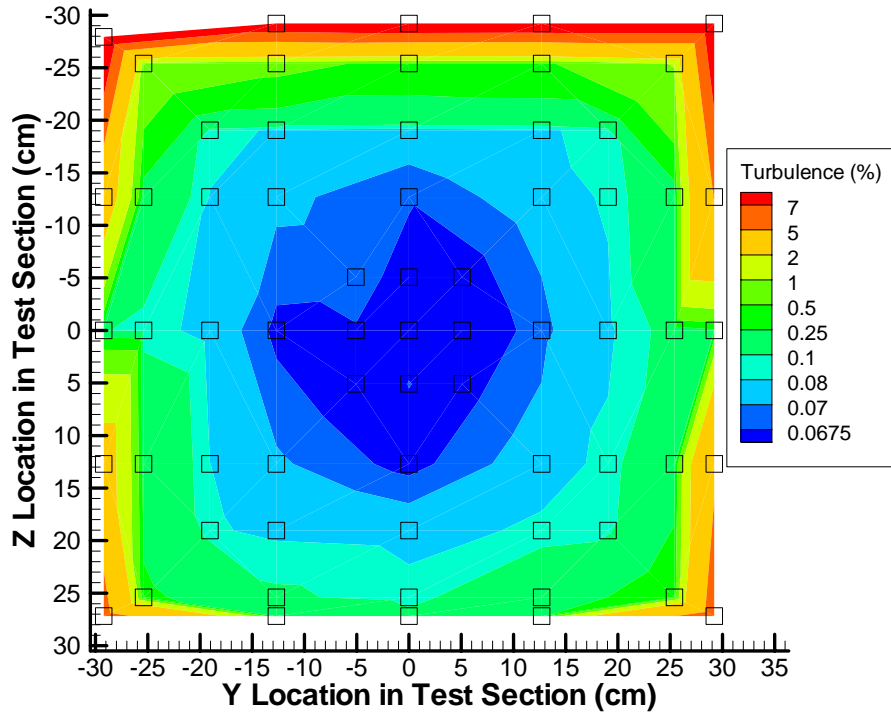


Figure 3-20. RMS turbulence contours across test section at X = -1.22 m location. Black squares are data sampling locations.

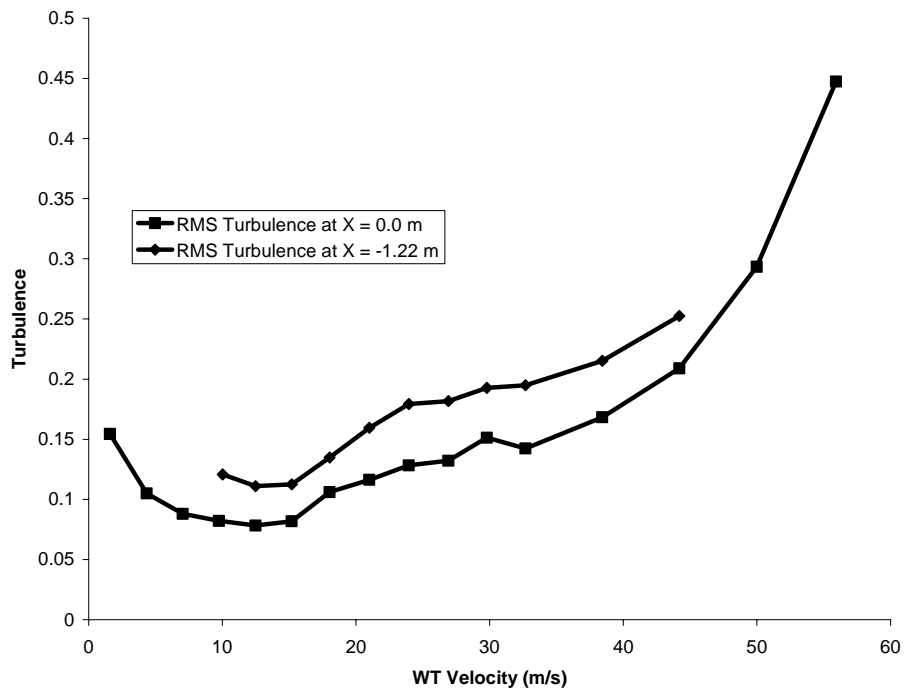


Figure 3-21. Centerline Global RMS and PSD Turbulence variation over different velocities at X locations.

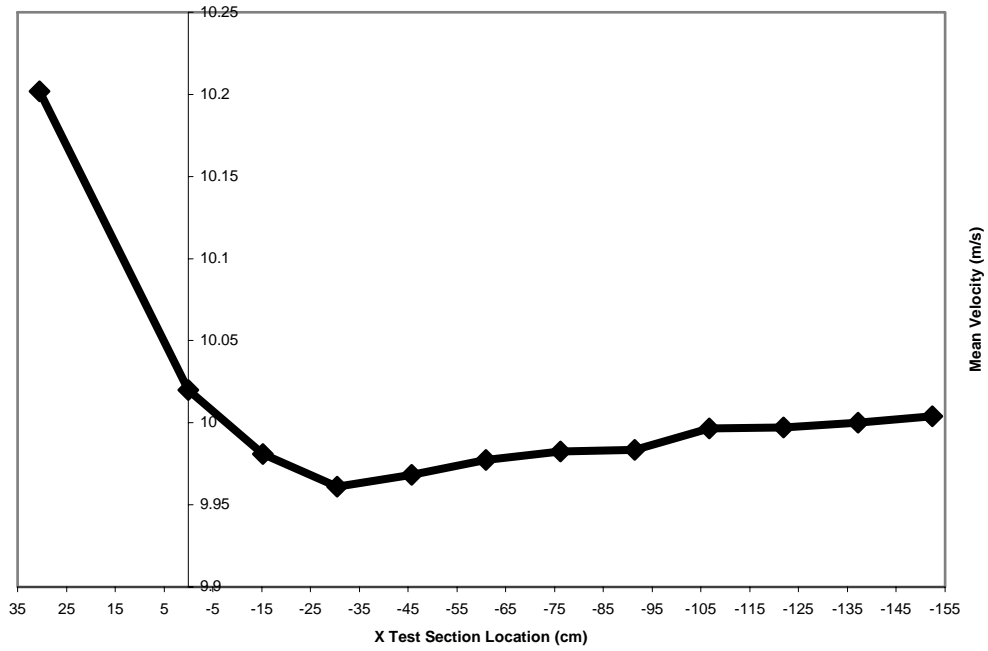


Figure 3-22. Mean velocity variation over X along centerline of large test section at a (0,0,0) velocity of 10 m/s.

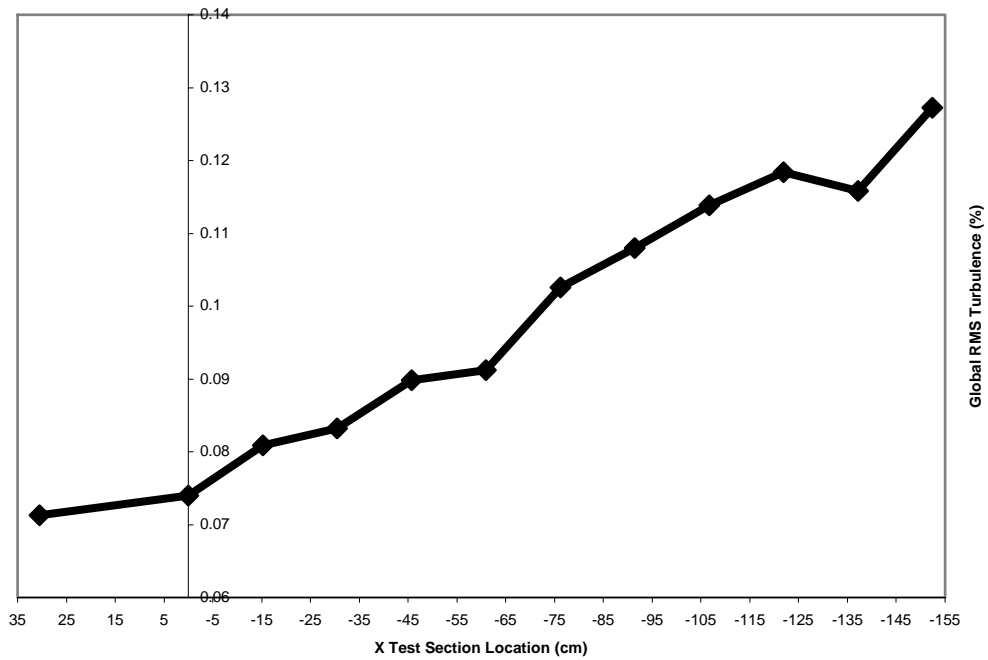


Figure 3-23. Turbulence variation over X along centerline of large test section at a (0,0,0) velocity of 10 m/s.

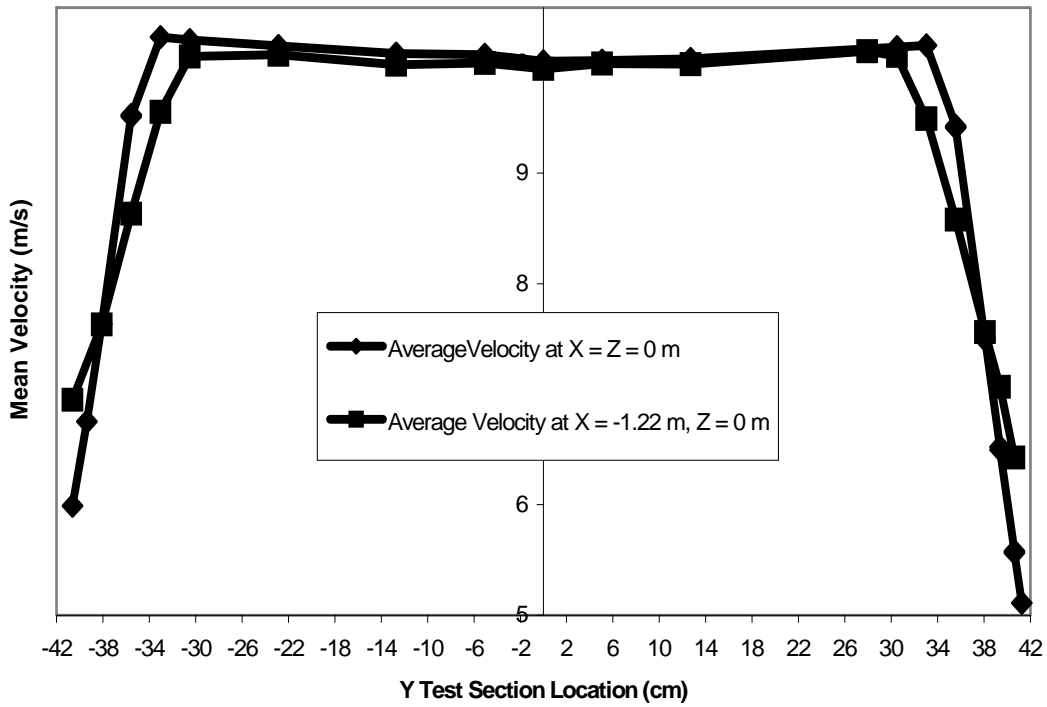


Figure 3-24. Variation of velocity across Y direction for (0,0,0) velocity of 10 m/s, Z = 0.0 m, X = 0.0, -1.22 m.

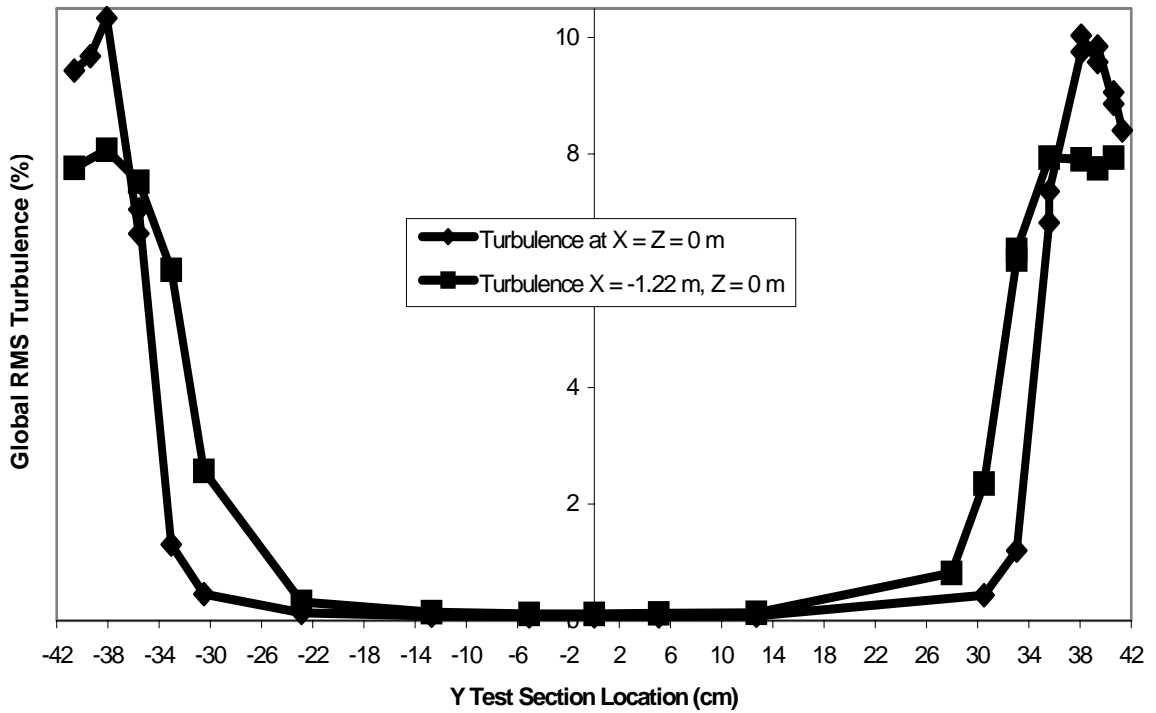


Figure 3-25. Variation of global RMS turbulence across Y direction for (0,0,0) velocity of 10 m/s, Z = 0.0 m, X = 0.0, -1.22 m.

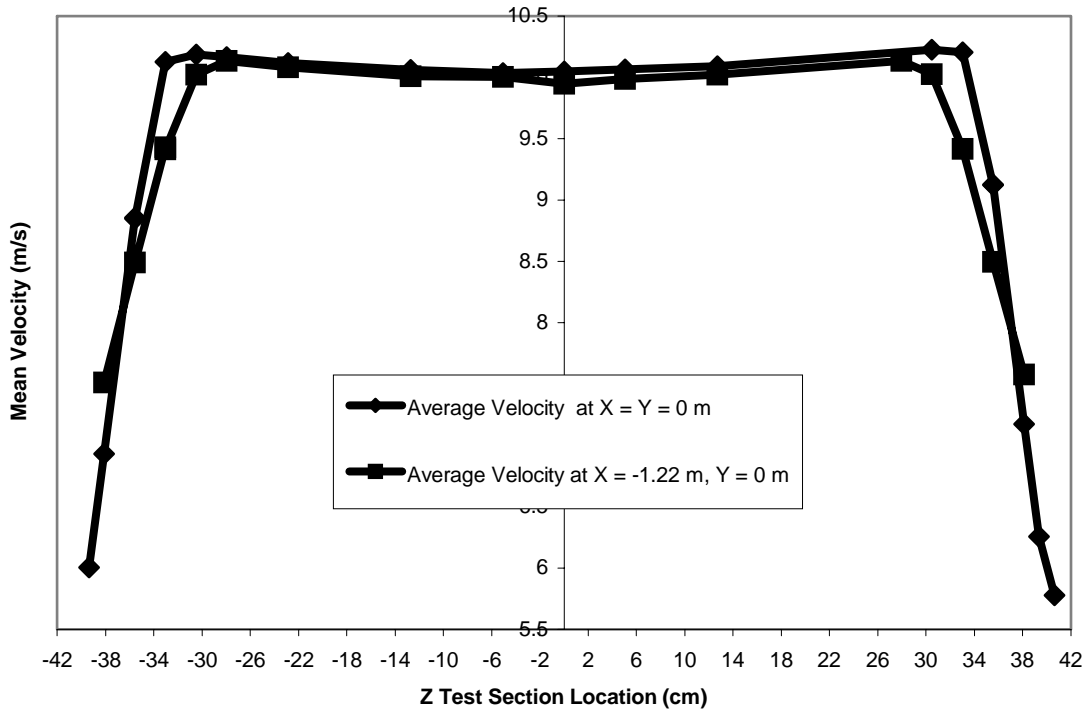


Figure 3-26. Variation of velocity across Z direction for (0,0,0) velocity of 10 m/s, Y = 0.0 m, X = 0.0, -1.22 m.

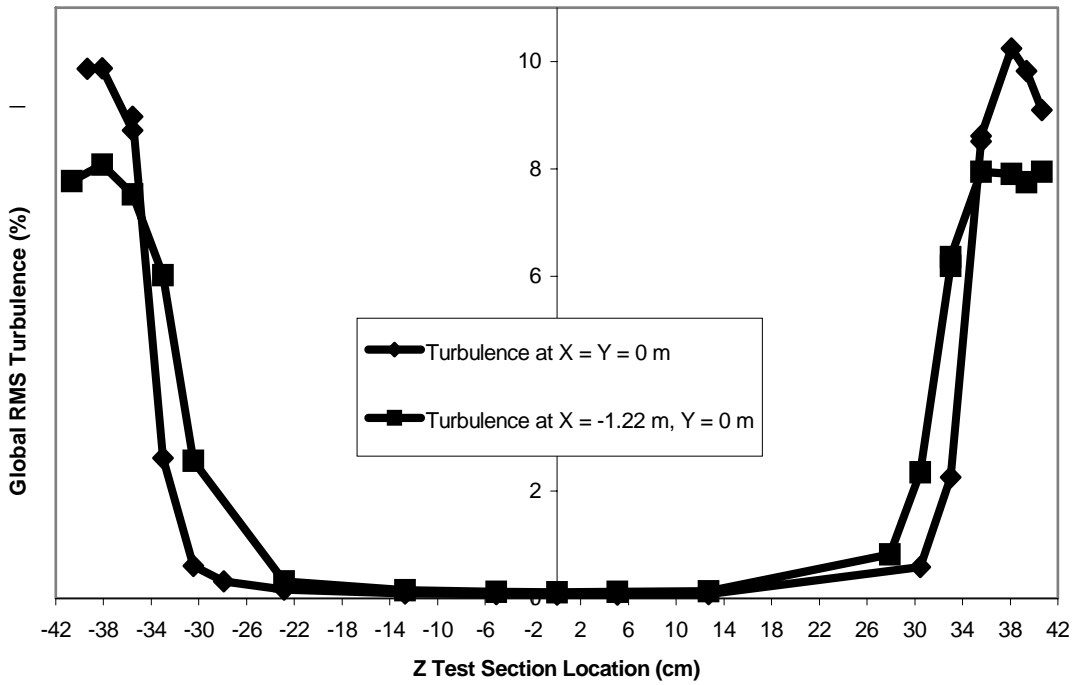


Figure 3-27. Variation of global RMS turbulence across Z direction for (0,0,0) velocity of 10 m/s, Y = 0.0 m, X = 0.0, -1.22 m.

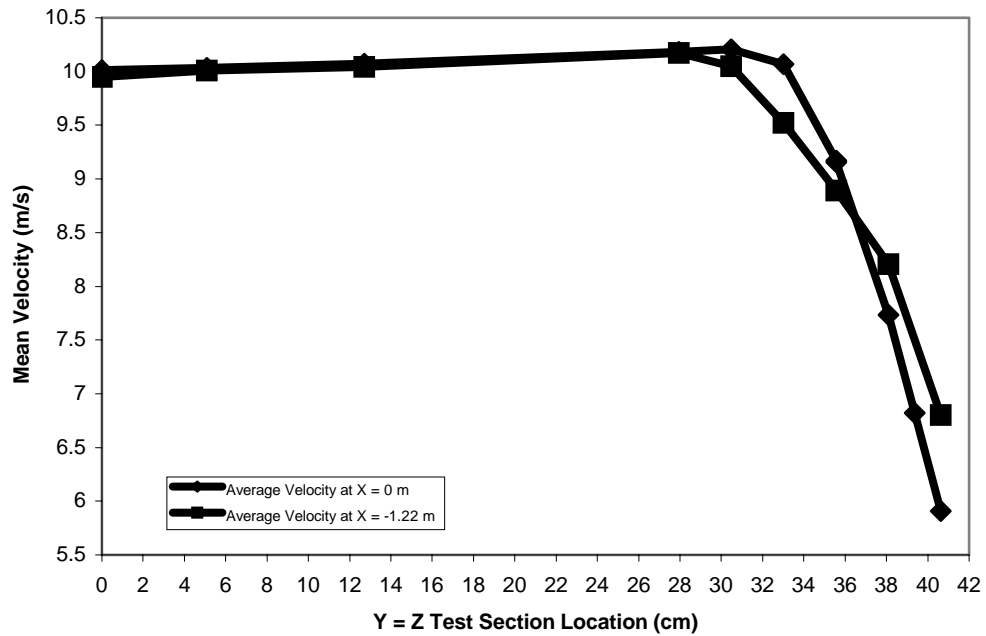


Figure 3-28. Variation of velocity across Y = Z direction for (0,0,0) velocity of 10 m/s, X = 0.0, -1.22 m.

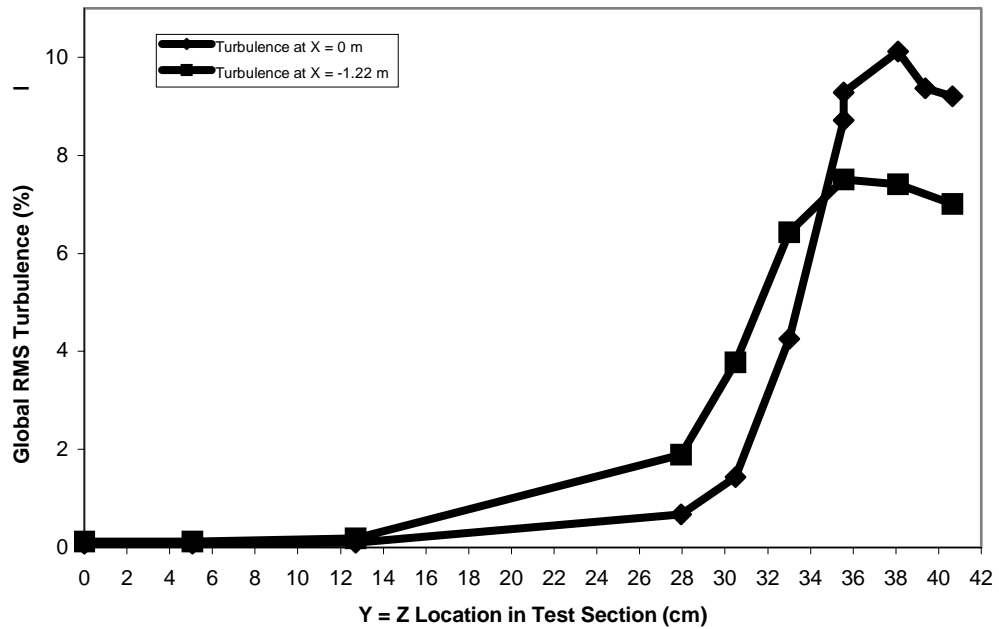


Figure 3-29. Variation of global RMS turbulence across Y = Z direction for (0,0,0) velocity of 10 m/s, X = 0.0, -1.22 m.

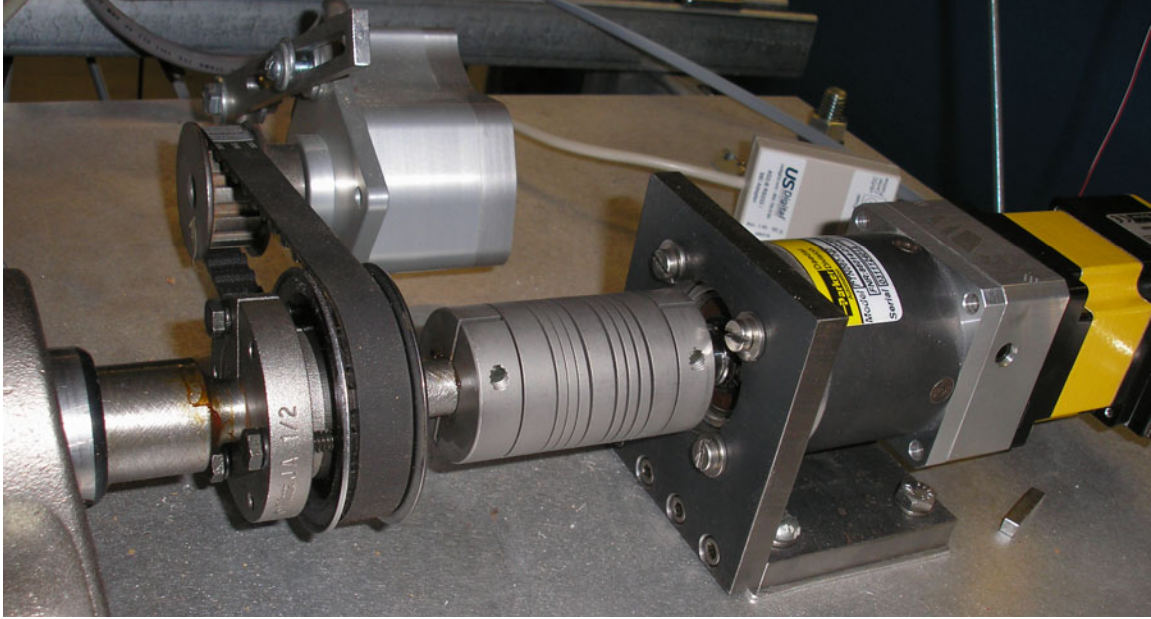


Figure 3-30. Servo unit (right), axial spring (center), AOA encoder (top), and feed through to test section (left).

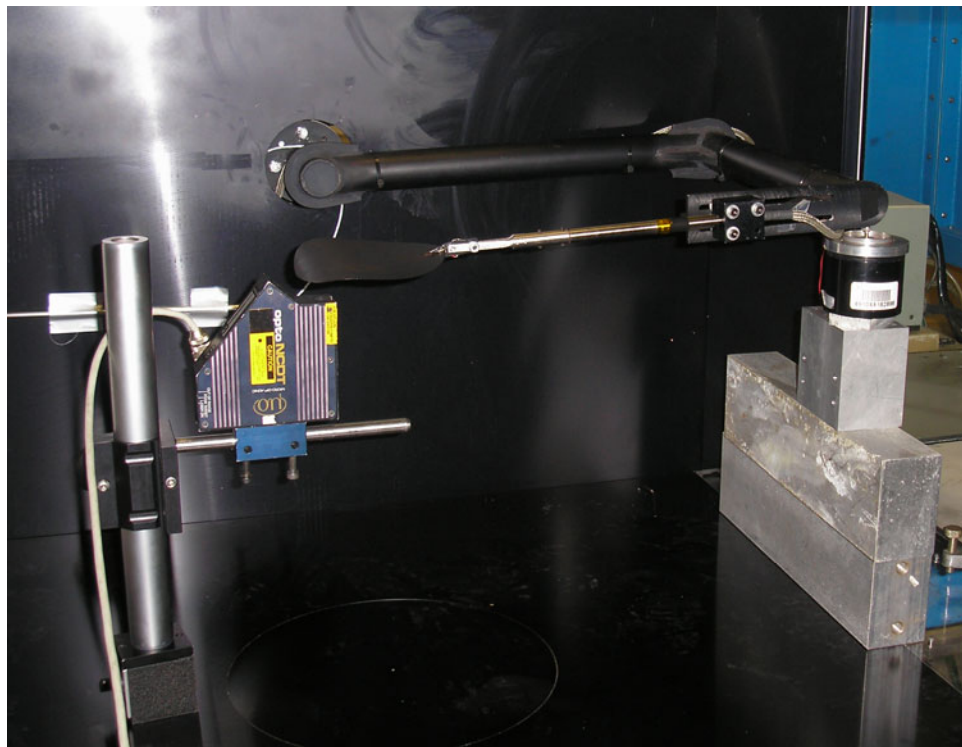


Figure 3-31. Vibrational analysis experimental setup with laser displacement sensor (left) and shaker (right).

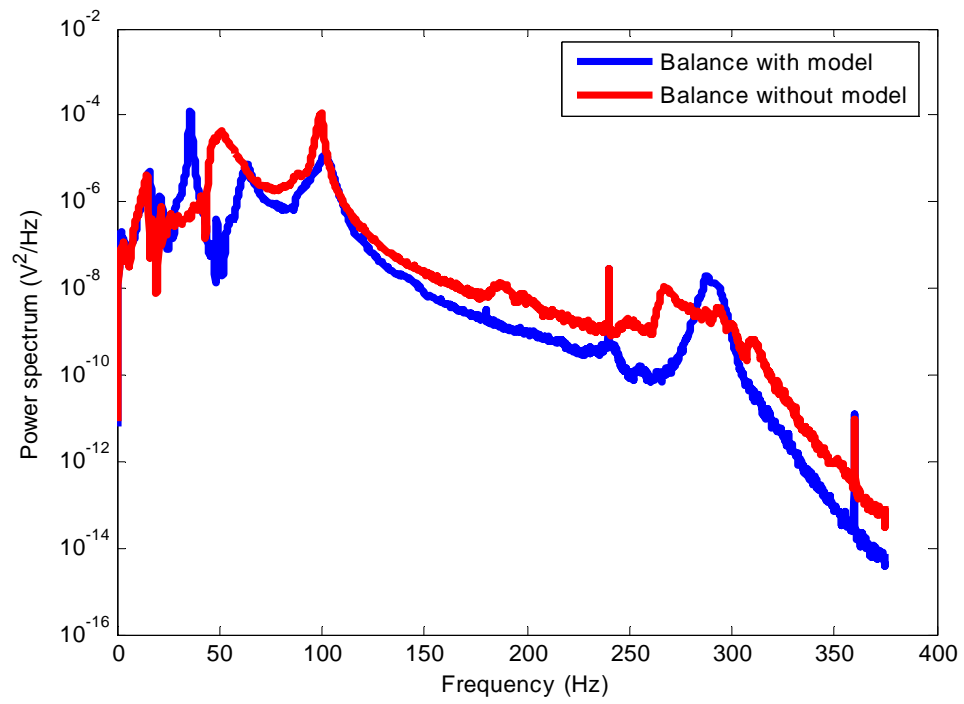


Figure 3-32. PSD plot for vibration of tip of balance with and without model.

CHAPTER 4 WIND TUNNEL EXPERIMENTATION

With the flow quality in the Engineering Laboratory Design (ELD) 407B wind tunnel known, experiments on exemplar micro air vehicle (MAV) wings will be performed. The MAV wing design will be chosen such that it closely matches designs studied by Viieru, Albertani, and also those designs used in the International MAV Competition (IMAVC). Several types of wind tunnel tests will be performed on the wing to determine characteristic aerodynamic behavior, and also to validate the usefulness and validity of such procedures. The goal of this experimentation is to elucidate the University of Florida (UF) MAV's wing flow physics and to establish procedures for the testing of future MAV designs in the wind tunnel. Finally, suggestions for the design of future UF MAV wings will be made.

Overview of Experiments

Given the capabilities and equipment available in the aerodynamic laboratories at UF it was possible to perform several aerodynamic tests on MAVs. In order to simplify the scope of experiments a single geometric design was studied for most of the tests. A specific speed of 10 m/s was chosen as the most useful MAV flight condition. This speed led the selected model to operate at a mid-span chord Reynolds number (Re) of 90,000, for which much information exists.

Loads Determination

The primary tool available in our wind tunnel has been the sting balance. The balance may be used for quick and simple determination of aerodynamic loads, and it

may be used in the quantitative comparison of different designs. The balance does not, however, provide any means of determination of the actual flow structure around the object of study.

Flow Visualization

Flow visualizations are important techniques which use different methods to clarify the motion of fluid particles so that they may be easily understood. This thesis will focus on several accepted methods of flow visualization to determine the physics of the flow around a UF MAV wing. The results of the experiments are expected to yield insight into future MAV design improvements.

Surface oil flow visualization

An immiscible fluid may be applied to the surface of a model to provide a less intrusive method of sensing the surface velocity of fluid flows. The fluid will shear under the stress applied by the flow field. In wind tunnel aerodynamics it is common to perform oil surface flow visualization. The oil travels in the direction of the airflow, and it may also be affected by pressure gradients applied over the surface [13]. In special cases the thinning rate of the oil may be used to accurately determine shear stress and, assuming Newtonian fluids and known boundary layer information, velocity [22, 22]. Pigment may be added to the oil to further show its flow properties and directions.

Surface oil flow visualization can be quite useful but suffers from several drawbacks. The oil, like any fluid, is affected by gravity and will tend to flow down an inclined surface. If the body force of the oil is not strongly overcome by aerodynamic shear force then the results of the visualization may become unclear. The flow of the oil is time dependent, hence certain oils may be more capable of rendering dynamic effects than others. The viscosity of the oil must be tailored to the expected aerodynamic shear

stress which can create difficulties in areas where the flow abruptly changes its nature [21]. The oil can also be quite messy and will often flow into unwanted areas. The oil presents a moving boundary on a surface, and hence may change the characteristics of the flow field. The oil will also tend to reduce the roughness of the surface, and it can change the effective geometry of the surface by puddling and forming waves [13]. All the same, the oil surface flow visualization method represents a useful class of flow visualizations.

Laser based flow visualization

Flows may also be visualized by adding seed particles. The seed particles should be able to maintain adequate dispersion in the flow, and ideally they should move with the fluid exactly. Seed can be added along selective dimensions or in a homogenous manner. Observation of the motion of the seed can yield clues as to the nature of the flow, but seed can often obscure itself making the visualization less useful. The seed particles are also prone to being ejected from vortices due to centrifugal force, and if not properly chosen body force can affect their motion.

The advent of the laser was followed by the appearance of many sensitive and useful laboratory apparatus that took advantage of a concentrated, coherent, and often polarized beam of light. Several different flow visualization methods rely on laser power to illuminate the flow field. Certain materials fluoresce or scatter light under the application of a laser's beam allowing visualization. Reflective, refractive, and fluorescent seed particles such as smoke or mist may be added to a clear fluid to allow visualization.

Flow may be visualized without a laser, for example by observing the smoke emitting from the cherry of a cigarette, but only highly collimated light or a laser may be

directed into a thin sheet allowing selective illumination of the particles which traverse the thickness of the sheet. This illumination may be used to simplify a complex three dimensional (3D) flow into a two dimensional (2D) case or to simply highlight otherwise obscured or invisible particles. Selective seeding may be used to allow flow structures to be highlighted. Time exposure images may be used to produce pathline photos which may be used to clarify the motion of the flow. A method called particle image velocimetry (PIV) is a laser based flow visualization method which produces quantitative velocity vector data from flow visualization images.

Overview

A wing design will be selected which is representative of UF MAVs. Loads data will be used to determine angles of attack (AOAs) of interest for a rigid wing. Surface oil flow visualization will be performed on a rigid wing to highlight aerodynamic effects occurring on the wing surface. Laser flow visualization will be used to highlight and elucidate characteristic flow behaviors. A comparison will be made between a rigid and PR wing in an attempt to explain its beneficial flow qualities.

Model Selection

It was necessary to choose a representative wing geometry to focus on because of the number of experiments planned. The wing was chosen to be without the effects of fuselage or motor to simplify experiments and also to make experiments comparable to those performed by Albertani and Viieru [7, 8]. Both Albertani and Viieru studied wing geometries used by the UF MAV Team in IMAVC competitions. Modern UF MAV designs used in the IMAVC have been low aspect ratio (LAR) wings with a Zimmerman planform [3, 4, 5]. The Zimmerman planform is characterized by a circular trailing edge (TE) and a blunted leading edge (LE). This design allows the propulsion unit to be

configured in a tractor configuration without increasing the maximum dimension of the aircraft, which becomes the span of the wing. This design also increases the possible area of the wing. The selected wing will have a Zimmerman planform designed similar to UF's 2004 entry to the IMAVC as seen in Figure 4-1.

The wing will use the same airfoil as the one entered in the 2004 competition (Figure 4-2). This airfoil is also one studied extensively by Albertani [7]. The airfoil has reflex in order to negate the pitching moment [3, 4, 5, 7]. The airfoil is applied to the planform in the following manner. The airfoil was entered into ProEngineer and extruded straight into the third direction to create a curved plate. The planform was drawn normal to the plate so that the LE at the center span met the beginning of the plate, and the center span TE met the end of the plate. An operation was applied to cut the planform out of the airfoil plate section. This process yields a wing which has the reflex applied on the very rear part of the TE only, and the downward curvature of the LE gradually decreases out across the span.

MAV wings also typically use dihedral to aid roll stability [3, 5, 7]. Laser flow visualization experiments would yield more favorable results when reflections from the wing were minimized. The dihedral of some wings which were tested forced the camera to be angled to see the entire flow field, or the camera would miss much of the wing's surface flow. The angling of the camera caused the pictures to be overexposed and the particles obscured. It was decided to use a wing design with no dihedral to assist in laser based flow visualizations. The lack of dihedral allowed for an unobstructed view across the span of the wing which also reduced overexposure significantly.

UF MAV wings typically use a flexible design which aids in dynamic gust suppression. The flexibility of the wing is a product of manufacturing methods and brings difficulties in reproducibility. Two flexible wing designs exist which have been used by the UF team at the IMAVC [3, 4, 5], and they have been extensively studied [7]. The batten reinforced (BR) wing is characterized by a rigid center section and leading edge. Flexible battens are attached to the LE, and a 0.02 mm latex membrane is adhered to the battens and rigid parts of the wing. The battens enforce the airfoil shape along the latex, but they are flexible and affect adaptive washout to the wing. The perimeter reinforced (PR) wing has a similar rigid center section and LE, except a rigid piece of material extends around the perimeter to the TE of the wing. This space is covered with the latex which yields a drum-like surface. A comparison of the PR, BR, and rigid wings is shown in Figure 4-3. The flow behavior of the PR wing was of most interest due to its strange effective airfoil shape in flight, as seen in Figure 2-5. It was likely that the BR wing would mimic the basic flow patterns of the rigid wing, but the adaptive washout effect would likely decrease the severity of any adverse flow conditions. It was important to study all three wing designs, but most focus was applied to the PR and rigid wings in the interest of time.

The wing was chosen to sit at the edge of the definition of a MAV with a 15.2 cm span and a 12.7 cm root chord. The rigid part of the wing was crafted of 2 layers of bi-directional carbon fiber reinforced plastic (CFRP) laid up on a precision mold machined by a computer numerically controlled milling machine. The CFRP was oriented so that its fibers were $\pm 45^\circ$ with respect to the span line. The CFRP composite was the same thickness as that used on IMAVC entries, an average of 0.46 mm, and it resulted in a stiff

and strong laminate, compared to expected aerodynamic forces. It was desirable to mount the wing from its center span TE to avoid flow obstruction and allow visibility down both sides of the wing. The wing was not stiff enough to support itself from the TE alone so the wing was stiffened along its centerline. Several extra layers of CFRP were added to the inner 20 cm of span so that the wing consisted of 5 layers at the TE attachment point, and 4 layers extended to the mid chord. The LE at the centerline was 3 layers thick.

The model was created by applying the pre-impregnated CFRP to the release treated mold. The top of the CFRP was covered with Teflon® release film to lock in the excess resin. The CFRP was supplied with a precise resin content, hence trapping the resin increased the reproducibility of the process. The mold was placed into a vacuum bag and the interior pressure reduced to 0.1 Atm. The bagged mold was placed into a precision heating unit set at a temperature of 120° C for 4 hours. Once the cure cycle was complete the wing was removed and allowed to cool under vacuum to prevent warpage.

The wing was removed from the bag and excess material was ground off against another reference wing. The LE was hand sanded with 220 grit sandpaper until it was devoid of burrs. Attempts were made in the sanding process to yield a smooth, symmetric elliptical shape on all edges. This part of the process certainly introduced reproducibility concerns, but it was very difficult to gauge the actual resulting edge geometry.

The wing was then compared against the mold to detect warpage in the post cure CFRP. Warpage in the CFRP stems from many factors. The largest cause of warpage was found to be fiber misalignment. If the 2 layers were not pressed onto the mold at 0°

with respect to each other warpage would almost always occur. Another cause of warpage was the bi-directional fabric being skewed from the 0/90° orientation it was supplied as. Tows in the cloth were not always woven straight which would also cause warpage. Finally, if the model were removed from the mold while it was still hot warpage would result because at high temperatures CFRP is a plastic material.

Any wing which did not adequately compare against the curvature of the mold was discarded. If any edge of the wing at rest was warped off the mold by more than 2 mm it was discarded. If the wing could be pressed down into the mold by more than 5 mm it was discarded. Only a few wings passed these strenuous criteria, but it was necessary to ensure reproducibility of results if different models were to be used on different tests.

After passing the warpage tests the TE and center span of the wing was located. A 5 mm wide and 1 cm long slit was cut along the center span into the TE. A 3 cm long by 1.5 cm wide piece of straight 7 layer CFRP was glued into the TE slit. Holes were drilled into this CFRP holder to allow the wing to be mounted to the wind tunnel's sting balance. Figure 4-4 shows a rigid wing readied for surface treatment.

The surfaces of the models were treated differently dependent on application. Every effort was made to avoid removal of CFRP material which would increase flexibility. The top side of the wing had a bi-directional weave pattern characteristic of all CFRP MAV wings. The primary models used for study were lightly sanded and filled to reduce the intensity of the bumpiness. A competition MAV would have been similarly sanded to reduce bumps, but the sanding process without filling would have removed CFRP material. The model was then painted matte black to reduce laser reflections.

Surface roughness was certainly a reproducibility and flow concern, but every attempt was made to craft models very much like competition aircraft.

A PR wing was crafted by removing material so that a 60 mm center span rigid area remained, and a TE perimeter thickness of 4.0 mm was preserved. The latex was applied with an amount of tension that had been empirically determined to create airplanes that flew well. The tension of the latex was a huge reproducibility concern as was its proper application. It was very difficult to judge if the latex had been applied with uniform tension, and after applications ripples in the latex would often form requiring a recoating. The latex degrades due to handling and exposure to light, hence it was difficult to be consistent with any PR wing model.

The BR wing models were crafted by adding an extra step to the layup process. Six strips of 5 mm by 0.5 mm unidirectional CFRP were applied to locations along the rigid leading edge before the model was cooked. The excess CFRP was similarly removed, and then the latex was applied with very little tension as has produced aircraft with favorable flight qualities.

Loads Determination and Analysis

In this section the loading characteristics of the rigid wing model will be determined. The loading characteristics of the models will be discussed, and AOAs of interest will be selected. The loads characteristics of many rigid, BR, and PR wings have already been extensively studied by Albertani [7], and hence it was deemed unnecessary to repeat the experiments. The purpose of the loads analysis for the rigid wing was to determine AOAs of interest for a detailed oil surface and laser sheet visualization study.

Experimental Setup

Aerodynamic loads data were generated using a LabVIEW VI interface to the Aerolab balance. A model is first mounted on the balance and its initial AOA was determined using a AccuPro Pro360 digital inclinometer. The inclinometer has an angular resolution of $\pm 0.05^\circ$ so care must be taken to ensure that the AOA readings are repeatable. The definition of AOA for reflexed MAV wings has been established by Albertani [7] as the angle measured between the center span LE and the point of maximum reflex. The Pro360 inclinometer reports angular difference between its longitudinal axis and the gravity vector. The AOA was read by gently pressing the balance against the bottom side of the wing so that it was in contact with the LE and maximum reflex point. Care was taken to avoid deflecting the model with the inclinometer, and multiple readings of the inclinometer were read until a converged AOA was determined. The AOA was referenced to the test section ground plane which was 0.1° from being perfectly normal to the gravity vector.

The wing also had to be centered in the roll axis so that its span line was parallel to the wind tunnel floor. Inaccuracies in centering would cause a component of the lift vector to be misinterpreted by the sting balance as side force. The model had to be accurately created so that the CFRP holder it was attached to did not cause any yaw angle to be present when the model was mounted. This was a difficult condition to establish, but errors were reduced by making measurements of the center span line from the wind tunnel wall. The sting balance itself was centered in a similar manner within the wind tunnel.

Loads determined using the Aerolab sting balance were susceptible to errors because the balance was designed for much larger loads than those generated by a small

MAV wing. The balance was also susceptible to electronic drift during an experiment. As such, it was necessary to repeat experiments multiple times to determine the most suitable and correct data. Small disturbances in the experimental procedure resulted in invalid data, and care had to be taken to ensure that the sting was operated in thermal equilibrium. A trend was observed where after several identical experiments the loads data would eventually converge into similar values.

The loads estimation procedure involved gathering wing AOA measurement, encoder AOA measurement, LE length and quarter chord length measurements to a fixed point on the balance. The reference area of the model must also be known. A tare matrix was first gathered by the balance control VI. The model is swept through a set of AOAs with the airflow of the wind tunnel deactivated to determine the static loads created by the model. After a tare has been gathered the VI is run with the airflow activated. The VI then determines the aerodynamic loads at the AOAs requested and saves the data. The data output from the balance are nondimensional force and moment coefficients referenced against AOA. The moment data are referenced about the quarter chord location.

The tare data and loads data are saved with standard deviations of the measurements taken. A separate VI was used to determine uncertainties in the data based off of the saved data and estimated uncertainties in area calculation, measured lengths, and pressure transducer error. The uncertainties in loads estimation were plotted as error bars on the loads data, and it appeared that vibration of the model served to increase the error bounds substantially.

Given this information it was understood that the loads data for very small MAV wings, while being realistic qualitatively, may not have been perfectly accurate in a quantitative sense. The drag component of the balance was shown to be especially prone to errors in quantitative values, yet it would consistently yield the same qualitative trends over AOA.

Loads Data

Loads data were gathered at a wind tunnel velocity of 10 m/s using different increments in AOA. An iterative process was used to determine interesting features in the AOA variable space. The final loads data gathered used AOAs chosen to highlight specific flow regimes. The data presented was deemed the best out of a series of experiments, and both qualitative and quantitative information were found to be in agreement with other tests.

A plot of lift coefficient vs. AOA is shown in Figure 4-5. Figure 4-6 shows the drag variation over AOA, and Figure 4-7 shows pitching moment variation over AOA. A plot of lift coefficient vs. drag coefficient was prepared and is presented in Figure 4-8.

Discussion of Loads Data

The lift was approximately linear from an AOA of 0° up to 10° . Beginning at an AOA of 8° the wing was vibrating when the tunnel was activated. The vibrations of the wing were on the order of ± 1 mm, and other models used by Albertani and tested by the author had similar vibrational patterns. This vibration appeared to increase the error in the loads data, and at AOAs with large vibration displacements the error bars were large. The large error bars present in the data obscured accurate interpretation of the loads results of a single experiment, however certain trends were observed across multiple sets

of loads data. These trends will be presented, but it must be understood that strictly speaking the large error bars essentially invalidate any of the following observations.

Between AOAs of 10° and 15° the results seemed to vary, but between 15° and 16° it appeared that there was a change in the slopes of the lift and drag plots. Specifically, the drag decreased subtly in that region. The drag was larger at a zero lift AOA than it was at a lifting AOA, hence the cause of drag, if not induced, warranted further study. A primary stall was observed starting at an AOA of 22° to 23° , and a secondary stall was observed starting between 28° and 29° .

Strange behavior was occurred between 18° and 19° AOA. The behavior was explored extensively and the loads data was found to change between an AOA of 18.4° and 18.9° in a highly repeatable manner. When transitioning between these AOAs the wing would vibrate strongly, and the higher AOA had very much less vibration than the lower AOA did. It was noted that within this highly vibrational region it was likely that the effective AOA was changing considerably.

This behavior was subject to 0.7° of hysteresis. Lowering the AOA from 18.9° to 18.2° was sometimes necessary to initiate the conditions experienced at 18.4° , and raising the AOA to 19.1° was often necessary to achieve the conditions present at 18.9° . This effect seemed to center around 18.65° , but at this AOA setting the model vibrated greatly thus changing AOA in the vibration. It was uncertain if the vibration caused the change in flow, but tests on other rigid models had pre stall vibrations on a similar order, hence tests were continued on the same model.

Around 18.65° the drag decreased a great amount as the AOA was increased, and the pitching moment increased abruptly. A small increase in lift was also observed. This

behavior will be referred to as the ‘drag divergence,’ and precedence of such behavior on rigid model was present in Albertani’s work [7]. This behavior was of interest to the author and warranted further study.

The pitching moment behavior of the wing was unwanted. A MAV should have a zero or small pitching moment to maintain steady flight. The small positive pitching moment showed at AOAs less than the drag divergence could easily be nullified by a pilot using elevator trim. However, if the pitching moment of an aircraft changes abruptly over a small AOA range piloting can become difficult. It should be noted that UF MAVs do not use rigid wings such as the tested model, and perhaps the pitching effect is part of the reason for that.

Vibrational Exploration

All data gathered at or less than the drag divergence AOA had large error bars, most likely because of the vibrating behavior of the model. Above the drag divergence the model would vibrate very little, and hence the associated error bars were small. It seemed important to study the vibrations of the specific model studied for completeness, hence a separate experiment was performed to determine oscillatory loading on the wing.

A strain gage was affixed to the top surface of a wing model just forward of the piece of CFRP used to mount the model. The gage was electrically connected to a Vishay P-3500 unit to read the strains. The P-3500 was configured to output a voltage signal which was linearly proportional to the strain. The actual value of the strain and voltage were not calibrated to deflection as only the vibrational characteristics of the wing were being studied. The P-3500 unit was connected to the VXI frame with a Bayonet Neill Coleman cable.

The signal output from the P-3500 had significant influence of 60 Hz line noise even though it was battery powered. The VXI machine was configured using the same settings as for the sting balance vibrational experiment in anticipation of similar behavior. The model was mounted in the tunnel and the tunnel speed brought to 10 m/s. The model was brought through an AOA sweep, and power spectral density (PSD) data was gathered at each AOA. A PSD plot of the strain gage's signal and baseline signal are shown in Figure 4-9.

The strain gage PSD plots showed three predominant vibrational modes. The first mode was very low frequencies, the second mode centered around 40 Hz, and the third mode was around 100 Hz. The apparent modes at 60, 120, and 240 Hz were disregarded as line noise. The PSD data from the AOA sweep was summed for frequencies of 0 to 20 Hz, 30 to 50 Hz, and 95 to 105 Hz and divided by the number of PSD bins to yield an average power spectra (PS) per signal metric. This data was plotted against AOA to yield Figure 4-10.

The results reinforced the vibrational experiment performed on the sting balance with model. It appeared, however, that the actual vibration of the balance around 100 Hz had a small influence on the overall vibration of the model. The natural frequency of the model, previously found to be around 36 Hz, appeared to dominate at AOAs less than the drag divergence, but it was much less significant after the drag divergence. The levels of vibrational power reinforced the error bars of the loads data by indicating a similar behavior across AOA. This information brought under question the interaction between model natural frequency and flow interaction.

Selection of AOAs of Interest

The AOA behavior of the loads data was considered and eleven AOAs of interest were identified for study. The AOAs are listed in Table 4-1 with a brief explanation for their choice. Most of the studies presented in this chapter of the thesis will focus on the study of the rigid model at these selected AOAs at 10 m/s.

Oil Surface Flow Visualization

This section will detail the surface oil flow visualization performed on the rigid MAV wing model. Results will be presented and discussed based on observations of the patterns in the oil. The surface flow visualization technique relies on the shear behavior of an immiscible fluid in response to another fluid's motion. In the wind tunnel, oils are used as surface coatings with tailored viscosity to appropriately respond to airflow. The oil may be applied continuously or spread as spots across a surface and flow patterns observed. The continuous oil application method was used to highlight significant flow features on the representative MAV wing.

The surface oil visualization was attempted on the flexible wing designs, but the white latex caused problems in proper visualization such as overexposure of the camera and poor flow properties. Painting the latex black caused the elastic properties of the flexible portions to change, hence the results would not necessarily be applicable to all flexible wings. Exposure to intense ultraviolet (UV) light degrades the latex rapidly, hence illumination of a fluorescent material would ruin models very quickly. Black carbon dust pigment was tested on an unpainted latex wing and blackened the entire surface very quickly. The latex was difficult or impossible to properly clean. Pigment adhered to the latex and stop moving with the oil flow, and solvents such as acetone would damage the latex and loosen the adhesive which held it in place. Tests on a rigid

wing which was painted also experienced problems with particle flow, and pigment would become trapped within the surface roughness making cleaning difficult. It was surmised that the oil must be applied to a surface which is very smooth, easy to clean, and did not have any chemical attraction which would immobilize pigment or change flow properties.

Experimental Setup

A rigid wing model was prepared as per the model selection section and the surface was lightly sanded. Self adhesive, heat shrink shiny black Mylar® film was applied to both surfaces of the model using a small iron. The excess film was trimmed to preserve the sanded shape of the CFRP edges. The model was placed in the wind tunnel attached to the dummy balance so that the oil would not damage the sting balance. The model was aligned in the tunnel so that its AOA was known.

Polydimethylsiloxane (PDMS) oils supplied by Dow Corning with different viscosities were used for this test. Olive, vegetable, and mineral oils were tested with poor results. Water and water mixtures also did not yield decent results. PDMS oils with a viscosity ranging from 0.5 cp to 1000 cp were tested on the wing for appropriate shear characteristics. The extremely low viscosity oils evaporated rapidly, and oils with a viscosity higher than 400 cp showed little to no response to free stream velocities of 10 m/s. Oil with a viscosity of 100 cp was selected for tests because it was capable of staying stationary after application but would flow under a free stream velocity of 10 m/s. Fluorescent orange pigment powder was added to the oil to aid visibility.

Oil was applied to the wing continuously and as spots. The spots, however, had difficulty flowing under low speed air conditions because of the resistance due to surface tension, when applied to a clean wing. When applied to a wing which had been pre-

wetted with clear oil, the pigmented oil dots spread and obscured their boundaries quickly. Results were obtained using the spot method, but they will not be presented in this thesis due to their low quality.

The oil was applied continuously to the wing with a cotton swab so that the entire wing had a uniform thickness of oil on it, similar to surface flow visualizations performed by Selig [14]. It was important that the pigment not be too liberally mixed else it would affect the flow properties of the oil. The pigment, however, needed to be evenly suspended in the oil at the time of application. A high intensity ultraviolet light was directed into the wind tunnel so that it would illuminate the oil and pigment on the side of the wing facing the camera. A Nikon D70 digital single lens reflex camera was used to capture pictures of the wing from outside the wind tunnel.

It was noticed that the oil flowed off the wing rapidly when angled at high AOA. More and less viscous oils were tested but showed insufficient response to air flows, and they also flowed off the wing. The effect of the oil dripping off the wing at high AOA was a limitation of this method. The bottom side of the wing was tested using this method but the oil pooled excessively in the cambered region for all but the highest AOAs. For this reason no data will be presented on the bottom surface visualization. The excess oil applied dripped to the tunnel floor and was cleaned after every run. The wind tunnel was immediately brought to 10 m/s after the oil had been applied, and sufficient time was allowed for the oil to settle into patterns. The pictures obtained of the oil flows were modified to increase the contrast of the pigment and aid understanding of the structures.

Results and Discussion

The oil surface flow visualization technique was tested against all AOAs of interest. The results will be presented and discussed in this section. The wing was tested at an AOA of 0° and the resulting image is shown in Figure 4-11. Two characteristic lines were present in the oil which ran the span of the wing. The lines were a buildup or pooling of the oil toward the quarter chord of the wing indicating reversed flow on the TE line and a separation occurring on the LE line. It was theorized that the TE line represents a reattachment, and hence the area between the lines was a representation of the laminar separation bubble. The lines did not extend to the wing tips. If the oil indeed was a separation bubble, it would make sense that the bubble would not extend to the wing tips because the energy brought to the flow by the tip vortices would prevent formation. Also, the tips of the wing operate at a much lower Re regime, hence changes in wing tip flow pattern were to be expected.

Figure 4-12 represents the wing at AOAs of 5° and 10° respectively. Each wing showed a similar pattern with a LE line and curved TE lines. The TE lines were curved away from the center span TE, the area of maximum reflex. If these lines do indeed represent the extents of the laminar separation bubble it would make sense that the flow does not reattach at the reflexed area at these AOAs because of the pressure gradient generated. Pooling of the oil at the TE was noticed in multiple runs of the 10° case and could not be avoided. It was suspected that this reduced the effective reflex in the area. The lines were again noted to not extend to the wingtips indicating that the flow at the tips is characteristically different from the flow over the main portion of the wing.

The wing was then tested at an AOA of 16° as shown in Figure 4-13. A weak line was formed downstream of the LE, and close behind it was another line. The line closer

to the LE followed the pattern of the LE line in Figure 4-12-B, hence it was presumed that they were similar phenomena. Another formation was noted at the very LE wing tips for this case. Small regions of oil had pooled at the wing tips, indicating that perhaps the LE was separating in that area. Multiple photographs were taken for the AOA of 16° case to attempt to clarify the LE formations, but the oil flowed off the wing very rapidly which robbed the LE areas of fluorescent particles.

The wing was photographed at AOAs of 18.4° and 18.8° . The 18.4° case was an extension of the two lines visible in Figure 4-13. The oil dripped off the wing so quickly, however, that the photos could yield less information. The LE lines coming from the wingtips increased in the 18.4° case, but they did not yet extend across the full LE. The images gathered over 18.8° were not repeatable, and this was assumed to be because of the moving nature of the oil. It was likely that the decreased shear stress generated by the oil at the center span LE caused the drag divergence phenomena to occur differently than it did in the case of a dry wing. An image at an AOA of 21° will instead be presented as this was an AOA which produced repeatable results. Figure 4-14 shows the wing at an AOAs of 18.4° and 21° . It was noticed at the 21° AOA that the line extending from the wingtips had progressed across the full length of the LE.

Figure 4-15 shows the wing at AOAs of 23° and 30° . The 23° case was expected to be transitioning into stall, and by 30° the wing was expected to be fully stalled. The images were difficult to assess because the oil flowed down the wing so rapidly, but it was clear that the 23° wing had an asymmetric flow pattern involved with only one side of the wing characterized by the LE oil line. The 30° case did not show any LE lines, but this case was difficult to assess due to the speed with which the oil flowed off the wing.

Discussion of Results

It was clear from the oil surface flow visualization that the wing is characterized by different stages of flow. Low AOAs are theorized to be characterized by long laminar separation bubbles. As the AOA increases the long separation bubble decreases in chord length and also along the span. The tip vortices are assumed to be the cause of the span wise length change. Increasing the AOA brings about the formation of LE behavior at the wing tips that work toward the center span as AOA increases. This LE behavior is possibly a short laminar separation bubble. The very high AOA cases were difficult to obtain data due to the rapid flow of the oil down the surface of the wing, and it was possible that the oil on the surface changed the aerodynamic characteristics of the wings. These exact characteristics should be validated using other methods to verify that the oil on the wing did not change the results sufficiently to otherwise invalidate the data.

Laser Based Flow Visualization

This section will detail the laser flow visualization experiments performed on the MAV wing model. Several types and orientations of laser flow visualization will be presented. All methods will rely on the reflectivity and refractivity of seed particles in the flow. The seed was spread homogenously through the flow and selectively placed. The laser sheet was oriented parallel and perpendicular to the flow, and both continuous and pulsed lasers were used.

Basic Experimental Setup

The basic form of the laser flow visualization technique involves spreading a laser beam into a thin sheet using a lens. The sheet is directed into the test section to illuminate a plane of interest. Seed particles are introduced to the test section, and a camera is focused onto the illuminated seed. The resulting photographs of the

illuminated seed show the motion of the seed and the fluid. A diagram of the setup for a span wise visualization is shown in Figure 4-16. A span wise visualization is named as such because the laser sheet may be traversed across the span of the wing.

Continuous Laser Flow Visualization

This set of experiments used continuous laser spread into sheet and a seeder to visualize the air flow. A localized seeder was used to visualize wing tip vortices in a chord wise visualization. A chord wise visualization allows the laser sheet to be traversed across the chord of the wing. A detailed span wise visualization using homogenous seeding was then performed which visualized in vivid detail the behavior of the air flow over the center span of the wing. A span wise visualization using local seeding was then performed to highlight the flow differences between a PR and a rigid wing.

Rigid wing chord wise visualization

The first set of experiments presented used a model and laser sheet oriented as shown in Figure 4-17. This experiment was performed on a rigid model to mimic Viieru's wing tip vortex visualization shown in Figure 2-4. Images were gathered used a Nikon D70 camera and a 60 mm AF Nikkor lens. The camera was attached to a rigid stand and placed inside the test section. A Model 95 Lexel continuous argon-ion 4.0 W laser was directed through a 1000 mm biconvex lens and a 5.0 mm glass stirring rod to create a laser sheet which was widely spread across the test section. The divergence of the sheet was large and hence could illuminate a large area, however the intensity of illumination was very low which required a long exposure for the camera to properly visualize the flow (Figure 4-18).

The laser sheet was directed into the test section using a mirror which could move along the X axis, allowing the plane of illumination to be placed in any chord wise location. The laser sheet was oriented so that its normal vector was parallel with the incoming velocity vector. Multiple planes of interest were studied in the X direction, but wherever the laser contacted the model caused an overexposure of the photographs. It was decided to gather photographs with the laser sheet placed at the very TE of the model as it provided a convenient reference point for future observations.

The particles passing through the laser sheet had a very short time of transit, hence an even distribution of seed was able to yield little useful information. A localized seeding method was therefore necessary to highlight interesting areas of the flow. A seeder was designed which could sit inside the test section and be moved by hand. The seeder consisted of a 10 mm polyvinyl chloride (PVC) tube with a cap at one end and a streamlined piece of aluminum tubing extended up above the capped end (Figure 4-19). An incense stick was held inside the tube from the cap. Small holes were drilled in the TE of the thin aluminum tubing, and tape was applied in the region of the holes to make a more smooth transition which increased smoke line integrity. The open end of the PVC tube was pointed upstream and the incense was lit. The difference in pressure between the upstream uncapped end and the holes in the aluminum tube caused air to be drawn out through the TE holes, essentially creating a line of smoke that was locally emitted in the tunnel.

This line of smoke was moved over many locations over the wing. The most interesting feature was the wingtip vortices. When illuminated by the laser sheet, the vortex formations were made visible by the deformations to the smoke line. The smoke

line was placed directly upstream of one wingtip, and the Nikon D70 camera was placed in the tunnel 1.0 m downstream of the wing. The lens of the camera was oriented to be directly downstream of the wingtip, and the camera was wrapped in plastic to protect it from contaminations. Photographs were only gathered of the left wing tip as the right wing was obscured by the model arm. The experimental setup is shown from the point of view of the seeder in Figure 4-20.

Pictures of the warped smoke line show the nature of the wingtip vortex. The warping of the smoke was negligible at zero AOA, however a swirl pattern quickly emerged as the AOA increased. The diameter of the vortex increased with AOA, and it was relatively stationary. Pictures were taken with a 0.25 s exposure, and at AOAs less than the drag divergence the smoke jumped around a great deal, blurring the vortex pictures. Beyond the drag divergence, however, the warping of the smoke line was very constant yielding a well defined vortex shape. Beyond stall the smoke line was pushed outward from the wing, and the vortex shape was lost. As was to be expected, the stall pictures were blurred by the moving location of the smoke line. Images of the vortices are shown in Figure 4-21.

Rigid wing span wise visualization

The second set of experiments presented used a model and laser sheet oriented as shown in Figure 4-16. Images were gathered used a Nikon D70 camera and a 200 mm AF Nikkor lens. The camera was attached to a 3-axis Parker traverse and motion controller system to accurately change the position of the camera. A Model 95 Lexel continuous argon-ion 4.0 W laser was directed through a 1000 mm biconvex lens and a 25.4 mm semicylindrical lens to create a laser sheet which was focused on the center span plane of the model. The divergence of the sheet was small and hence could only

illuminate a small area, however the intensity of illumination was very high which allowed the camera to properly visualize the flow.

This experiment focused on determining the detailed flow field of the rigid wing. The experiment was incredibly time consuming and was not able to be performed on the flexible wings. The white latex of the flexible wings caused over illumination of the particles which obscured the particles in the plane of interest. It was important to validate and clarify the meaning behind the surface oil visualizations, which only involved the rigid wing.

The laser sheet was directed into the test section using a mirror which could swivel, allowing all of a plane of the tunnel to be selectively illuminated. The sheet was oriented parallel to the incoming flow and parallel to the gravity vector. The entire laser and optic setup could be accurately moved across the Y direction of the tunnel to illuminate planes of interest. Multiple planes of interest were studied in the Y direction, but the oil surface flow visualization results showed that the effects of interest were approximately constant across the span up to a certain point near the wing tips. It was decided to study the phenomena occurring along the center span in detail as an indicator as to the nature of much of the flow over the wing.

The sheet was carefully aligned so that it was exactly centered in the test section as shown in Figure 4-16. The gravity vector determined from the inclinometer was used as a reference to properly position the camera. The 200 mm lens allowed a high level of zoom which was necessary to visualize small seed particles. The lens, however, had a focal plane with a thickness on the order of a millimeter; hence the camera had to be meticulously aligned in order to achieve focus all across the field of view. The traverse

which the camera was mounted on was aligned perfectly with the laser sheet so the camera could move and maintain focus all over the area of interest without refocusing. The laser sheet was easily swiveled so that the sheet would expose images with an equal intensity.

There existed no method of introducing seed into the tunnel upstream of the model at the time of the experiment, hence the seed had to be injected elsewhere. It was decided that the tunnel should not undergo any permanent modifications, so the seed was injected through the hole in the test section floor plate. A hatch was fabricated to allow a pipe to inject seed into the test section. The floor plate with the hole was placed downstream of the model arm to avoid flow interference. This setup necessarily required the seed to circulate all the way around the wind tunnel before reaching the model.

Several types of seed particles were tested. Propylene glycol fog emitted from a LeMaitre G150 fog machine was tested first. The device heated a mixture of propylene glycol and water near its boiling point and forced cold air over the surface of the liquid. The result was a nontoxic fog which could be controlled in density and volume. The fog was composed of very large droplets which were prone to coating the tunnel. The fog, once injected into the test section, could only circumnavigate the tunnel three or four times until it had adhered to the tunnel and exited the flow. This represented about 20 seconds of proper seeding per injection. This seed represented a poor choice because it would quickly sully the entire tunnel and require constant cleanup. The fog also coated the windows of the test section quickly. A seed was required which had a long persistence in the tunnel and that was not so messy.

Incense was then burned in the tunnel to create a non-toxic smoke which was well illuminated by the laser sheet. The smoke had a long persistence in the tunnel, often lasting 15 minutes of continuous run time. The smoke particles viewed from the camera, however, were exposed on the order of two pixels at maximum zoom. This small particle size required large amounts of smoke for practical visualization, and burning that much incense in the tunnel was impractical and also made everything smell very bad. It was decided that some other seed particle had to be used.

A LeMaitre Neutron XS haze machine was located which operated by vaporizing paraffin oil into cool air. The paraffin oil was also non-toxic, and tests in the tunnel showed a longevity of 5 minutes or more per application. The haze was composed of small particles which were not very dense. The particles were not prone to coating of the windows, and only a small portion of fluid was necessary to properly seed the tunnel, unlike the fog. The particles when imaged were 3 to 4 pixels in diameter at maximum zoom which provided ample light scattering capabilities. The haze was mixed with almost perfect uniformity in the flow.

Many camera settings were tested to visualize the particles at different zoom levels. All the particles tested did not expose particularly well when traveling at 10 m/s. Short exposures suffered from lack of light, while long exposures were blurred over. A view of the wing's whole chord was desired, and the camera was aligned to fit the whole wing into its field of view. It was quickly found that the rate of passage of the particles caused them to overlap each other on exposures longer than 1/25 of a second. In that time, the flow will have traveled three chord lengths re-exposing the same streak lines. The camera focused so far out, however, was unable to expose the particles even with the

highest sensitivity setting and largest aperture. Static particles were sub-pixel in diameter. It was therefore necessary to zoom in to achieve a better exposure.

The camera was then mounted so that its lens was almost touching the glass of the test section, achieving maximum possible zoom. At this point a decent exposure could be gathered with exposure times ranging from 0.01 s to 0.017 s. The lens was at its highest aperture and the camera set at highest sensitivity. Longer exposures would yield the blurring effect, but these short exposures were capable of accurately rendering the short time pathlines of the seed particles.

The high level of zoom, however, required multiple images to be gathered. In order to fully render the chord wise variation, 7 images had to be captured and stitched together. The far field of the flow was of interest, hence 3 images had to be captured in the vertical direction. The laser sheet could not pass through the wing, and hence the bottom of the wings was not illuminated. A separate set of bottom side pictures had to be gathered. This led to a total of 34 images to be gathered at each AOA to yield a complete picture of the flow field.

Calibrated spacing of the camera was required for the images to be able to fit together properly. Images were gathered of a calibration plate with holes etched in it at precision intervals. A Matlab code was used to accurately determine a calibration relating pixels of the camera's focused plane to a length in meters. This camera calibration was used with the supplied traverse calibration to select image locations so that each image had a known offset from other images. A series of locations was determined which would allow the full field of interest to be viewed.

The camera was traversed to a location and the laser sheet was aligned to provide optimum lighting. Pictures were taken through an angle of attack sweep. The numbering of the pictures was referenced to AOA and traverse location. Seed was injected as necessary to provide adequate visibility. After the pictures of each AOA sweep were taken the traverse moved the camera and the next image set was taken. A picture of the author measuring model AOA is shown in Figure 4-22.

This process created over 375 images for the 10 m/s case alone. A Matlab code was used to automatically sort and rename the image files according to AOA and location. The GNU's Not Unix (GNU) Image Manipulation Program (GIMP) was used to post process the images and stitch them into full field mosaics. The pathlines visible in the images were still extremely faint and indistinct. Each image was 5 Mb and computer memory limited the amount of images that could be shown on a single mosaic. A process was discovered which increased the fidelity of the pathlines and allowed the images to be shrunk to take up less memory.

Each color image was first converted to 8 bit grayscale mode. The images were processed with a GIMP plug-in called 'Neon.' Neon is an edge-finding algorithm which was found to have ideal properties for the finding of pathlines. Neon was applied to the images with a 15 pixel radius and 100 % intensity. The images were then shrunk to 25 % their size, and bottom side images were vertically flipped.

A master image was created in GIMP that had guides where each image should be placed. A GIMP guide is a line drawn on a layout that will cause images to snap to them, allowing for precision image placement. The images at each AOA case were dropped onto the guided master into their appropriate location. Misalignment of the images was

extremely small, on the order of 5 pixels, and the images were adjusted to minimize such misalignment. The mosaics were cropped as necessary, and contrast and brightness were adjusted.

This method of visualization was extremely time consuming and was effective in rendering only the 2D variations along the centerline of the wing. The resulting mosaics were stunning in their depiction of the fluid flows, but they suffered several drawbacks. The mosaics used images gathered at completely different times and hence the turbulent variations caused mismatch between frames, especially around separated regions. Cases with low levels of large scale turbulence showed a great deal of streamline matching, but the cases with large amounts of unsteady flow yielded disparate frames in the mosaic. A lens with more light gathering capability could have perhaps gathered a larger field of view at a time, but the experiment was completed using available components.

The mosaics yielded interesting information about the center span flow of the rigid wing which, viewed with the oil surface flow visualization, may be interpreted to extend across much of the wing. Figure 4-23 is the flow mosaic for an AOA of 0° . It is evident that a large laminar separation bubble is formed off the position of maximum camber, as was inferred from the oil surface visualization experiment.

The bottom side of the wing, however, appeared to be separated also. This bottom side separation explains the high drag at low AOA. The shape of the wing is such that the center span LE has the largest downward angle which decreases out toward the wing tip. Figure 4-34 is a head on image created in ProEngineer indicating the shape of the LE. Although this was not verified using other methods, it is likely that the bottom side separation effect decreases out toward the wing tips.

Figure 4-24 (AOA = 5°) shows that the bottom LE separation bubble is decreasing in size and becomes reattached much earlier than the 0° AOA case. It would make sense that the bottom side of the wing should reattach easily because it exists in a favorable pressure gradient. Figure 4-25 (AOA = 10°) shows an extension of this trend with a decreasing bottom side bubble. The top side long laminar separation bubble grew in effect vertically and changed its separation point so that at each AOA it occurs just after the maximum height of the wing. This behavior is consistent with the literature, indicating that a very small adverse pressure gradient is required to separate a low Re wing surface [10, 11, 12].

Figure 4-26 (AOA = 16°) marks the end of separation on the bottom side of the wing, and a close investigation of the image shows that the near wing air flows in a laminar fashion parallel to the top surface in the long bubble region. Unfortunately this method cannot show flow direction, but it would appear that backwards flow was feeding vortex shedding from the separation point. This could also help explain the behavior of Figure 4-13 in the oil surface flow visualization experiment.

Figures 4-27 (AOA = 18.4°) and 4-28 (AOA = 18.8°) show peculiar behavior around the drag divergence of the wing. The flow field was changed substantially from one image to the next. Figure 27 (AOA = 18.5°) showed an extension of the top side flow fields from Figures 4-23 through 4-26 (AOA = 0° to 16°). Figure 4-28 (AOA = 18.8°), however, appears to be of a completely different nature. The previous turbulent separation bubble transitioned into what appears to be unseparated turbulent flow which grows in strength from a point just downstream from the previous location of the separation bubble. Comparing with the loads data, it is now clear why the drag decreases

so sharply. The separation bubble which exerts a certain pressure drag was replaced by a turbulent boundary layer which will have a non-constant pressure applied across its length. Close inspection of the unaltered image of the LE of Figure 4-28 (AOA = 18.8°) showed the formation of a miniscule short laminar separation bubble.

Figure 4-29 (AOA = 21°) confirms the existence of the LE short bubble, and it would appear that the turbulence shed at the reattachment of the bubble is what keeps the rest of the flow attached along the length of the wing. The growth of the turbulent boundary layer must be a product of momentum mixing and the adverse pressure gradient. Figures 4-30 (AOA = 22°) and 4-31 (AOA = 23°) show an increasing thickness of the turbulent boundary layer and a decrease in streamline matching in the far field indicating more unsteady effects. Figure 4-32 (AOA = 25°) clearly shows an attached LE short bubble but a separated turbulent boundary layer. This is the first stage of the stall. Figure 4-33 (AOA = 30°) shows the second stage of stall in which the LE laminar bubble has burst, and no flow is attached to the wing except on the bottom side.

Considering that the appearance of the short LE bubble decreased drag so substantially on the model, it would make sense that other wings and aircraft which have long separation bubbles could benefit from the formation of a LE short bubble. If the bubble could be formed at lower AOA then separation induced pressure drag could be reduced. It is possible that the resulting turbulence could create comparable drag to the large bubble, but this would occur at low AOA hopefully out of the flight range.

Comparison of Rigid and PR Wings

The span wise flow visualization experiment was attempted on a PR wing, but difficulties arose which made the method unsuitable for detailed visualizations. The latex skin was bright white, and the laser contacting the latex caused massive reflections which

obscured all the particles in the vicinity. The latex was also painted matte black, but this caused two other problems. First, the elastic properties of the latex changed drastically after painting, potentially bringing error into the experiments. Second, the laser sheet was powerful enough that it would burn holes into the painted latex ruining the model immediately.

It was of most interest to study the LE behavior of the flexible portions of the PR wing to identify differences in separation behavior. In order to achieve LE visualizations, the latex was trimmed off the thick LE carbon portion of the wing so that the membrane was only supported by its very edges. This allowed the LE to be painted matte black, and a laser sheet directed at this area caused negligible reflection. It was of primary interest to study the outboard section of the wing which had an appreciable amount of latex on it. A position 40 mm out from the center span location was selected as this area appeared to have the most deformed area of latex in flight. The location of the laser sheet for these tests is shown in Figure 4-35.

The uniform seeding method did not yield acceptable results due to the increased lens flare and the reflection of the illuminated latex parts of the wing. The line seeder used to visualize the wing tip vortices was tested with interesting results. The LE separation bubble of the PR wing was made visible by the lack of particles within the bubble, however detail of the shear layer and pathlines was mostly lost. This method, however, proved successful in highlighting the outboard LE differences between the rigid and a PR wings.

It was interesting effect that the PR wing had a blacked out bubble whereas the rigid wing was seeded within the bubble. The conditions were otherwise the same, so the

difference in the pictures shows that the air flow within the separated regions come from different sources. The oil surface flow method using dots was attempted on the PR wing to find the local flow directions, but was unsuccessful. It may be of interest for future studies to determine the differences in the LE bubbles of rigid and PR wings.

LE span wise flow visualizations were performed on both a rigid and a PR wing at varying AOA at 10 m/s. The pictures gathered from the experiment showed that the PR wing forms a LE separation bubble as low as 12° while the rigid wing does not form a LE bubble until an AOA of 18° . The bubble at the LE of the PR wing was much thicker, longer, and well defined. The PR wing's bubble also seemed to attach rapidly and always before the latex portion of the wing. At an AOA of 20° , however, both bubbles appeared to be of similar size and shape. Images of the outboard LE flow visualization are shown in Figure 4-36

Pulsed Laser Visualization

It was of interest to study the velocity profiles of the flow around all the types of wings. Many methods exist to determine velocity, but UF's MAE department owns a 2D particle image velocimetry (PIV) system which could gather 2D velocity fields across an image's field of view instantaneously. The experimental setup for PIV is essentially the same as that used for span wise visualizations (Figure 4-35). The PIV system uses a dual head pulsed Nd-YAg 50 mJ laser to create a laser sheet. The laser sheet is emitted in two bursts with a precision time interval, and a special digital camera captures an image from each laser sheet. The images captured are flow visualizations of a frozen particle field, and qualitative information may be gathered from the images. The purpose of the PIV system, however, is to obtain quantitative velocimetry data of the flow shown on the

images. The data may be processed to create streamlines and determine separation but is prone to error, especially when used in a 3D flow situation [23].

Particle image velocimetry

The PIV system operates by taking two consecutive photographs of an illuminated flow field and then cross-correlating the photos to create a 2D velocity vector field. PIV enjoys many benefits over other flow diagnostic methods, while at the same time it suffers from many disadvantages. PIV is nonintrusive, but the process only senses the velocity of seed particles in the flow which may not follow the actual path of the fluid. PIV requires a simple set up of a special PIV camera, a laser system capable of discharging two consecutive bursts, and a synchronizer system. PIV is a field technique which instantly captures the 2D velocities in the field of view of the camera. The time resolution of PIV, however, is poor compared to other methods due to technical limitations [24, 25].

The University of Florida's Mechanical and Aerospace engineering department owns a 2D PIV system developed by TSI Inc. The TSI system includes a dual head 50 mJ ND-YAg laser, a 1600x1200 pixel grayscale PIV camera, and a synchronizer unit which synchronizes the camera exposures to the laser pulses. Both the synchronizer and the camera are connected to a dual processor Pentium Xeon 2 Ghz system with 4 Gb of RAM. The PC runs *Insight*, the software required to access the synchronizer and camera and perform the vector validation. All parameters necessary for velocimetry are input to *Insight* and are passed on to the hardware.

Velocity fields of flow over MAV wings were gathered at various span wise locations with the laser sheet oriented parallel to the incoming flow and the gravity vector. A rigid and PR wing were tested at multiple angles of attack at several flight

speeds. At each speed and angle of attack the velocity field was found first over the suction side of the wing and then the model was rotated roll wise 180 deg and then pitched into the same AOA and the velocity field was found for the pressure side of the wing. At a speed of 10 m/s it was determined that smoke from the LeMaitre Neutron XS would provide sufficient seeding. The uniform size and homogenous dispersion of the haze made its use a perfect choice for MAV velocimetry [23, 25, 26].

The laser heads were set up on a span wise traverse attached to an optical table on top of the test section. A mirror was used to aim the laser sheet through the ceiling window down through the test section. The lasers could be traversed so that the sheet could cross the span of the wing with much accuracy. The camera was oriented normal to the laser sheet plane outside the test section and was positioned so as to optimize seed visibility while at the same time keeping the entire profile of the wing in the frame. The computer and synchronizer were placed so that the operator could avoid looking at the bright laser light, and also so the light from the computer screen could not be intercepted by the PIV camera.

Each experiment captured 500 image pairs with a time differential of 15 μ s. The region of interrogation was sized at 32x32 pixels based off of the seeding capabilities of the haze machine [23, 24, 26]. After the PIV images were captured the vectors were calculated in *Insight* and the resulting vector fields were ensemble averaged to create a mean vector field. Before calculating a mean field, erroneous vectors were excised using reasonable minimum and maximum velocity constraints [23]. The mean vector fields of the suction and pressure side of the wing were combined in Matlab and the velocity vector data were used to calculate a field of velocity magnitude, velocity ratio (V_r), and

vorticity. Of most interest were plots of V_r which showed information similar to the Euler pressure coefficient (C_p). The V_r plots showed normalized pressure distributions in the inviscid regions, ignoring 3D effects, but are less useful in regions of separation and the boundary layer. Poor vector calculations were present around overexposed areas of the wings leading to the inability to resolve boundary layer information. White tape was placed on the test section glass to reduce reflections, but this also obscured boundary layer image information. The inability to accurately traverse the camera during the experiment also restricted the capability of zooming the camera in to yield more detailed observations. Manual methods of traversing the camera were attempted, but accurate correlations could not be made between frames.

Figure 4-37 shows the velocity ratio contours for the wings placed in the wind tunnel at an AOA of 15° and a wind tunnel velocity of 10 m/s. The PIV images were gathered 40 mm out from the center span location, hence they complement the comparison span wise flow visualization experiment. This flight condition was chosen because loads data showed that the PR wing operated more efficiently than the rigid wing [7]. The V_r plots prepared showed the difference between the wings. V_r was calculated using the equation in Equation 4-1, which is a simplified formulation of the Euler pressure coefficient.

$$V_r = 1 - \left(\frac{\text{Velocity Magnitude}}{\text{Origin Velocity}} \right)^2 \quad (4-1)$$

The PR wing V_r plot shows that the low pressure region on the top of the wing extends over a longer region of the wing and has an overall lower pressure. The difference in the low pressure region alone can account for the enhanced lifting properties of the PR wing. Furthermore, it seems that the high pressure region on the pressure side

of the PR wing extends further aft than it does on the rigid wing. Loads tests on the wings showed that the wings have different pitching moment properties, and this can be visualized by the pressure distributions [3].

As would be expected the flow fields over the centerline of the wings were very nearly identical because the wing is very rigid in that area and the deflection due to air loading was very small. Third dimensional flow effects and related errors, if present, should be quite small along the centerline because it is an axis of flow symmetry [23]. Poor velocity correlations were obtained around the span wise location of the wing tips. It was also difficult to reference distances when the sheet was placed beyond the wing tip because no area of the wing was in focus. This poor correlation is most likely due to the large out of plane component of air velocity due to the strong wing tip vortices [23, 25]. The highest quality outboard PIV correlations were obtained 40 mm away from the center span of the wing

Streamlines were calculated in Matlab based off of mean velocimetry data and superimposed over images of the seeded flow field to show the flow characteristics (Figure 4-38). A difference in the streamline plots between the PR rigid wing was noted which may affect lift. On the pressure side of the aft portion of the BR and rigid wings the streamlines came closer together indicating a flow acceleration. This flow acceleration is likely due to the pronounced reflex in that area of the rigid wing. However, the PR wing does not have so strong of an acceleration effect due to the lessened effect of reflex. This makes sense as the PR wing has no physical supports which enforce the trailing edge shape. This effect is important because it affects the pitching moment of the PR wing and perhaps increases its lift over the rigid wing. The

streamlines that end in space are artifacts of the PIV system's inability to closely resolve the boundary velocities along the wing.

PIV can add valuable insight to the pressure distribution and the flow field for many applications. It is possible to obtain high resolution and high accuracy velocity field data for a number of applications, however it was noted that the standard deviations of the data were very high indicating errors in velocity determination. The contours of Figure 4-23 were only calculated using the two components of velocity in the plane of the laser. Any contribution due to the third velocity component was lost from the data, hence the contours may only be viewed as indicators of the pressure field distributions and not actual distributions [22]. Better information could be gathered using a 3D PIV system and a traverse system which would allow for precise camera placement.

Pulsed laser visualization

Before the continuous laser flow visualization experiments were performed, visualization was attempted using the PIV system. The rigid and PR wing models were placed in a different open loop wind tunnel for which seed had to be injected at the inlet. The seeding was very inhomogeneous and led to poor PIV correlations, however the flow visualizations obtained showed peculiar behavior. Figure 4-39 shows a rigid and PR wing at an AOA of 12° and velocity of 10 m/s. The LE separation bubble of the PR wing was evident in these pictures as was the long separation bubble off the camber position of the rigid wing. These pictures showed the instantaneous flow structure of the flow over the wing.

Conclusions

The rigid, BR, and PR wings were subjected to laser sheet flow visualizations which elucidated their flow properties. The rigid wing was shown to exist with a laminar

long separation bubble emanating from a position of high camber at low AOA. As AOA was increased it was seen that a short laminar separation bubble forms off the LE and its reattachment creates turbulence which keeps the flow attached until stall. Stall progressed through two stages. The first stage of stall is characterized by detachment of the turbulated boundary layer on the aft portion of the wing as the short bubble remains intact. The second stage of stall is a burst LE bubble with no attached flow.

Significant obstacles exist to using laser flow visualizations on flexible wings which use a latex membrane on the flexible portions. Nevertheless, methods were found to obtain data using these methods. The PR wing had a LE separation bubble which formed at lower AOA than the rigid wing, and this bubble was thicker and longer than any bubble which formed off the rigid wing's LE. Accordingly, the turbulence shed by the PR wing's bubble was of a different nature. 2D PIV applied to UF MAV wings may be used to determine general pressure distributions, but the effects of 3D flow causes this method to yield erroneous results. A 3D PIV system would be most useful in determining MAV velocimetry information.

Table 4-1: Reasoning behind selection of AOAs of interest

AOA	Reason for interest
0°	Zero lift yet has high drag
5°	Minimum drag case
10°	Strong vibration begins here
16°	Decrease in drag, decrease in moment
18.4°	Before drag divergence
18.9°	After drag divergence
21°	Before stall
22°	Maximum lift coefficient
23°	Stalled wing
25°	Fully stalled wing on secondary lift curve
30°	Fully stalled wing on tertiary lift curve

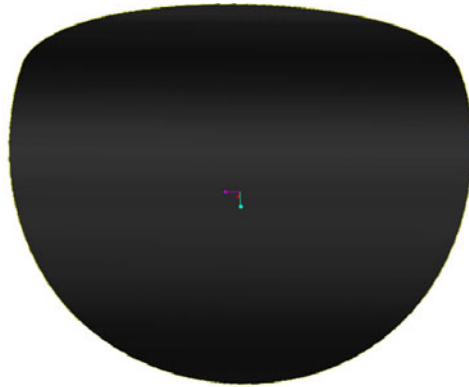


Figure 4-1. ProEngineer rendering of model having LAR Zimmerman planform.

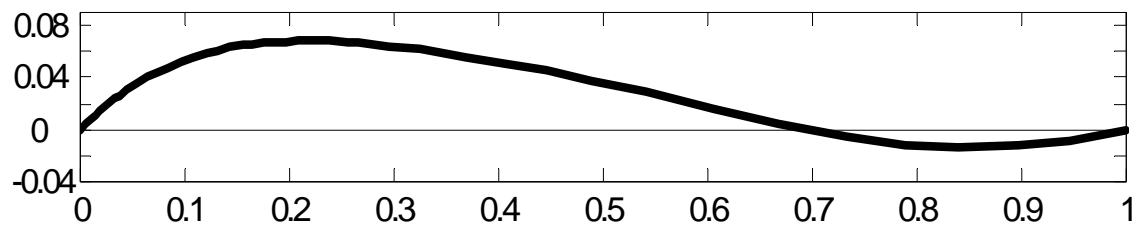


Figure 4-2. Plot of normalized airfoil used on 2004 competition MAVs.

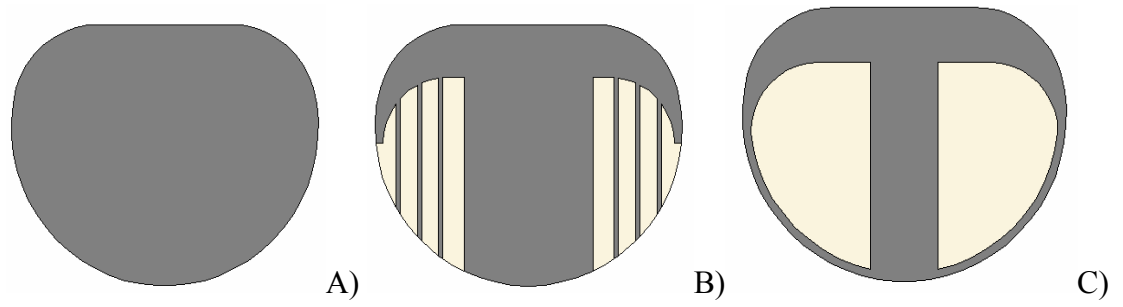


Figure 4-3. Planform of rigid wing (A), BR wing (B), and PR wing (C).



Figure 4-4. MAV rigid wing model with sting mount attached and edges sanded.

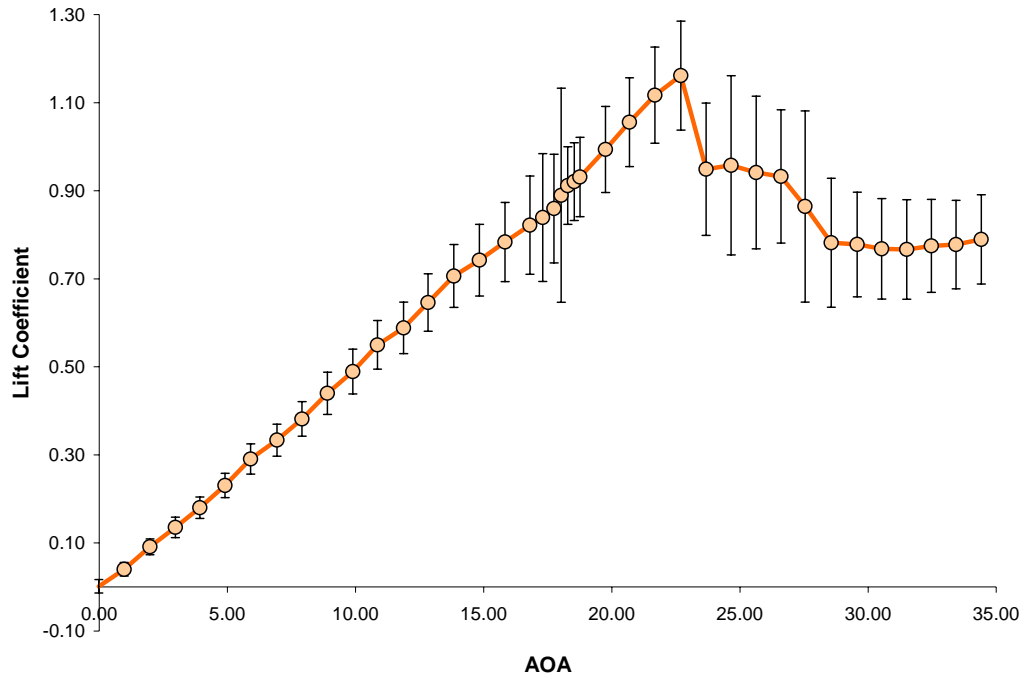


Figure 4-5. Variation of lift coefficient over AOA at origin velocity of 10 m/s.

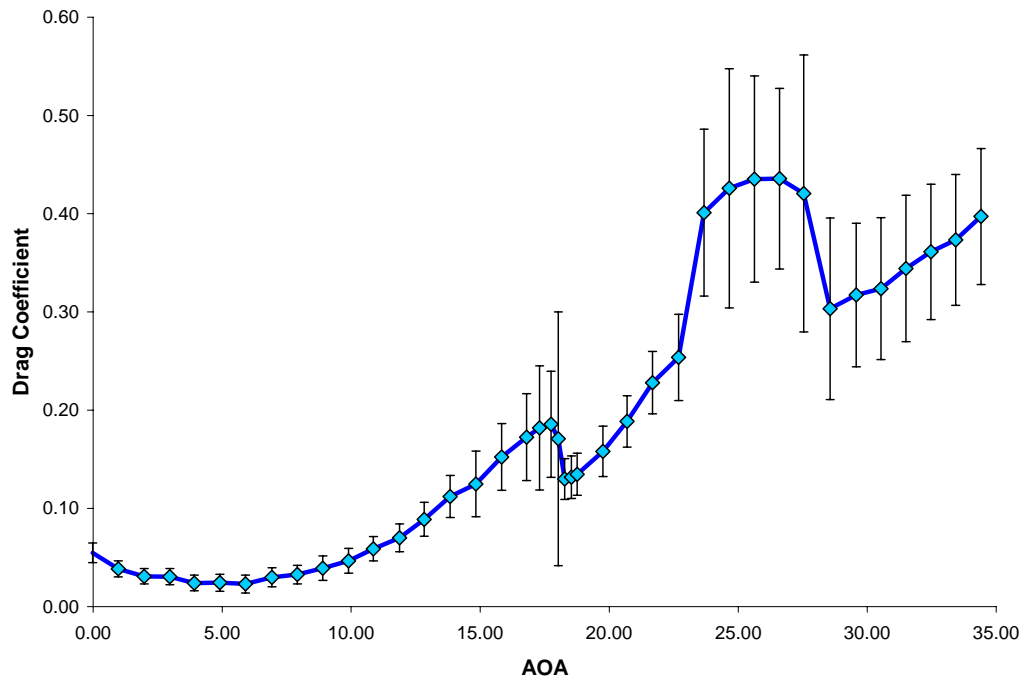


Figure 4-6. Variation of drag coefficient over AOA at origin velocity of 10 m/s.

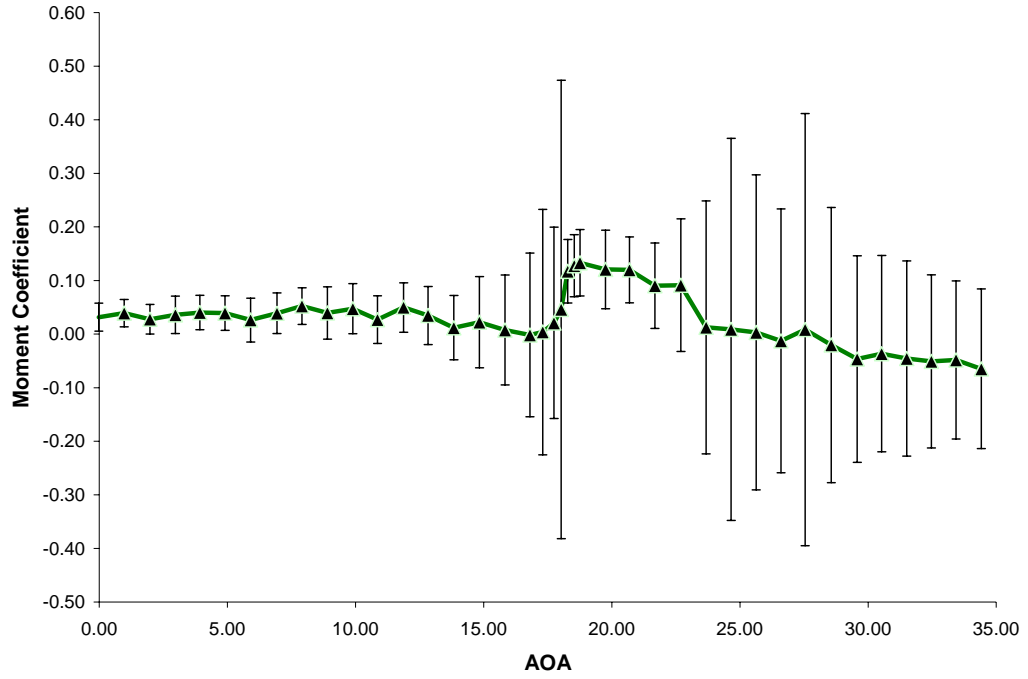


Figure 4-7. Variation of moment coefficient over AOA at origin velocity of 10 m/s.

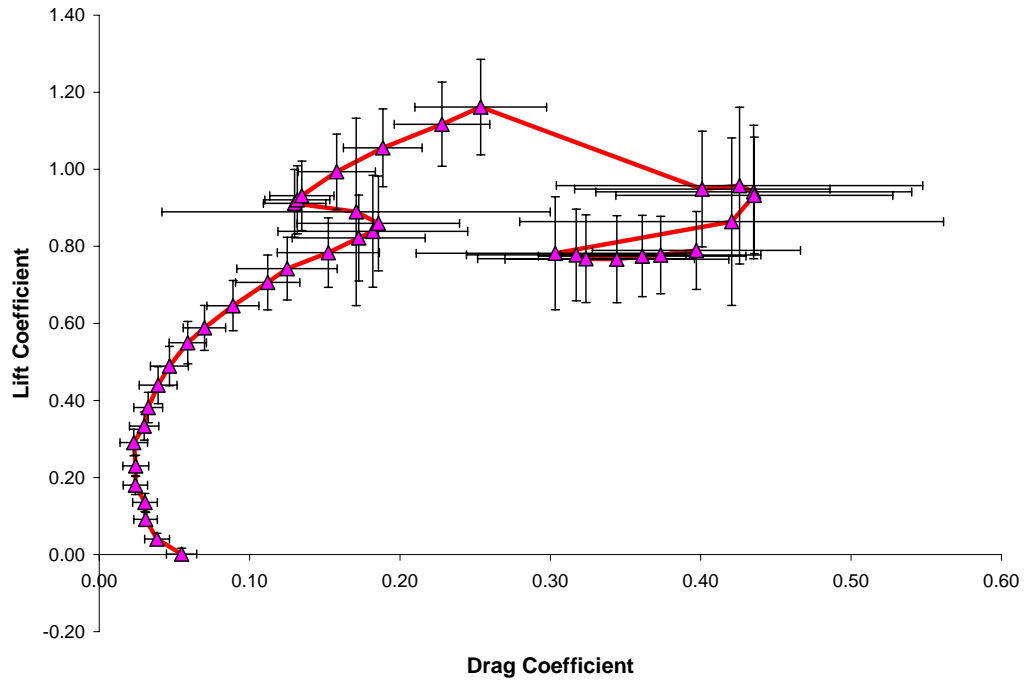


Figure 4-8. Lift vs. drag coefficient at origin velocity of 10 m/s.

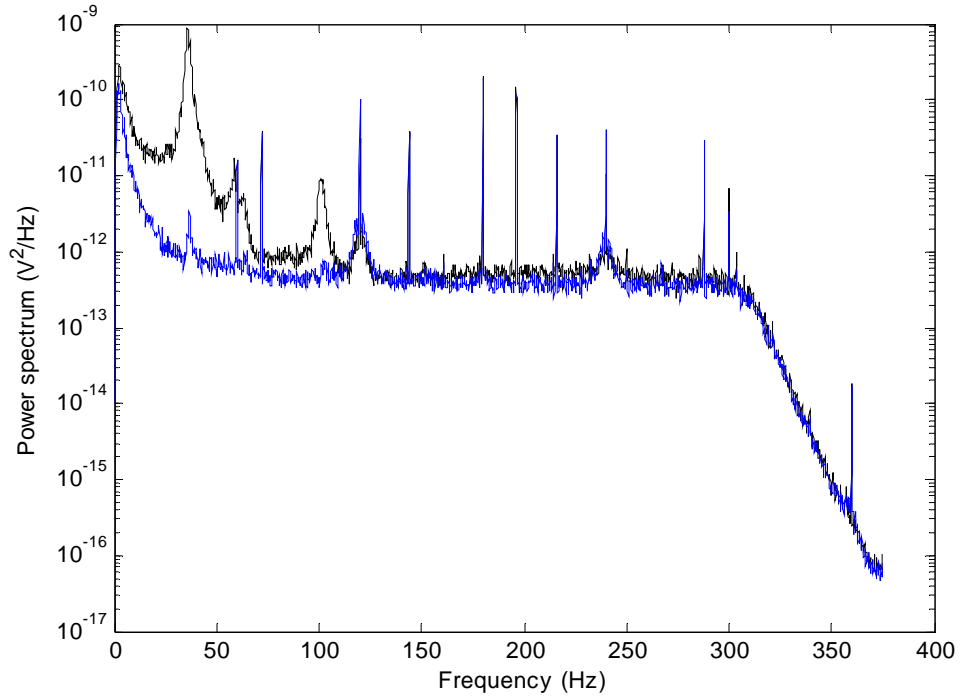


Figure 4-9. Power spectral density plot of strain gage signal (black) and baseline signal (blue) at an AOA of 18° and wind tunnel velocity of 10 m/s.

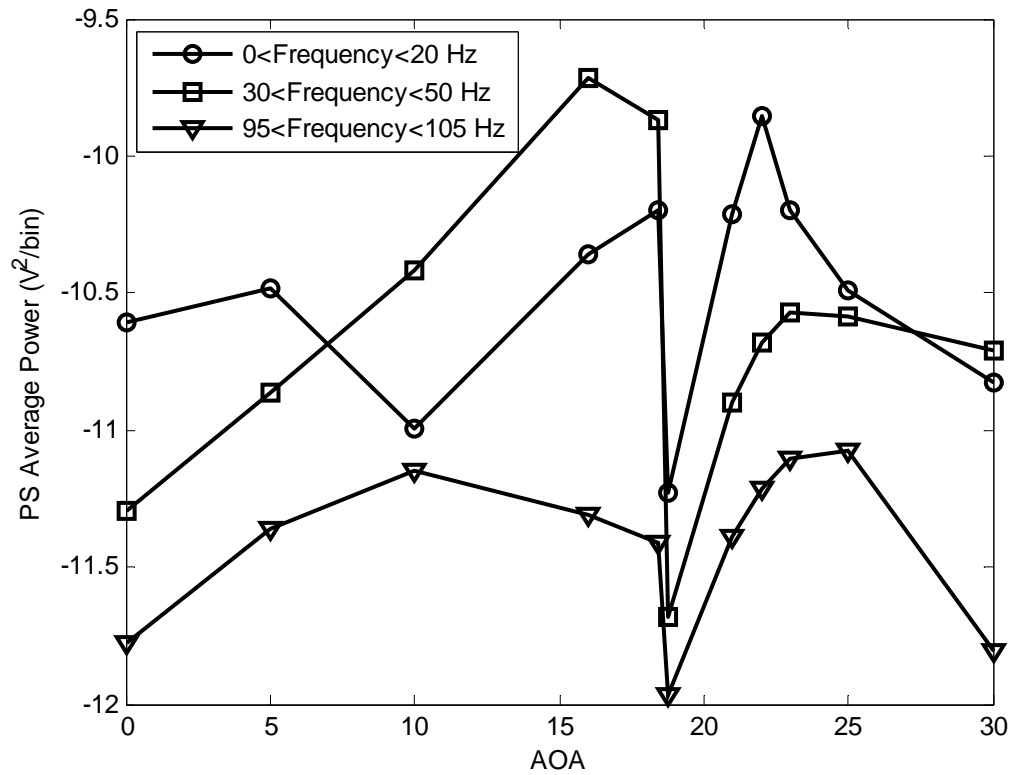


Figure 4-10. Average power of predominant modes at $V = 10$ m/s.



Figure 4-11. Oil surface flow visualization of wing at AOA of 0° and wind tunnel velocity of 10 m/s

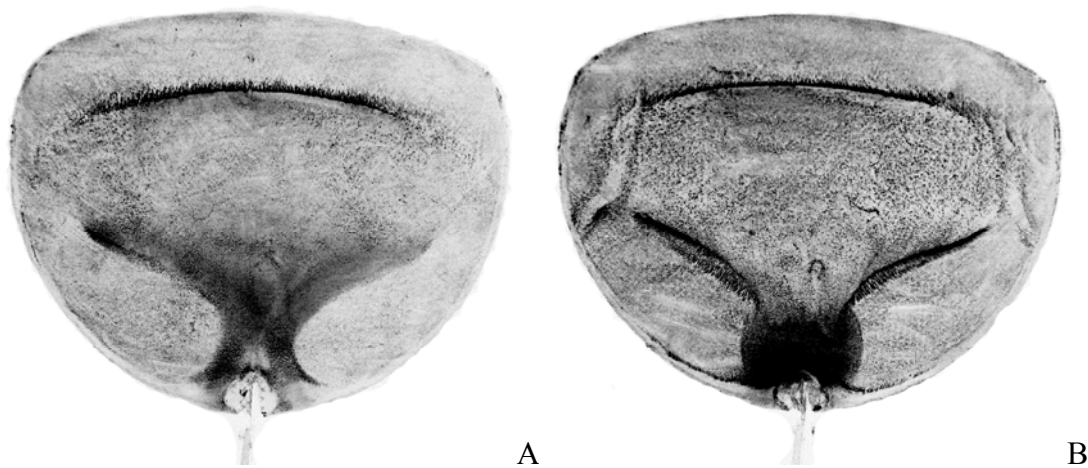


Figure 4-12. Oil surface flow visualization of wing at A) AOA of 5° and B) AOA of 10° and wind tunnel velocity of 10 m/s

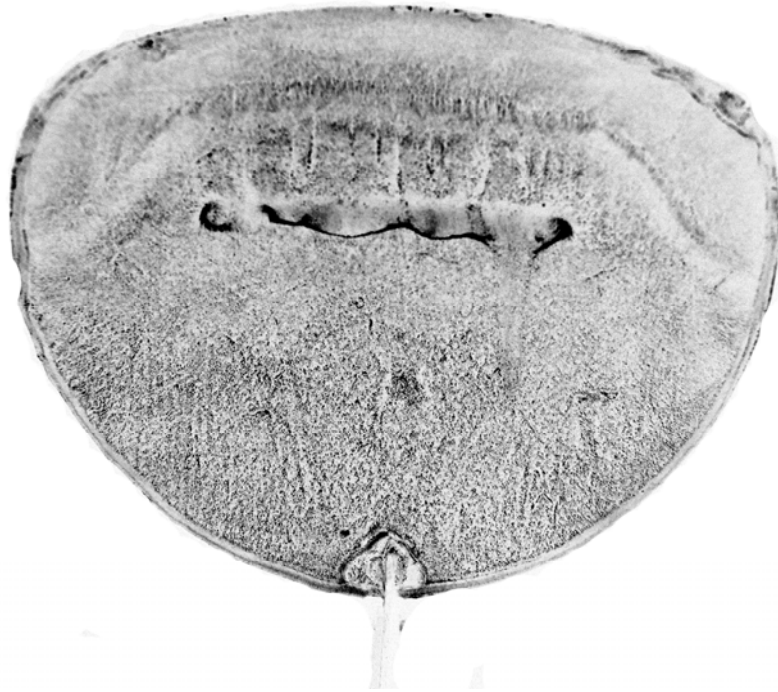


Figure 4-13. Oil surface flow visualization of wing at AOA of 16° and wind tunnel velocity of 10 m/s

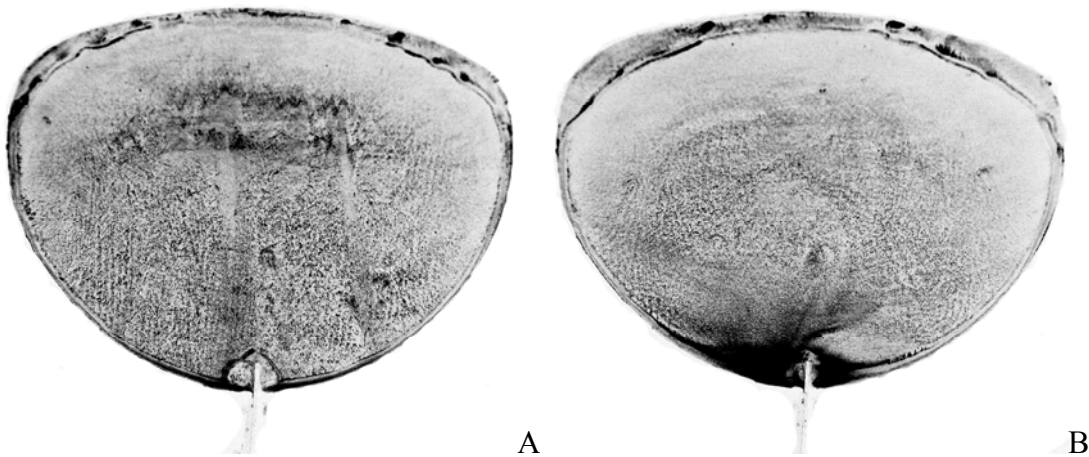


Figure 4-14. Oil surface flow visualization of wing at A) AOA of 18.4° and B) AOA of 21° and wind tunnel velocity of 10 m/s.



Figure 4-15. Oil surface flow visualization of wing at A) AOA of 23° and B) AOA of 30° and wind tunnel velocity of 10 m/s

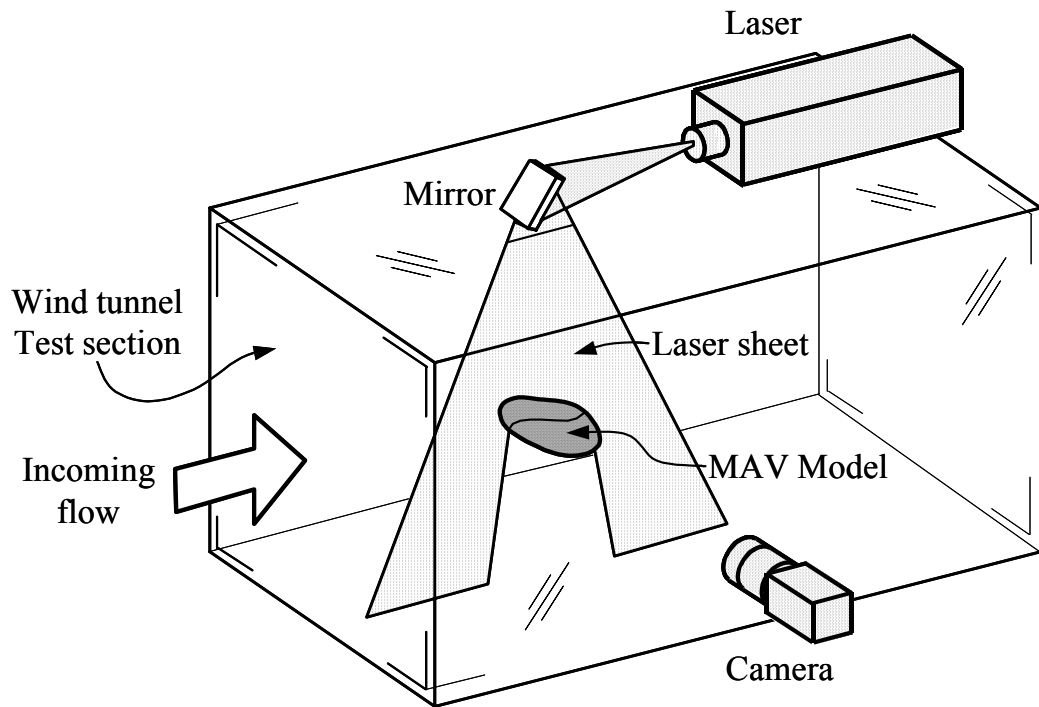


Figure 4-16. Diagram of span wise laser flow visualization setup.

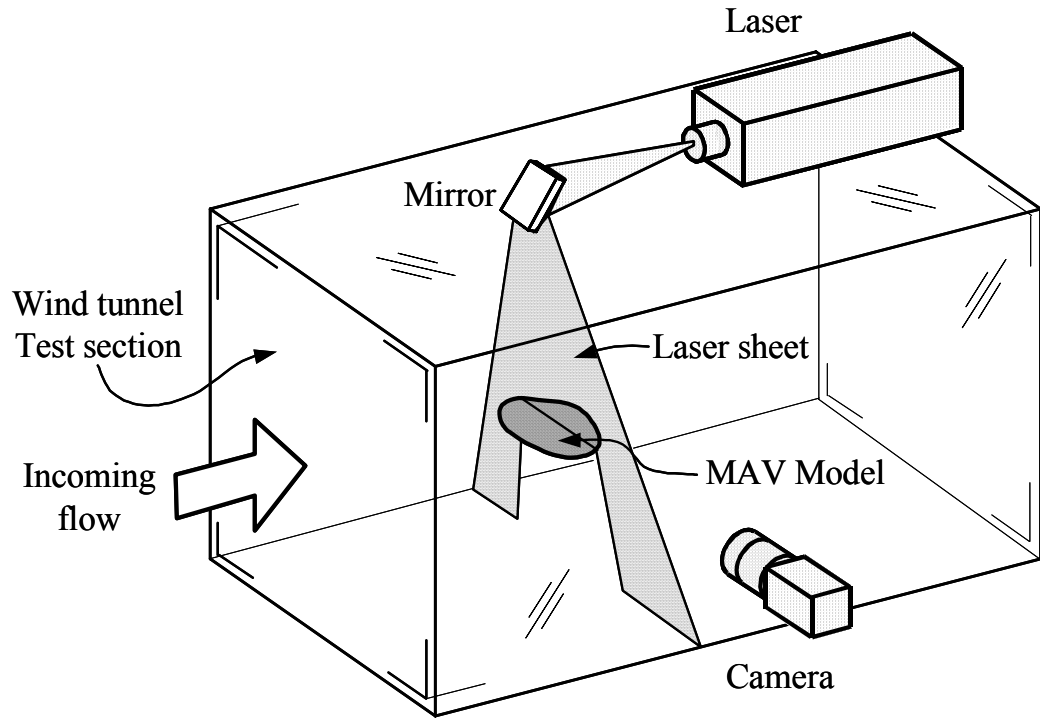


Figure 4-17. Diagram of chord wise laser flow visualization setup.

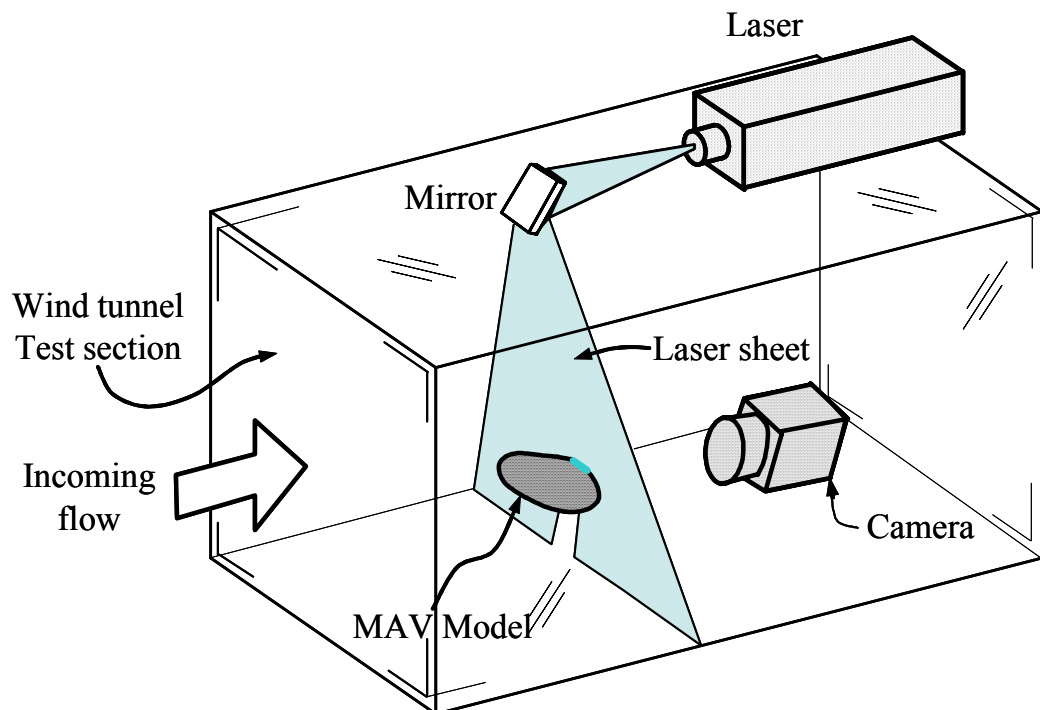


Figure 4-18. Diagram of chord wise visualization with laser sheet directed at very TE of wing.

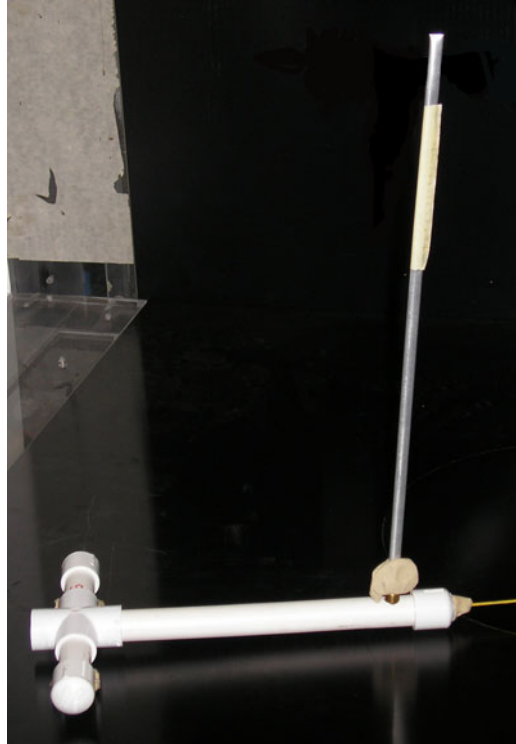


Figure 4-19. Line seeder apparatus inside large test section.

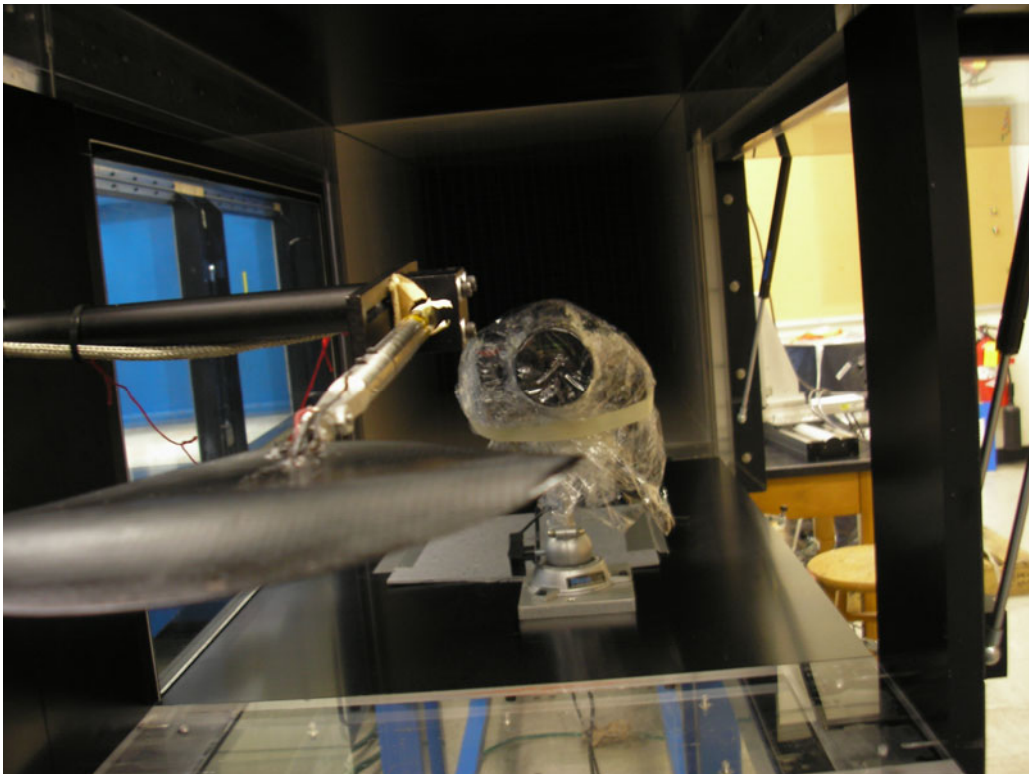


Figure 4-20. View of camera in small test section looking from perspective of seeder

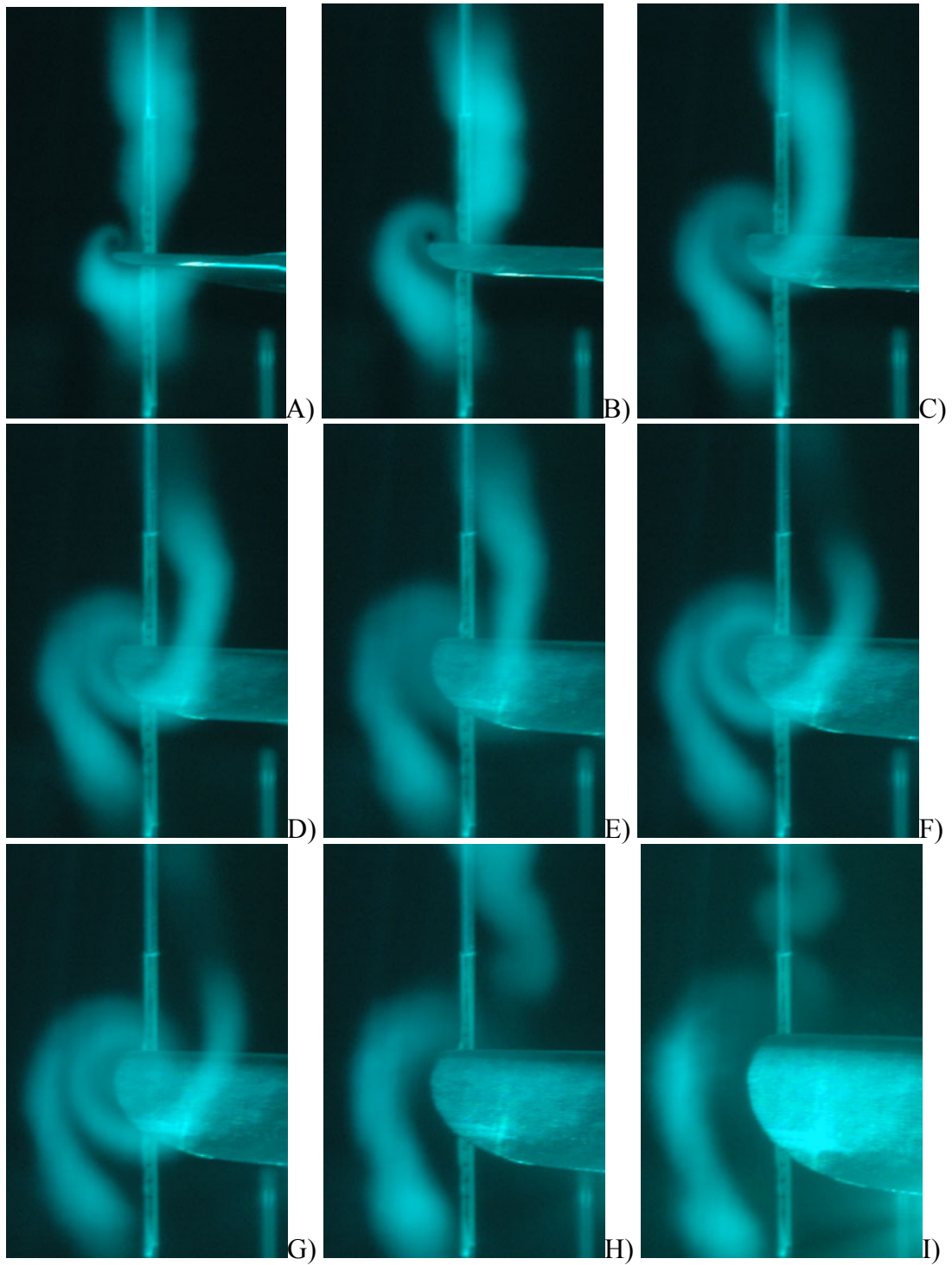


Figure 4-21. Images of vortex evolution for a rigid wing with a wind tunnel velocity of 10 m/s, AOA = 0° (A), 5° (B), 10° (C), 16° (D), 18.5° (E), 18.9° (F), 21° (G), 23° (H), 30° (I).

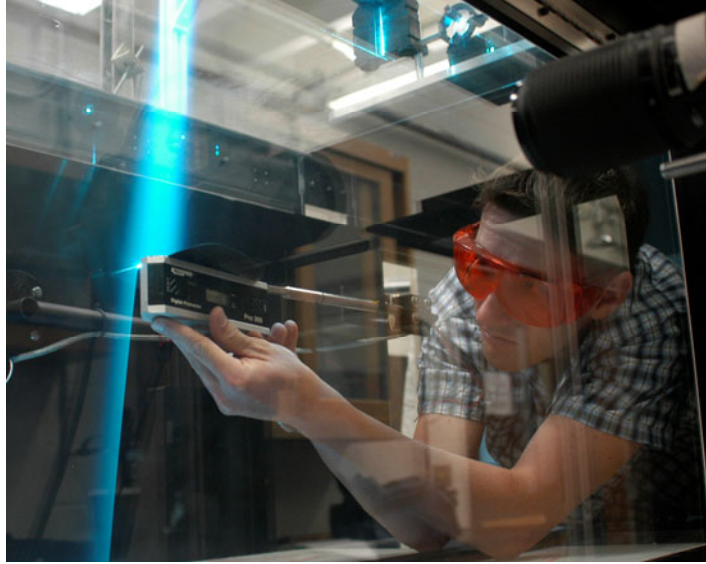


Figure 4-22. Gathering accurate AOA measurement before taking pictures. Camera is top right, and laser sheet is on minimum dispersion and full power. Photo courtesy Bob Bird.

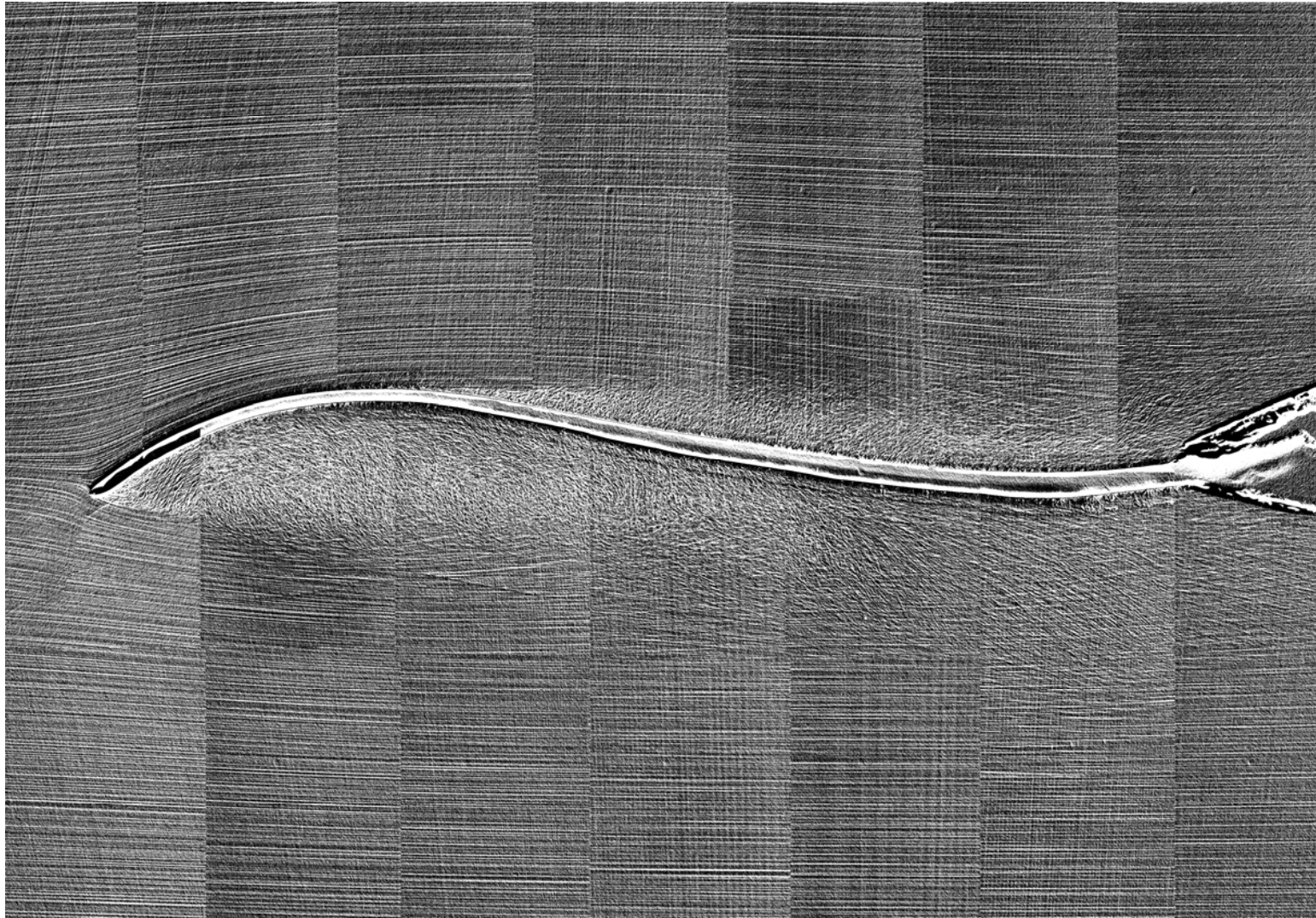


Figure 4-23. Flow visualization mosaic of center span of wing at a wind tunnel velocity of 10 m/s, AOA = 0°.

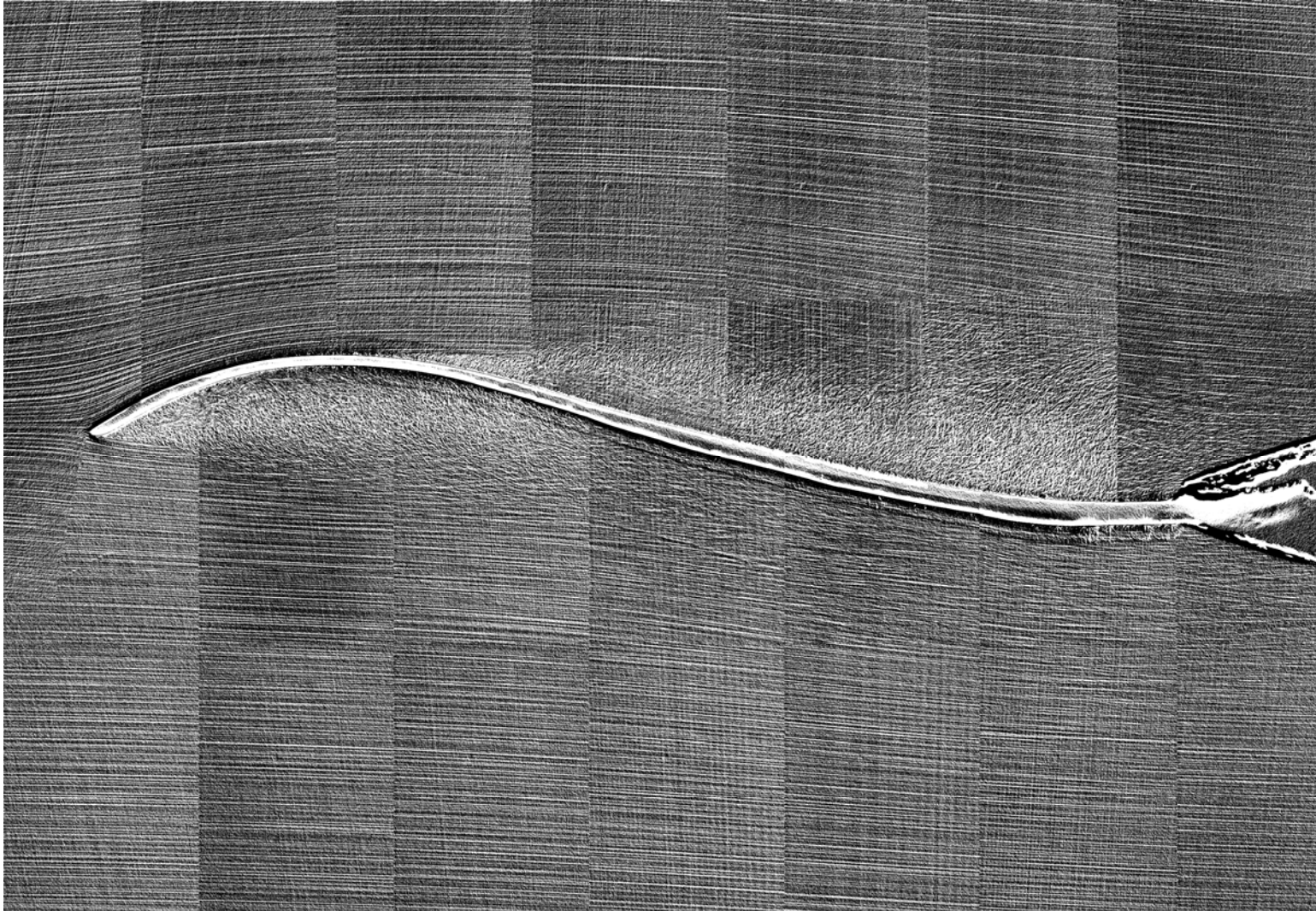


Figure 4-24. Flow visualization mosaic of center span of wing at a wind tunnel velocity of 10 m/s, AOA = 5°.



Figure 4-25. Flow visualization mosaic of center span of wing at a wind tunnel velocity of 10 m/s, AOA = 10°.



Figure 4-26. Flow visualization mosaic of center span of wing at a wind tunnel velocity of 10 m/s, AOA = 16°.

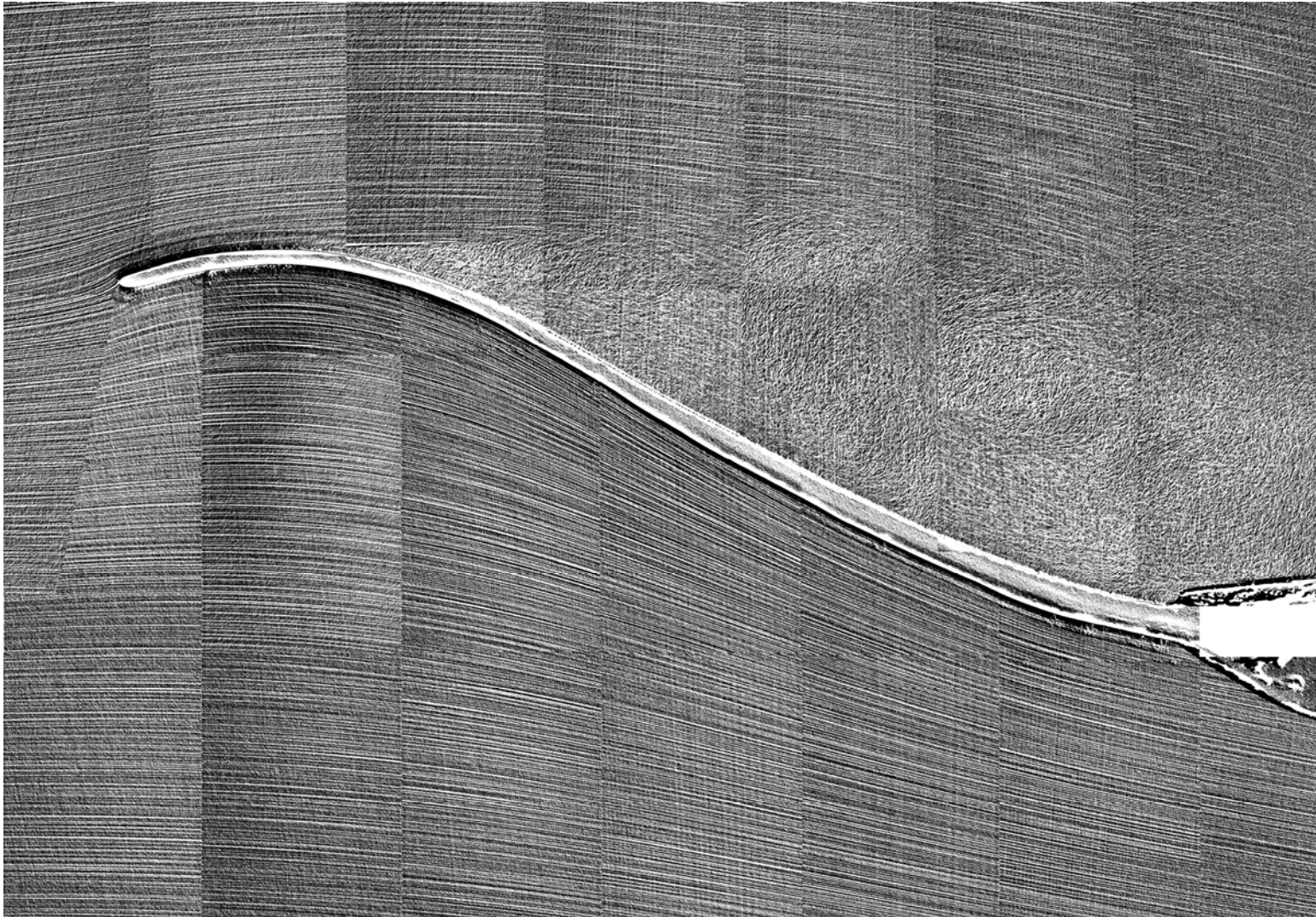


Figure 4-27. Flow visualization mosaic of center span of wing at a wind tunnel velocity of 10 m/s, AOA = 18.4°.



Figure 4-28. Flow visualization mosaic of center span of wing at a wind tunnel velocity of 10 m/s, AOA = 18.8°.

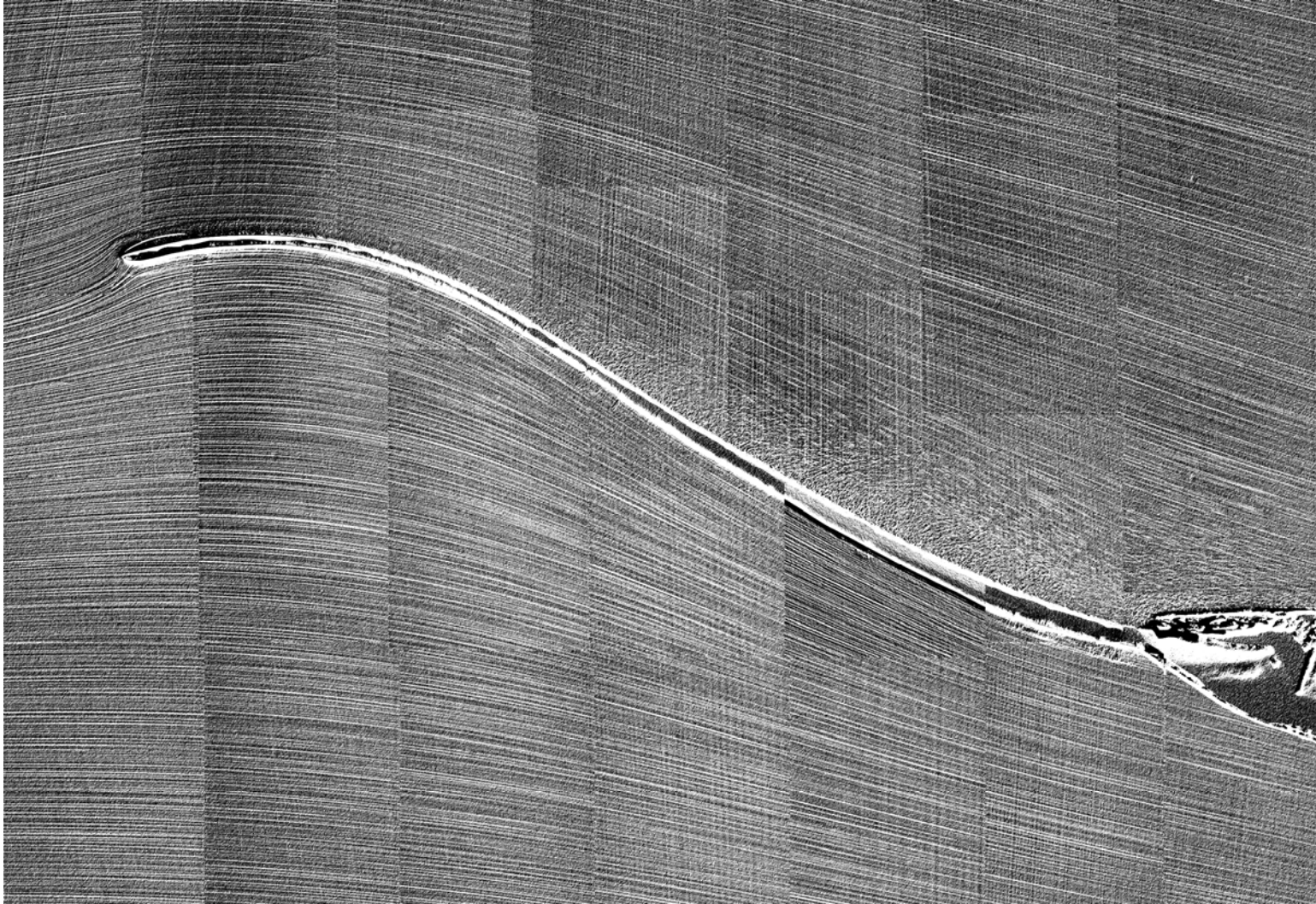


Figure 4-29. Flow visualization mosaic of center span of wing at a wind tunnel velocity of 10 m/s, AOA = 21°.

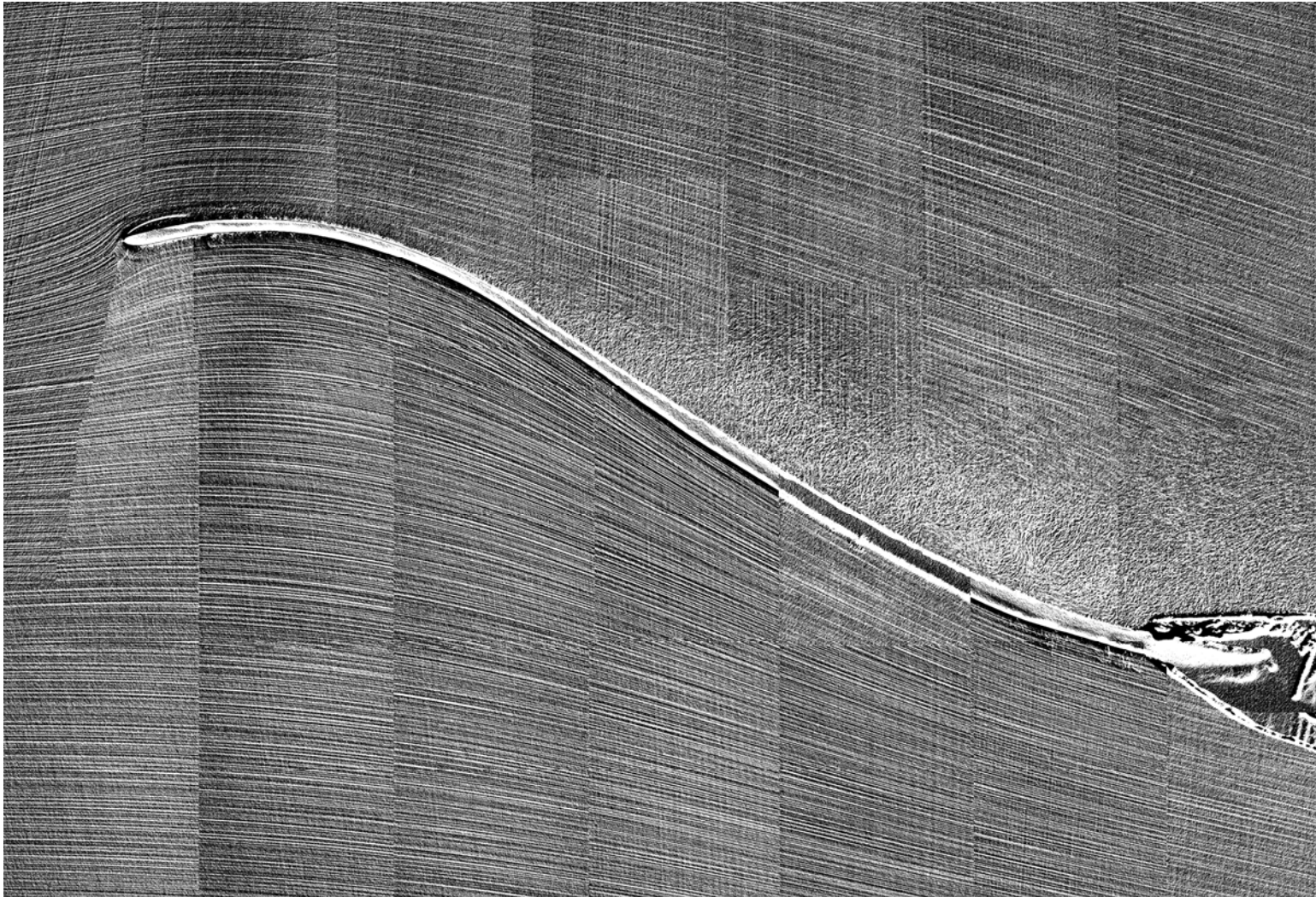


Figure 4-30. Flow visualization mosaic of center span of wing at a wind tunnel velocity of 10 m/s, AOA = 22°.

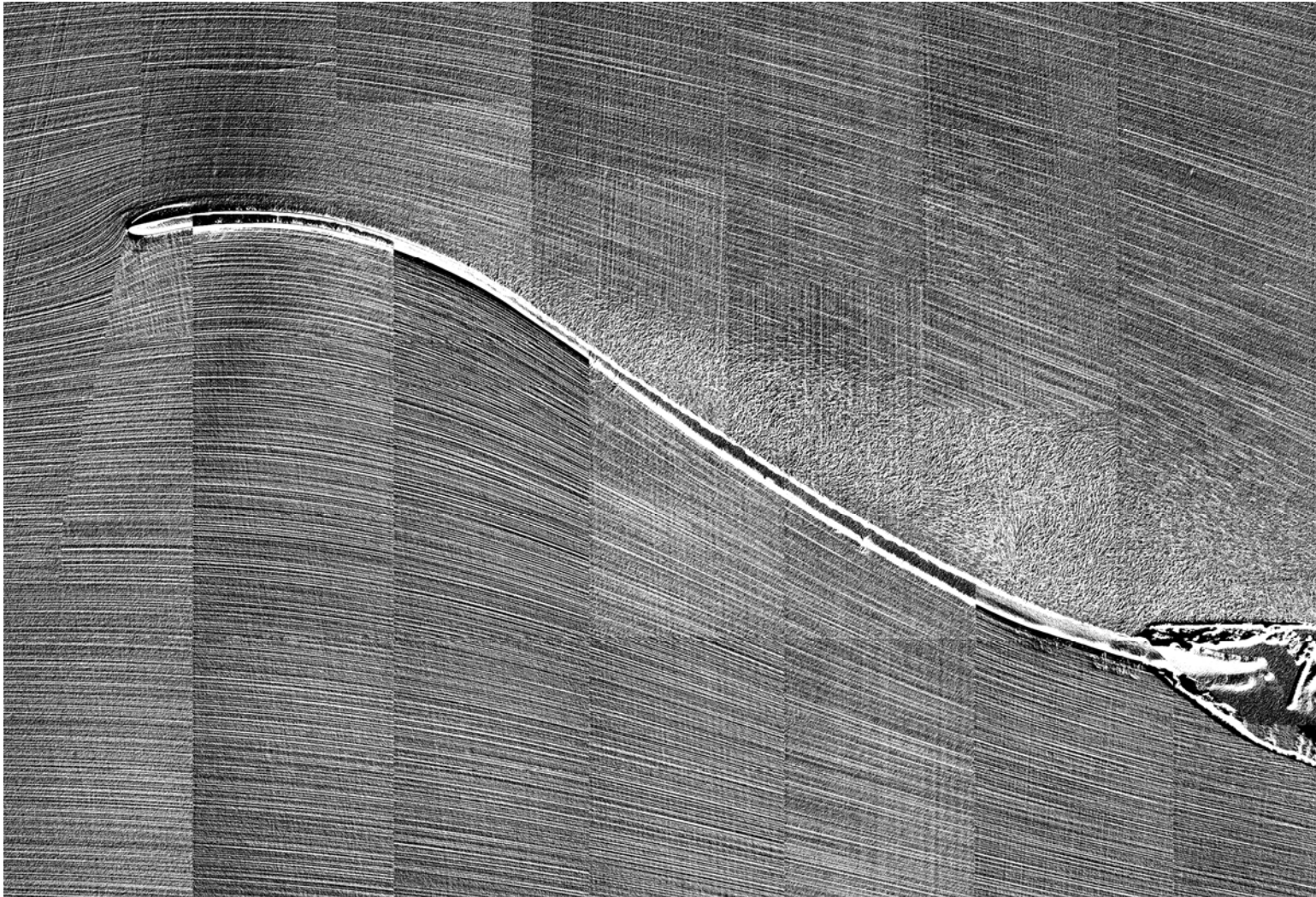


Figure 4-31. Flow visualization mosaic of center span of wing at a wind tunnel velocity of 10 m/s, AOA = 23°.



Figure 4-32. Flow visualization mosaic of center span of wing at a wind tunnel velocity of 10 m/s, AOA = 25°.

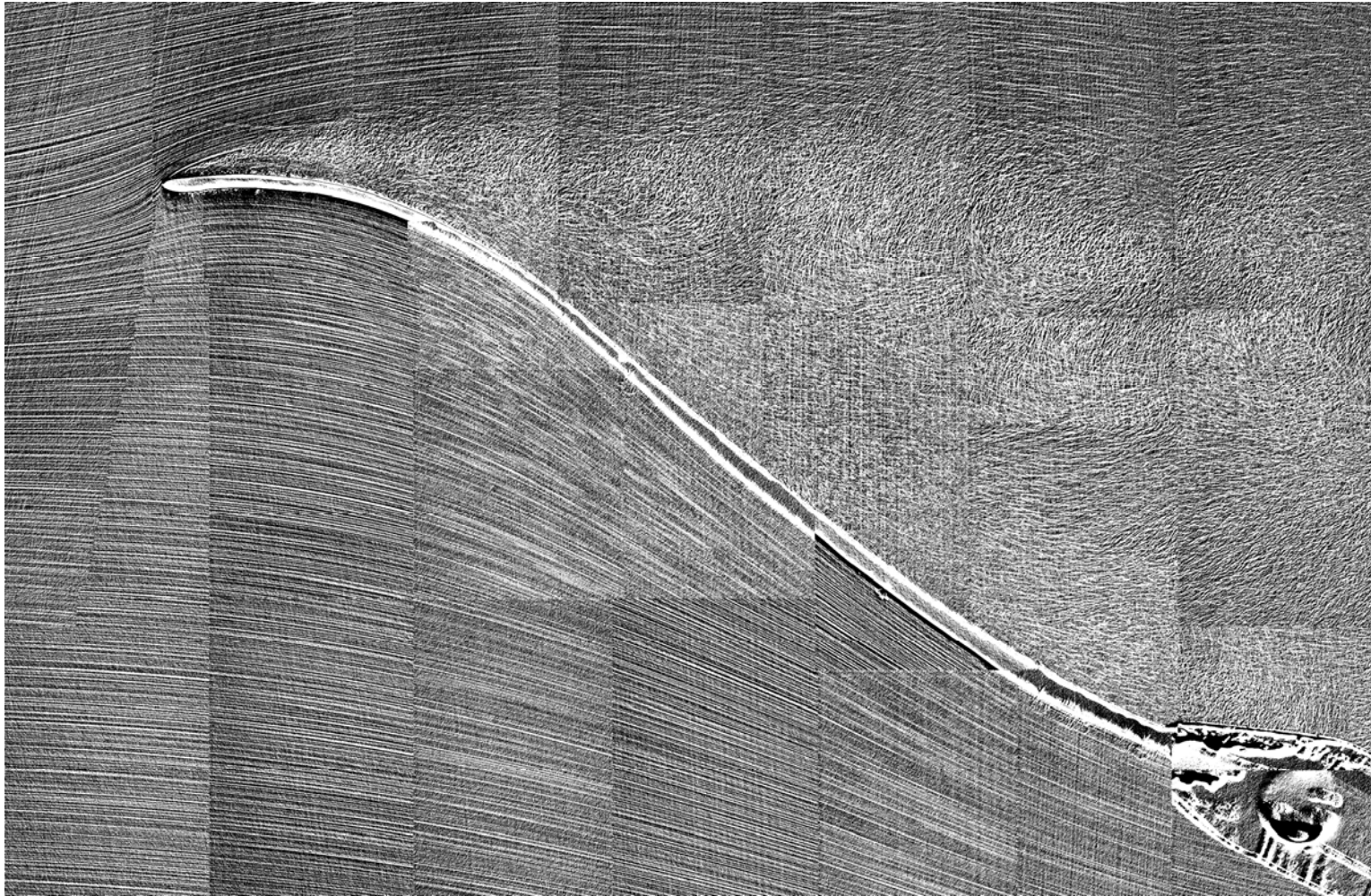


Figure 4-33. Flow visualization mosaic of center span of wing at a wind tunnel velocity of 10 m/s, AOA = 30°.

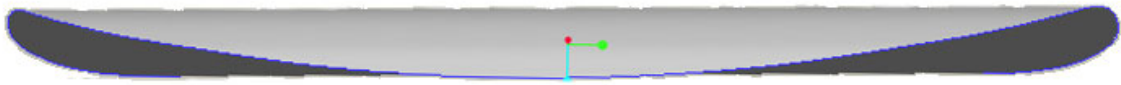


Figure 4-34. Image of LE of wing indicating decreasing downward slope of LE toward wing tips.

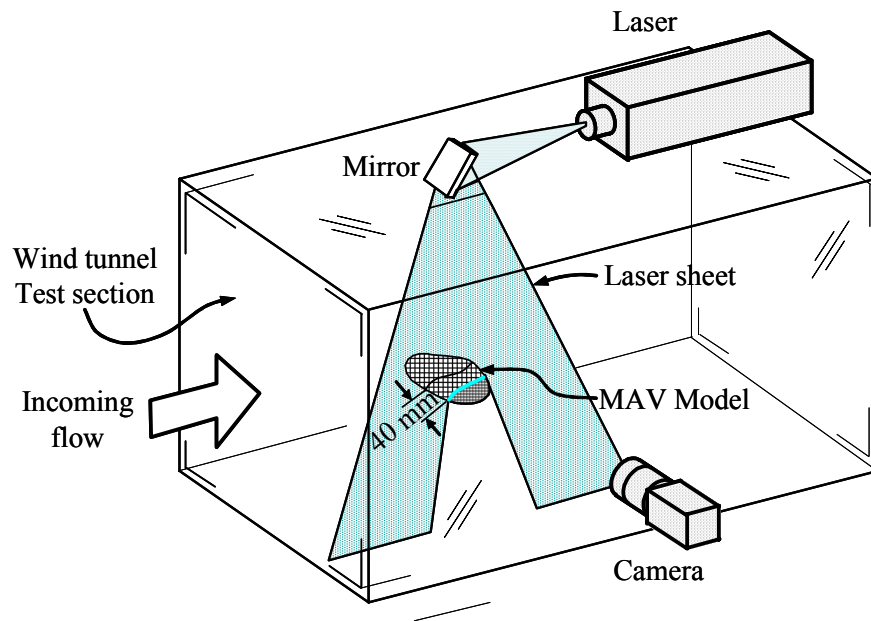


Figure 4-35. Diagram of laser sheet directed 40 mm from center span location.

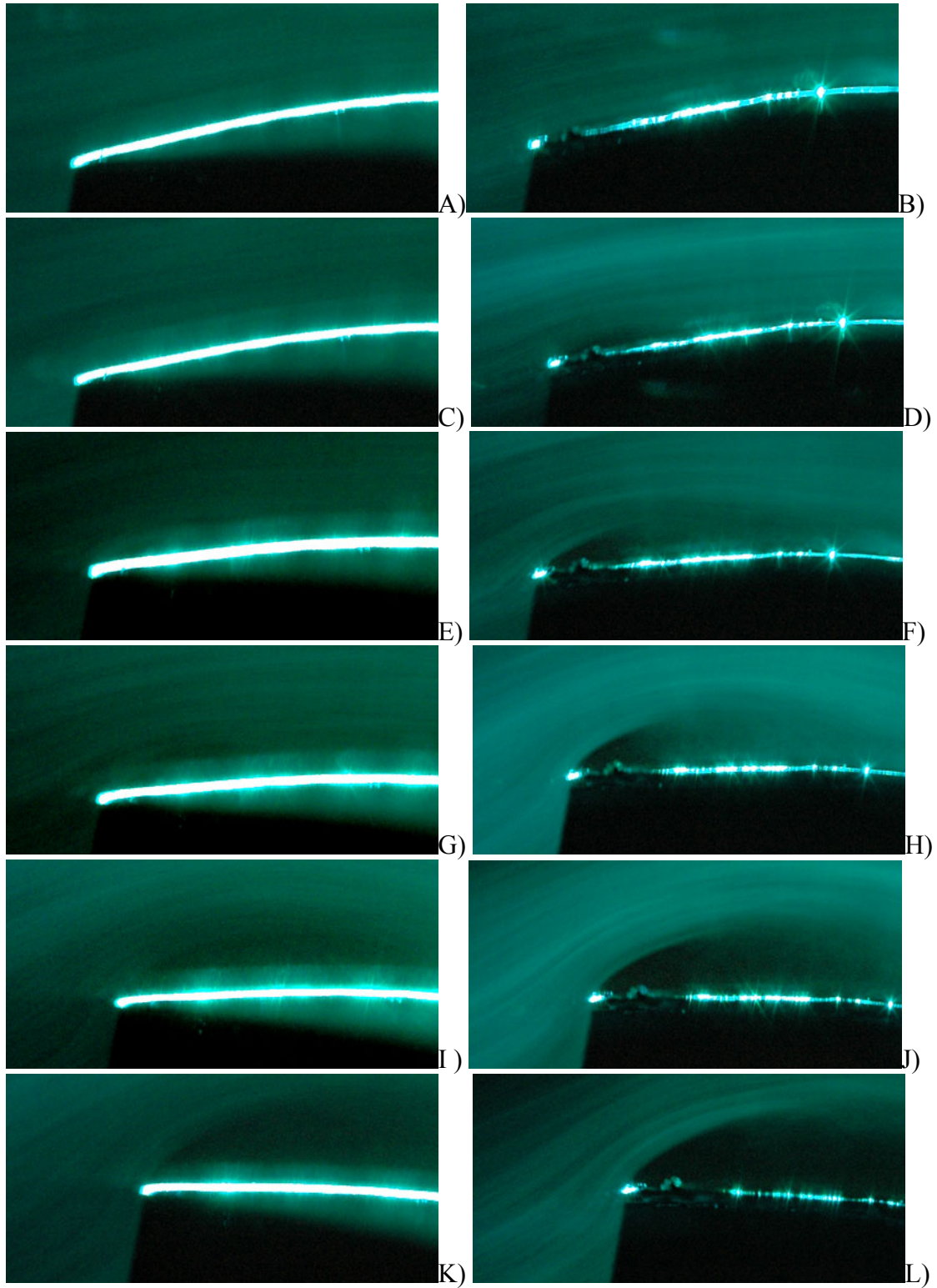


Figure 4-36. Leading edge visualizations of rigid wing (left column) and PR wing (right column) visualizations 40 mm out from center span at $V = 10$ m/s and AOA of 10° (A,B), 12° (C,D), 14° (E,F), 16° (G, H), 18° (I, J), 20° (K, L).

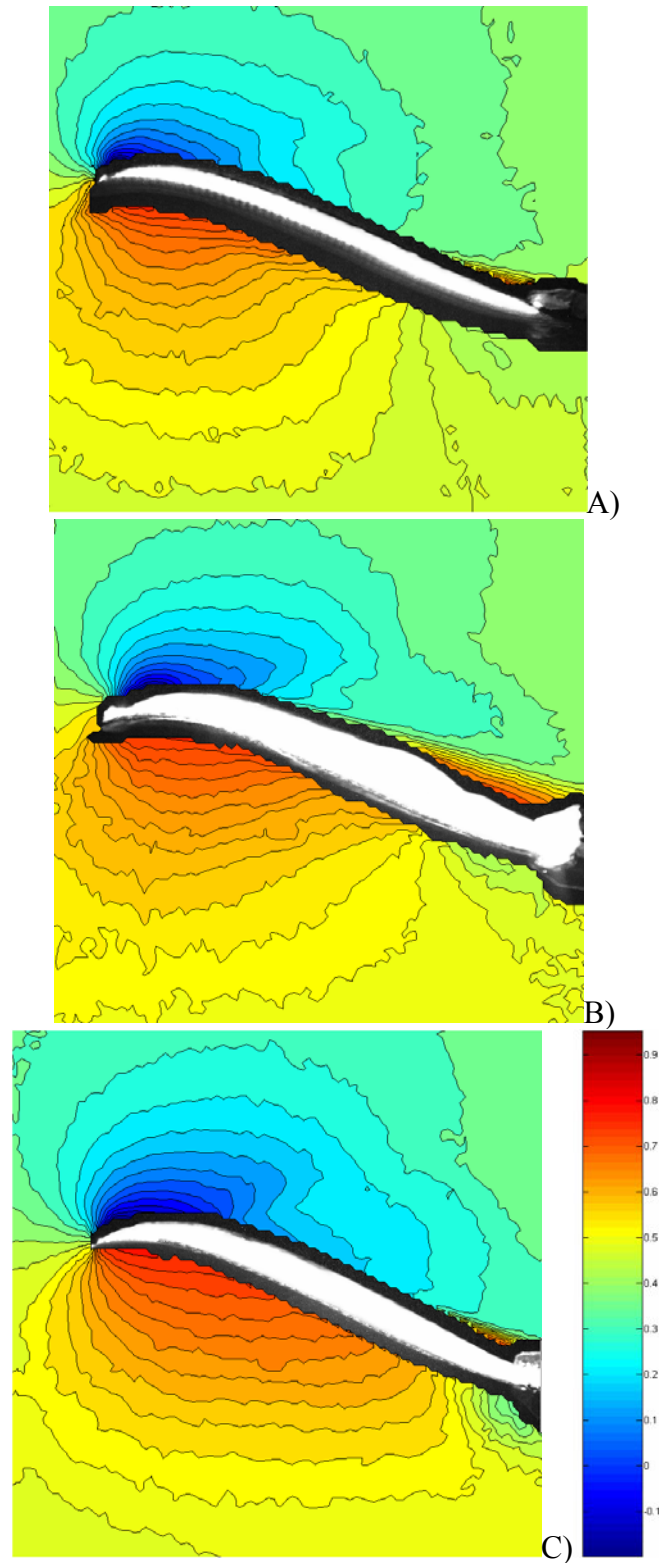


Figure 4-37. Velocity ratio contours for rigid (A), BR (B), and PR (C) wings at AOA of 15° and wind tunnel velocity of 10 m/s. Images obtained 40 mm from center span of wing.

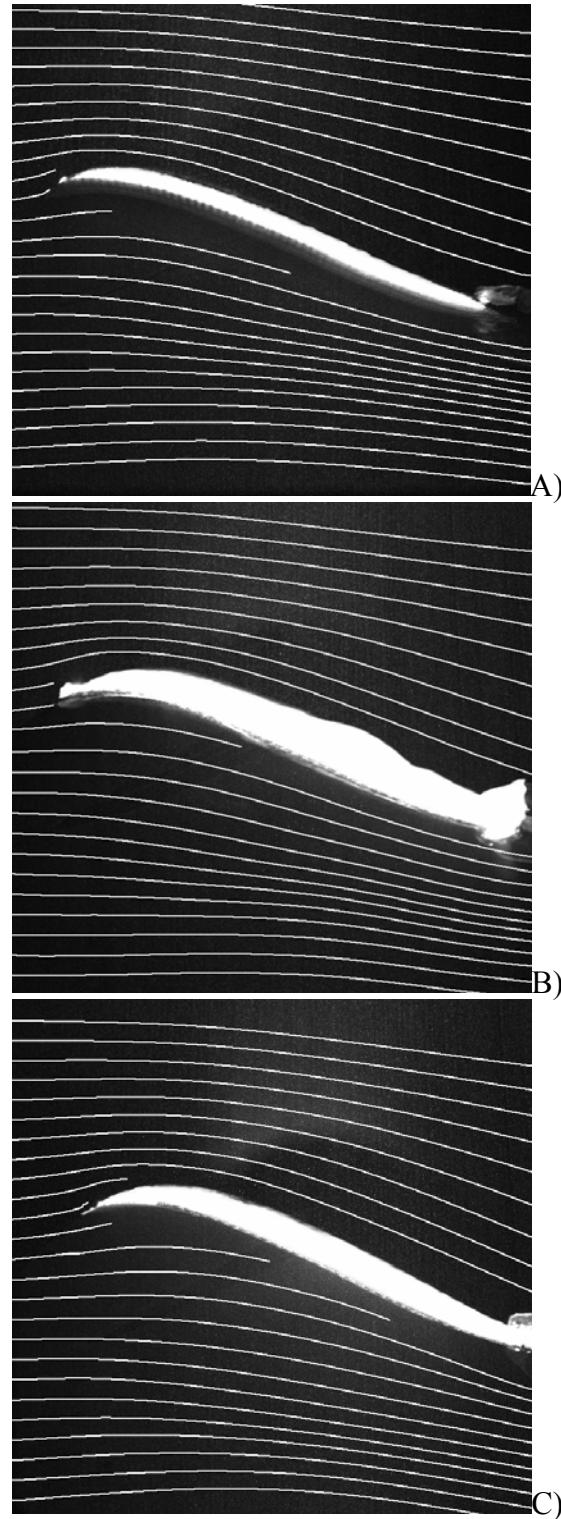


Figure 4-38. Streamlines generated in Matlab superimposed on top of images gathered using PIV camera. Images are rigid (A), BR (B), and PR (C) wings at AOA of 15° and wind tunnel velocity of 10 m/s. Images obtained 40 mm from center span of wing.

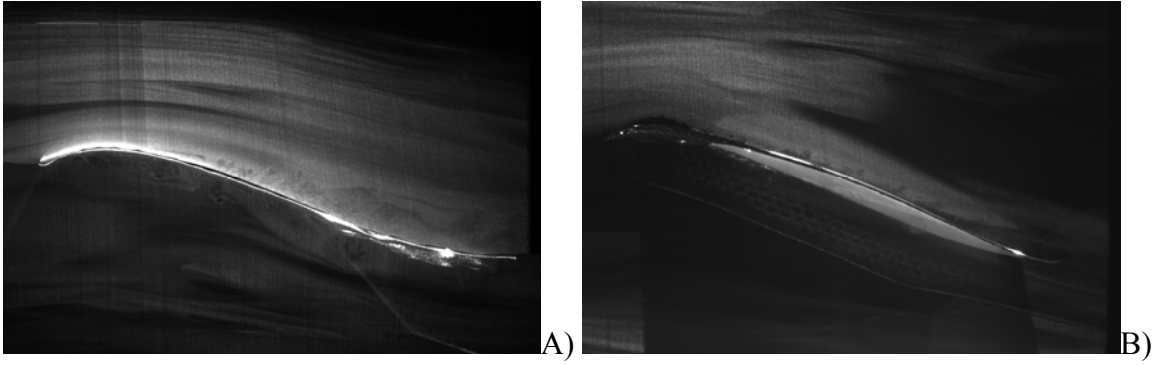


Figure 4-39. Pulsed laser flow visualization of rigid (A) and PR (B) wings at AOA of 12° and V of 10 m/s.

CHAPTER 5 CONCLUSION

Wind Tunnel Survey Conclusion

The flow quality and velocity profiles were determined for both test sections of the Engineering Laboratory Design wind tunnel. The small test section had global root mean square (RMS) turbulence intensities less than 0.07 % over much of the available area at micro air vehicle (MAV) flight speeds. The turbulence grew with increases in velocity, but the data at higher velocities was not to be trusted due to rapid changes in tunnel temperature. The large test section had turbulence intensities less than 0.12 % for much of the available area at MAV flight speeds, but the test section had a very large boundary layer which reduced the core flow area to nearly the size of the small test section.

The tests performed at higher velocities were subject to rapidly increasing test section temperatures which certainly introduced error into the measurements. If turbulence and velocity information is desired for higher speeds, then the experiment should be repeated after an adequate cooling system has been installed. The large test section has limited usefulness due to its large boundary layer. Methods should be attempted to decrease the boundary layer growth along the straight walled diffuser.

Flow Visualization Conclusion

The rigid, batten reinforced (BR), and perimeter reinforced (PR) wings were subjected to multiple wind tunnel tests. The loads data of the rigid wing showed that a sharp change in the flow field exists in the pre-stall angle of attack (AOA) sweep. Oil surface flow visualizations performed on the rigid wing showed that a long laminar

separation bubble is present across the top surface of the wing at low AOA. Increasing AOA causes the flow field to change so that a short laminar separation bubble forms off the leading edge (LE). The oil surface flow visualization method was shown to be effective when applied to the rigid wing at lower AOA, but its effectiveness decreased as the model AOA was increased. A plot of the change in flow regimes over AOA is shown in Figure 5-1. Figure 5-2 shows the nature of each flow regime at the center span of the wing. This method could be used to quickly determine whether or not separation was occurring on MAV wings at low AOA.

The laser flow visualizations clarified the nature of the separation bubbles and wingtip vortices. The PR wing was had early onset of a LE separation bubble, and the bubble was of a different character than the rigid wing's short LE bubble. Future studies of the flow could include a detailed span wise mapping of flow characteristics and a detailed chord wise mapping of wing tip vortex growth. Particle image velocimetry (PIV) was used to attempt to determine pressure distributions over the wing, but future studies will require a three dimensional (3D) PIV system for accurate results. It was clear from the experiments that the flow over a low aspect ratio (LAR) MAV wing is highly 3D, and even the center span region may not be immune to 3D effects due to the substantial separation.

Future Work

It was clear from the experiments that University of Florida (UF) MAVs have issues with separation. The separation can induce extra drag and harm controllability. As MAVs are decreased in size the separation effects will play a larger role in the aircraft aerodynamics. If the effectiveness of conventional turbulators are not sufficient at low Re then other methods must be explored. The PR wing shows promise in that it can

passively create a LE separation bubble of a different nature than the short separation bubble of the rigid wing. Obstacles exist to studying the PR wing using visualization methods, but in time they may be overcome.

MAV wings pulled from a single mold were tested, hence they had the same geometry. It would be of interest to study other wing designs with varying camber and reflex to identify more efficient designs. The UF design may have the separation behavior due to its highly cambered design, or due to the wing shape. The wing shapes were derived from a simple process, however future MAVs need not have such a curved plate wing design.

One possibility for study is the design of the leading edge. The LE could be configured into many shapes and designs to produce desired flow effects. It may be possible to passively trigger a LE separation bubble at low AOA so that the drag from separation may be reduced. The flexible wing design may also be used in a manner which produces a decreased drag. Studies into the lifting wings of MAVs can certainly be applied to create aircraft which fly with more capability and better handling qualities.

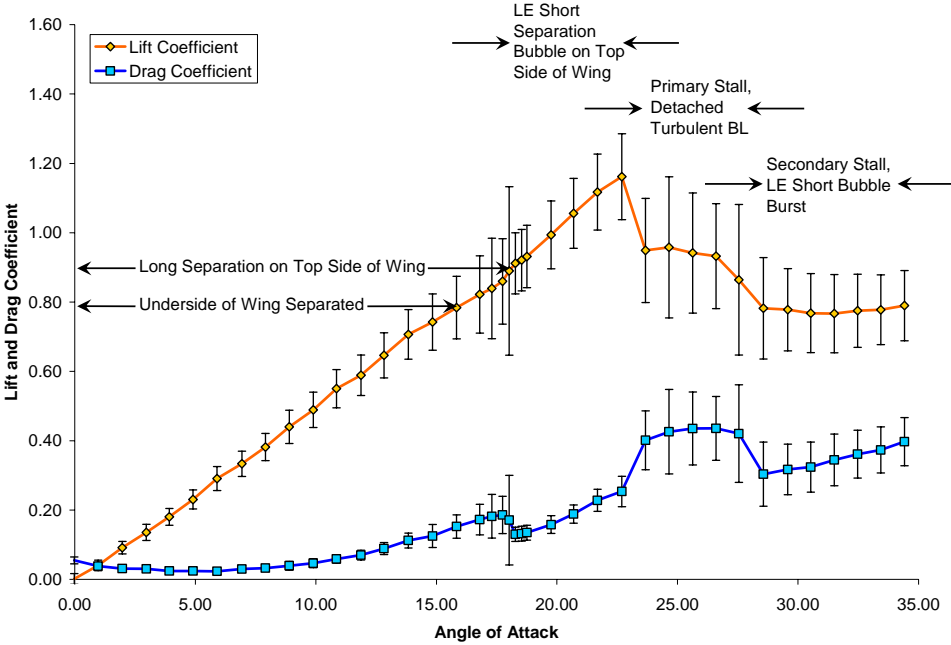


Figure 5-1. Lift and drag coefficient curves with characteristic flow regimes indicated.

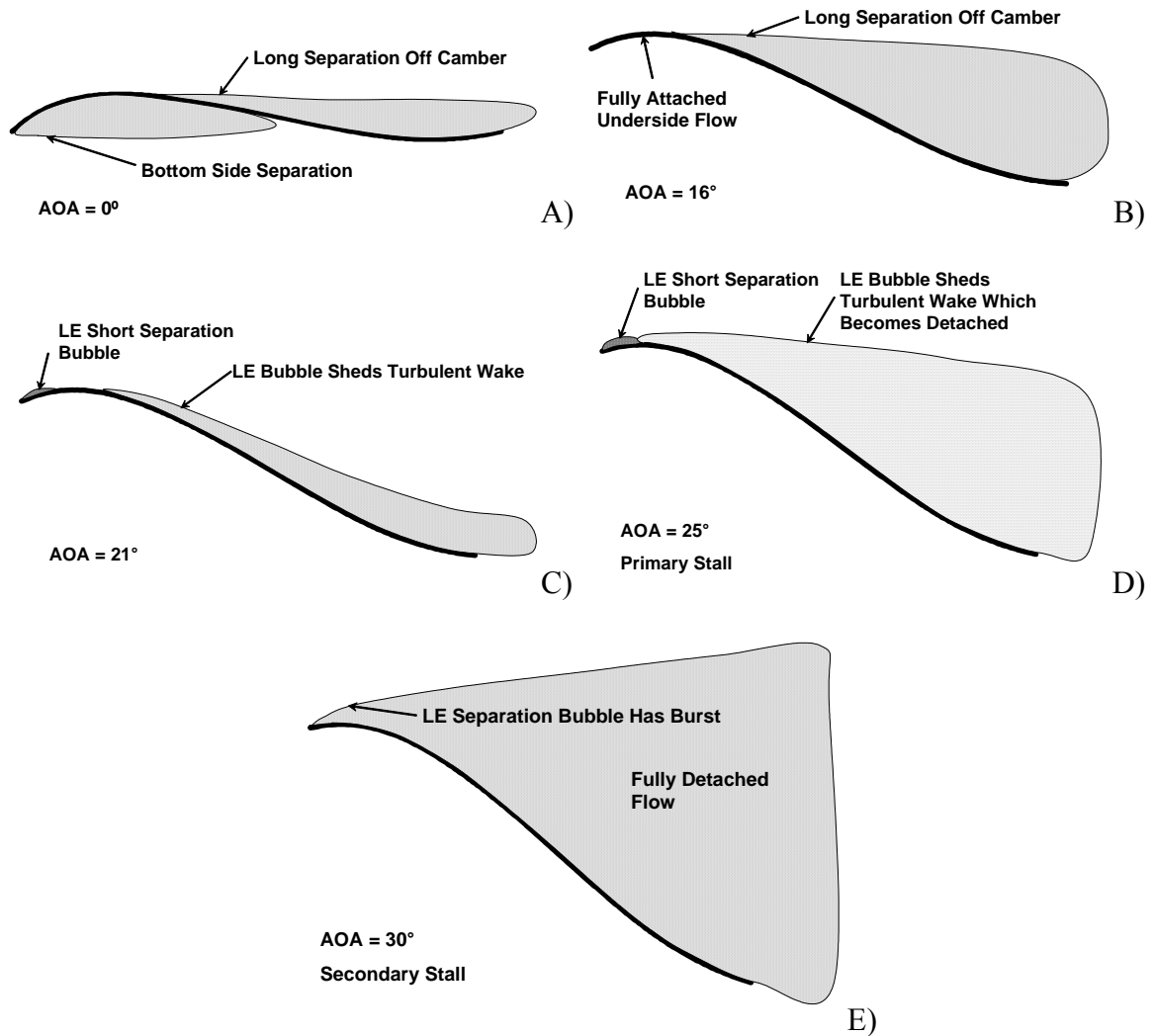


Figure 5-2. Changes in air flow patterns along center span based off of laser based flow visualization. A) Long and bottom side separation, B) Long separation only, bottom side attached, C) Formation of short LE separation bubble which sheds turbulent wake, D) LE short bubble sheds detached turbulent wake, E) LE bubble is burst and flow is fully detached from surface.

APPENDIX A
HIGH SPEED WIND TUNNEL CHARACTERIZATION

This appendix contains plots indicating the characterization results obtained at a wind tunnel control voltage setting of 5.0 V. This control setting corresponded to an origin velocity of 26 m/s for the large test section and 50 m/s for the small test section. A root mean square (RMS) method of determining turbulence was used to prepare the turbulence plots.

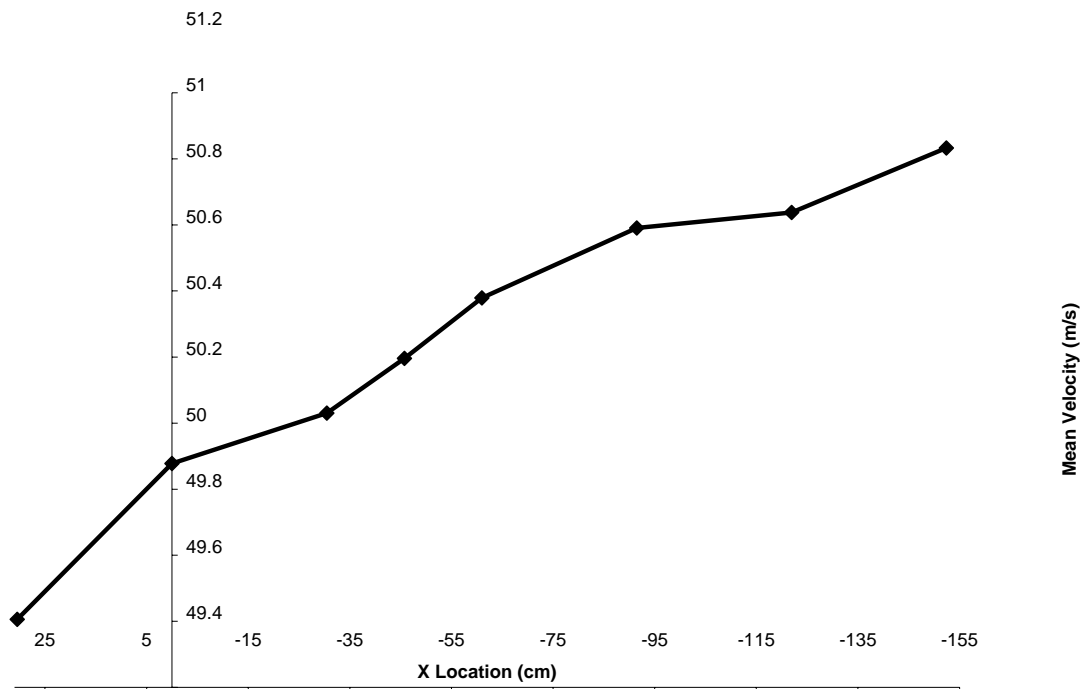


Figure A-1. Centerline mean velocity variation across X.

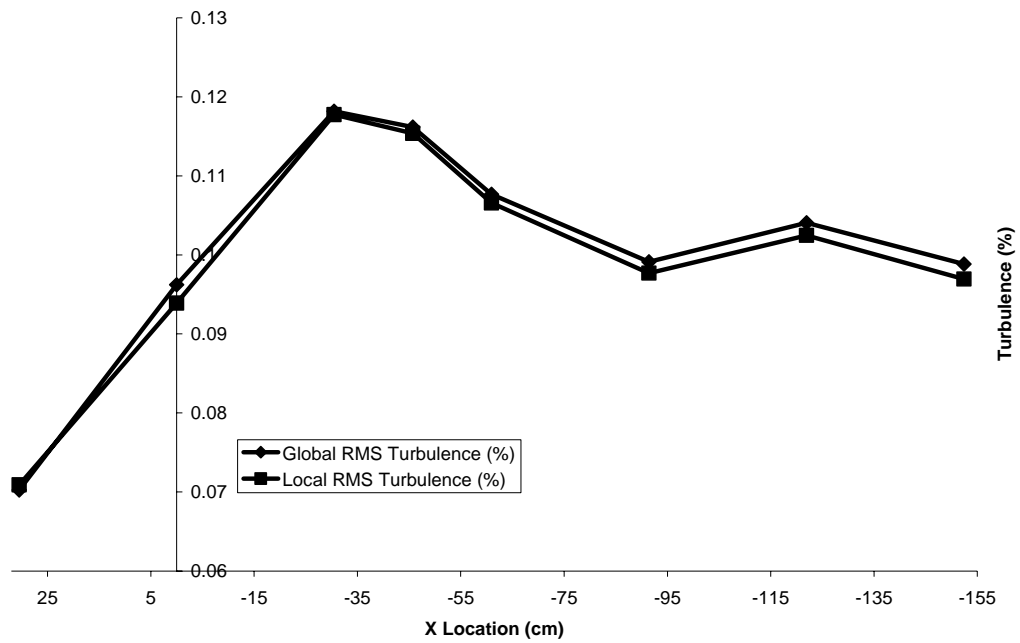


Figure A-2. Centerline turbulence variation across X.

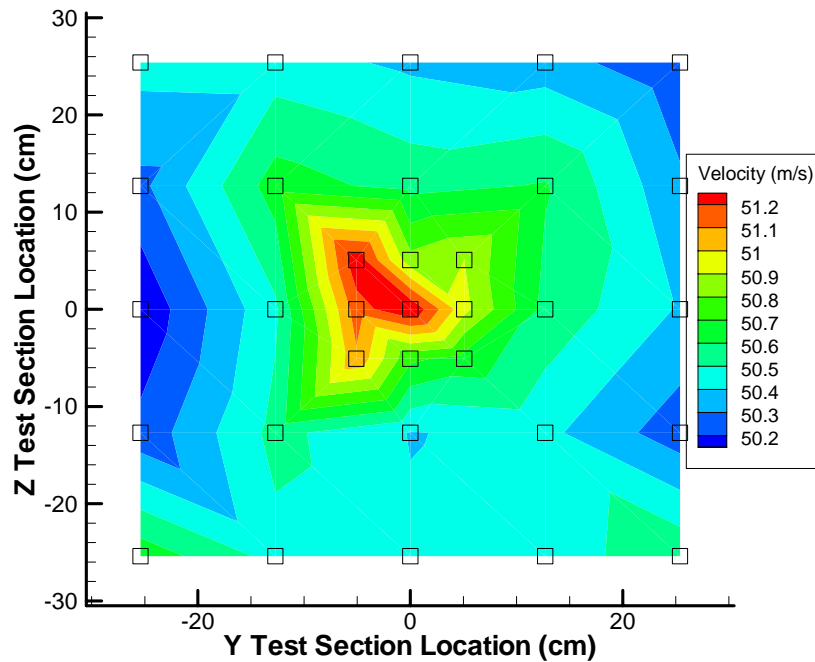


Figure A-3. Velocity contour across test section at $X = 0$ m and $V = 51$ m/s. Black squares are data sampling locations.

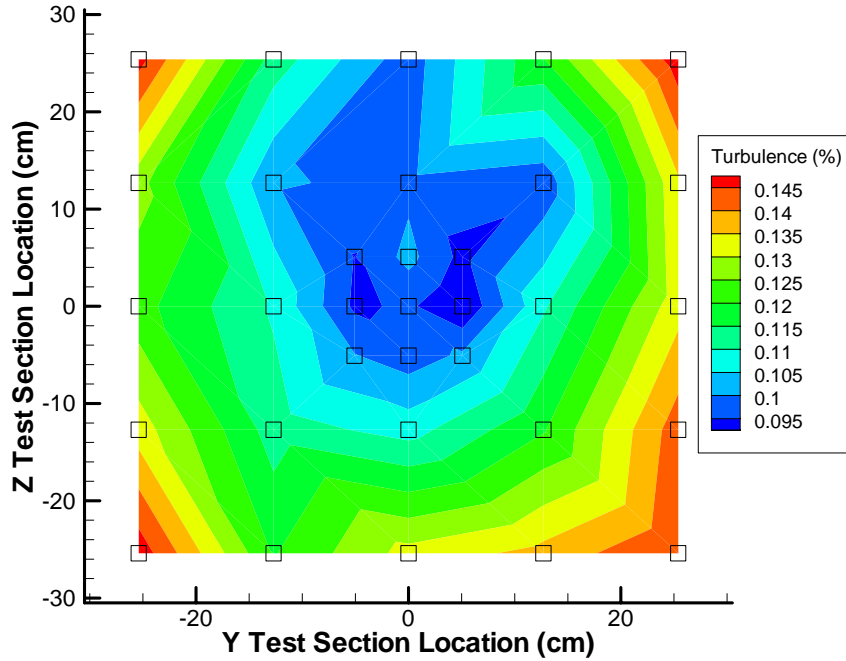


Figure A-4. RMS turbulence contour across small test section at $X = 0$ m and $V = 51$ m/s. Black squares are data sampling locations.

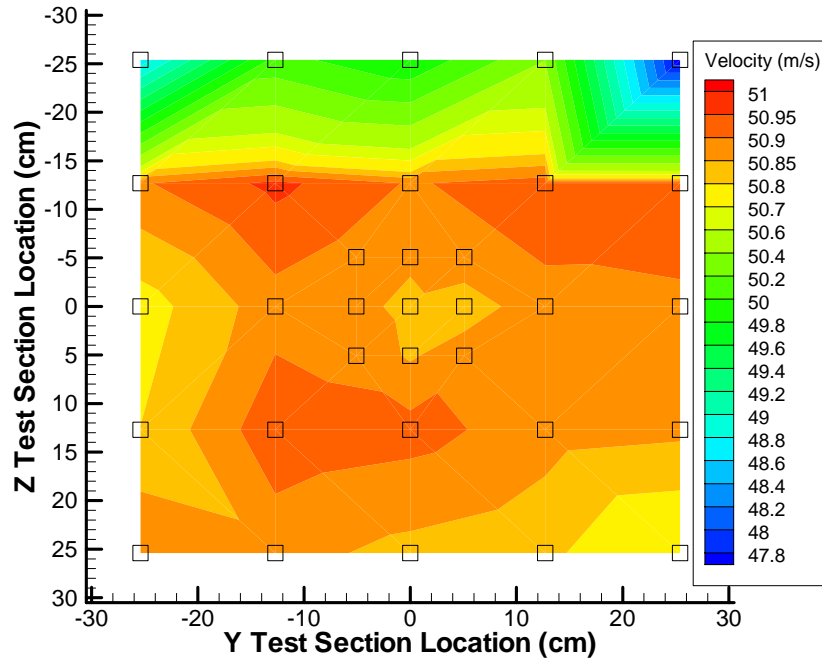


Figure A-5. Velocity contour across test section at $X = -1.22$ m and $V = 51$ m/s. Black squares are data sampling locations.

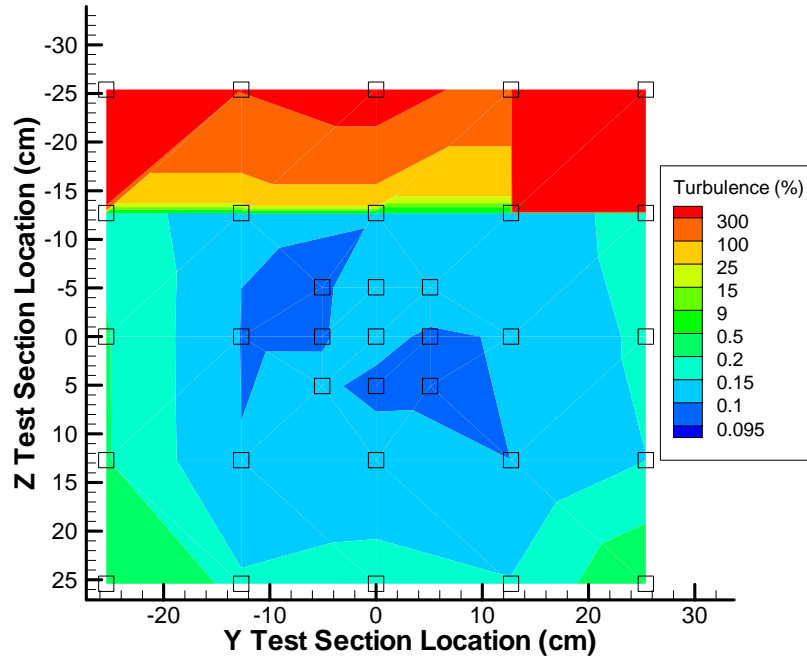


Figure A-6. RMS turbulence contour across small test section at $X = -1.22$ m and $V = 51$ m/s. Black squares are data sampling locations. Possible errors present in top corners.

Large Test Section Results

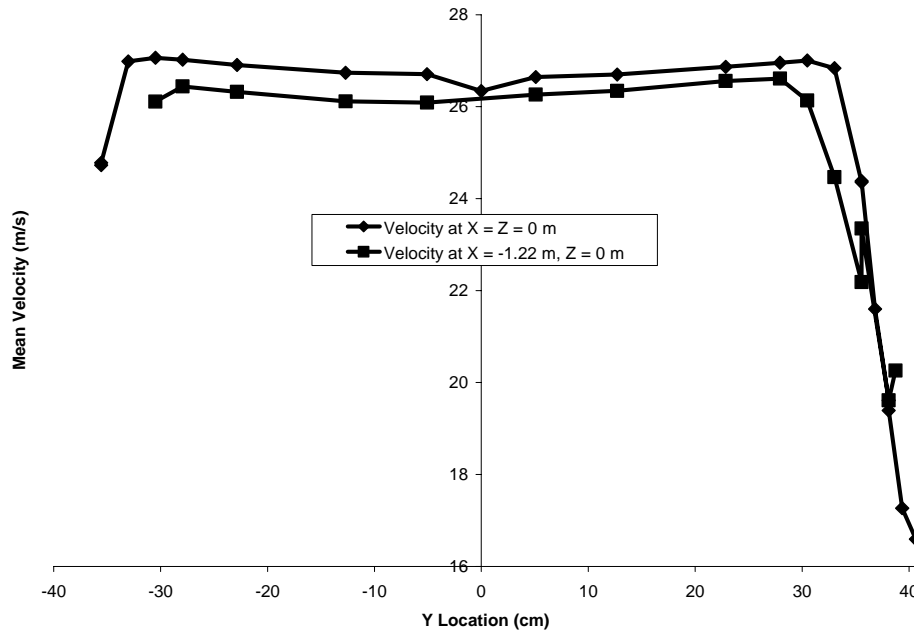


Figure A-7. Variation of velocity across Y direction for $(0,0,0)$ velocity of 26 m/s, $Z = 0.0$ m, $X = 0.0, -1.22$ m

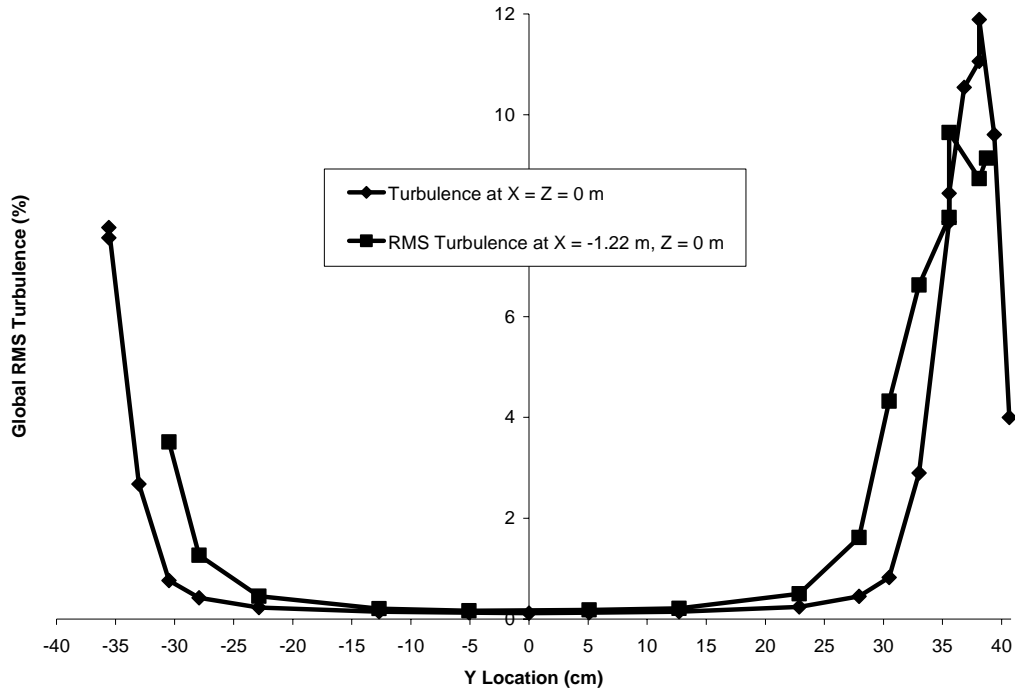


Figure A-8. Variation of global RMS turbulence across Y direction for (0,0,0) velocity of 26 m/s, Z = 0.0 m, X = 0.0, -1.22 m.

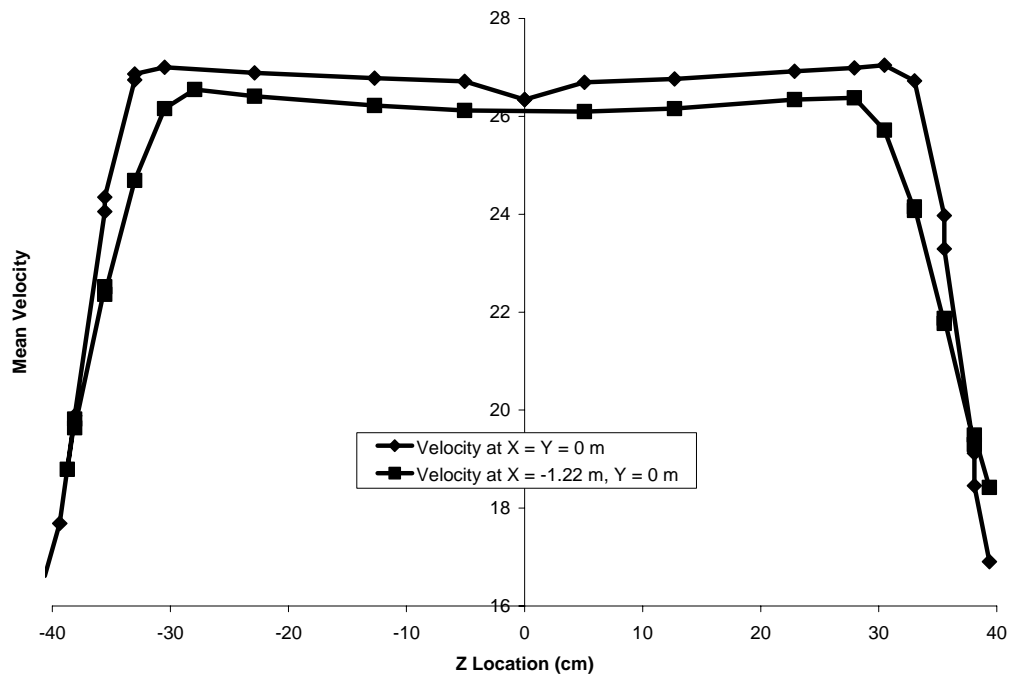


Figure A-9. Variation of velocity across Z direction for (0,0,0) velocity of 26 m/s, Y = 0.0 m, X = 0.0, -1.22 m.

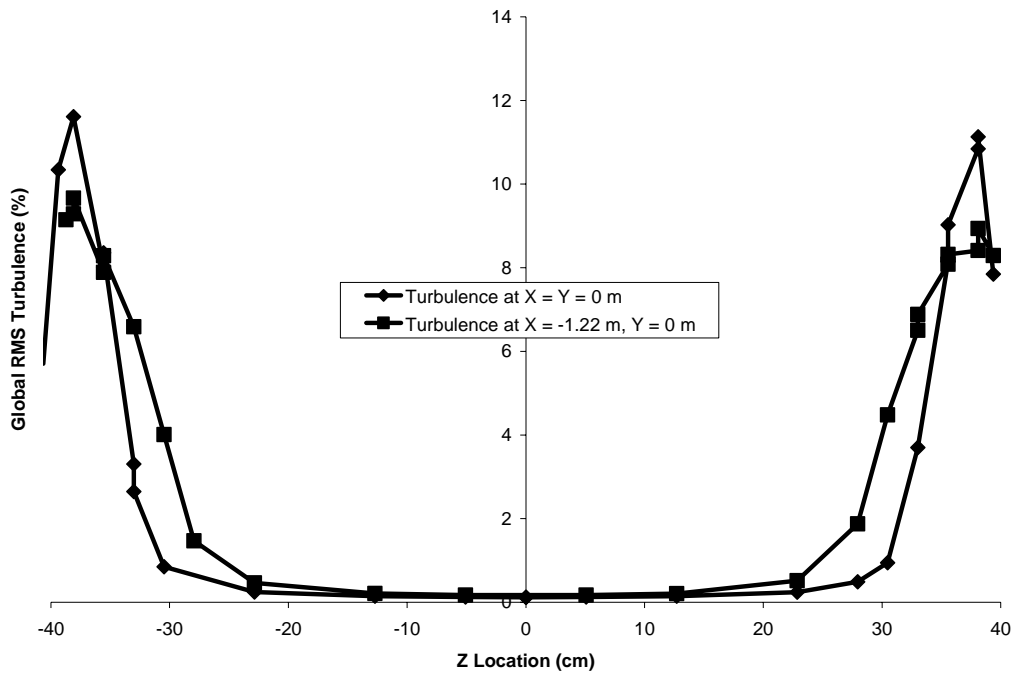


Figure A-10. Variation of global RMS turbulence across Z direction for (0,0,0) velocity of 26 m/s, Y = 0.0 m, X = 0.0, -1.22 m.

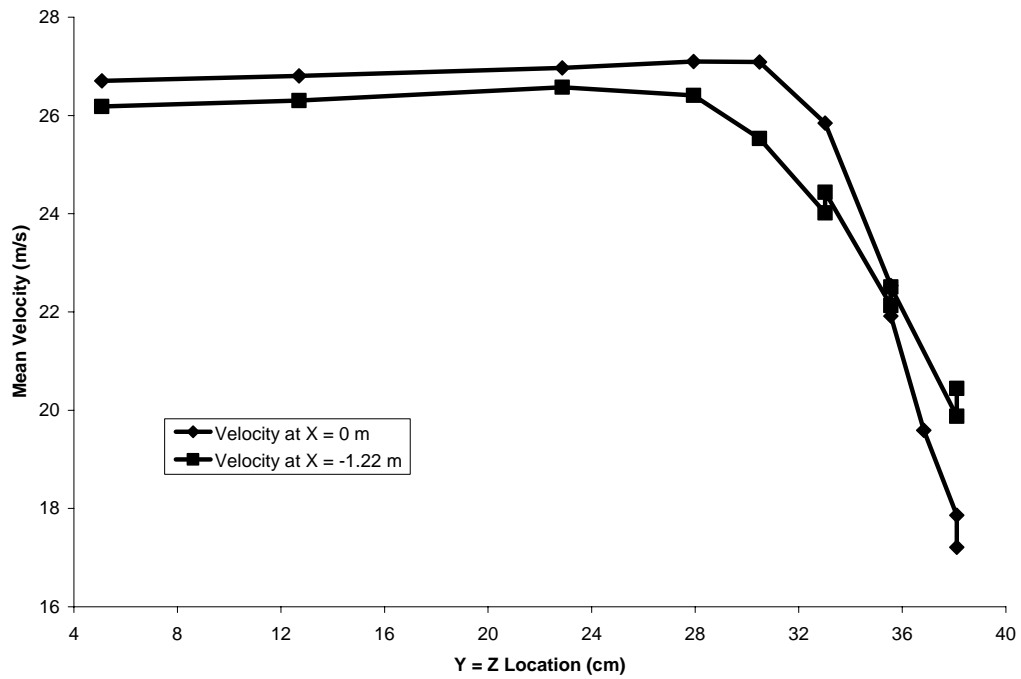


Figure A-11. Variation of velocity across Y = Z direction for (0,0,0) velocity of 26 m/s, X = 0.0, -1.22 m.

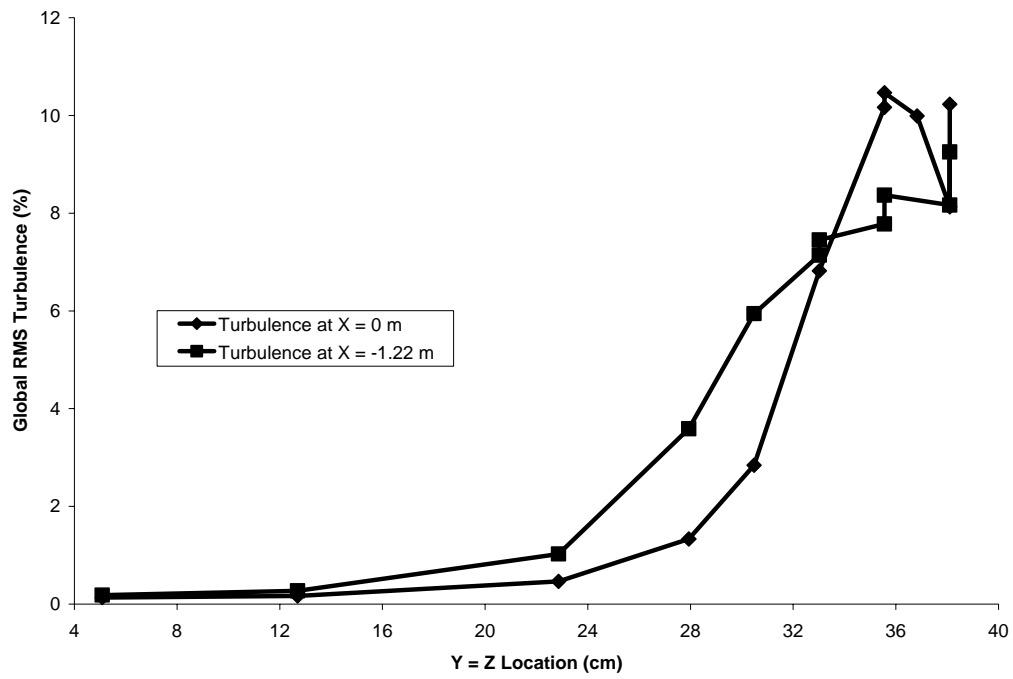


Figure A-12. Variation of global RMS turbulence across Y = Z direction for (0,0,0) velocity of 26 m/s, X = 0.0, -1.22 m.

LIST OF REFERENCES

1. Mueller, T. J., DeLaurier, J. D., "Aerodynamics of Small Vehicles," Annual Review of Fluid Mechanics, Vol. 35, 2003, pp. 89-111.
2. Mueller, T. J., "Aerodynamic Measurements at Low Reynolds Numbers for Fixed Wing Micro-Air Vehicles," Special Course on Development and Operation of Unmanned Air Vehicles for Military and Civil Applications, Von Karman Institute, Belgium, September 1999.
3. Albertani, R., Boria, F., Bowman, S., Clanton, D., Crespo, A., Francis, C., Ifju, P., Johnson, B., Lee, K., Morton, M., Sytsma, M., "Development of Reliable and Mission Capable Micro Air Vehicles," 2005 International Micro Air Vehicle Competition, Konkuk University, Seoul, South Korea, May 2005.
4. University of Florida Micro Air Vehicle Team "University of Florida Competition Micro Air Vehicles," 2002 International Micro Air Vehicle Competition, Brigham Young University, Provo, Utah, May 2002.
5. Claxton, D., Johnson, B., Stanford, B., Sytsma, M., "Development of a Composite Bendable-Wing Micro Air Vehicle," 2006 International Micro Air Vehicle Competition, Brigham Young University, Provo, Utah, May 2006.
6. Carmichael, B. H., "Low Reynolds Number Airfoil Survey": Vol. 1, NASA CR 165803, Nov. 1981.
7. Albertani, R., "Experimental Aerodynamic and Static Elastic Deformation Characterization of Low Aspect Ratio Flexible Fixed Wings Applied to Micro Aerial Vehicles," Ph.D. Dissertation, Department of Mechanical and Aerospace Engineering, University of Florida, Gainesville, FL, December 2005.
8. Lian, Y., Shyy, W., "Three-Dimensional Fluid-Structure Interactions of a Membrane Wing for Micro Air Vehicle Applications," AIAA Paper 2003-1726, April 2003.
9. Pelletier, A., Mueller, T. J., "Low Reynolds Number Aerodynamics of Low-Aspect-Ratio Thin/Flat/Cambered-Plate Wings," Journal of Aircraft, Vol. 37, No. 5, September-October 2000. pp. 825-832.
10. O'Meara, M. M., Mueller, T. J., "Laminar Separation Bubble Characteristics on an Airfoil at Low Reynolds Numbers," AIAA Journal Vol. 25, No. 8, August 1987, pp1033-1041.

11. Mueller, T. J., "The Influence of Laminar Separation and Transition on Low Reynolds Number Airfoil Hysteresis," *Journal of Aircraft*, Vol. 22, No. 9, September 1985. pp. 763-770.
12. Muti Lin, J. C., Pauley, L. L., "Low Reynolds-Number Separation on an Airfoil," *AIAA Journal* Vol. 34, No. 8, August 1996. pp 1570-1577.
13. Selig, S. M., Gugliermo, J. J., Broern, A. P., Giguere, P., "Experiments on airfoils at low Reynolds numbers," *AIAA Paper* 96-0062, January 1996.
14. Lyon, C. A., Selig, M. S., Broeren, A. P., "Boundary layer trips on airfoils at low Reynolds numbers," *AIAA Paper* 97-0511, Jan. 1997.
15. Gopalarathnam, A., Et. Al., "Design of Low Reynolds Number Airfoils with Trips," *Journal of Aircraft*, Vol. 40, No. 4, July-August 2003. pp. 768-775.
16. Lian, Y., "Membrane and Adaptive-Shaped Wings for Micro Air Vehicles," Ph.D. Dissertation, Department of Aerospace Engineering, University of Florida, Gainesville, FL, August 2003.
17. Mathew, Jose, "Design, Fabrication, and Characterization of an Anechoic Wind Tunnel Facility," Ph.D. Dissertation, Department of Mechanical and Aerospace Engineering, University of Florida, Gainesville, FL, May 2006.
18. Oppenheim, A. V., Schafer, R. W., *Discrete-Time Signal Processing*, (2nd Ed.), Prentice Hall, New Jersey, 1999, pp. 83-91.
19. Taylor, G. I., "Statistical Theory of Turbulence," Introduction and summary of parts I-IV, July 4, 1935, pp. 421-446 of *Proceedings of the royal society of London, Series A, Mathematical and Physical Sciences*, Vol. 151, No. 873, 1935.
20. Panton, R., *Incompressible Flow*, (4th Ed.), John Wiley and Sons, Inc., New Jersey 2005, pp. 353.
21. Naughton, J. W., "Wall Shear Stress Measurements on the NASA Hump Model for CFD Validation," *AIAA Paper* 2004-2607, June 2004.
22. Naughton, J. W., Viken, S., Greenblatt, D., "Skin-Friction Measurements on the NASA Hump Model," *AIAA Journal*, Vol 43, No. 6, 2005.
23. Huang, H., Dabiri, D., Gharib, M., "On errors of digital particle image velocimetry," *Measurement Science and Technology*, Vol. 8, September 1997. pp. 1427-1440.
24. Westerweel, J., "Fundamentals of digital particle image velocimetry," *Measurement Science and Technology*, Vol. 8, August 1997. pp. 1379-1392.

25. Raffel, M., Willert, C., Kompenhans, J., *Particle Image Velocimetry: A Practical Guide*, (1st Ed.), Springer, New York, 1998, pp 62-121.
26. Melling, A., "Tracer particles and seeding for particle image velocimetry," *Measurement Science and Technology*, Vol. 8, October 1997. pp. 1406-1416.

BIOGRAPHICAL SKETCH

Mike Sytsma was born in the then-little town of Homestead, Fl. His parents built a cute little brick house out in the country and life was good. He was always taking things apart, experimenting with science stuffs, and sticking his head where he didn't belong. In second grade he made a solar powered car from popsicle sticks. In third grade he had a short lived experiment with homemade gunpowder. In fourth grade he nearly electrocuted himself to death experimenting with a lightning generator he built, and then his parents took all his fun science toys from him.

That summer between fourth and fifth this tiny but strong hurricane named Andrew blew everything away in Homestead. The little town was devastated and everything was destroyed. The house Mike lived in survived as did the avocado grove, but life was tough. Mike was sent away by his parents while they fixed the house, and two months later he was enrolled in a school in Homestead. The schools were pretty terrible due to the crowded facilities and lack of electricity and air conditioning, and his learning lagged greatly. In sixth grade his parents put Mike into Princeton Christian Middle School, and Mike got a strong background in math and English there. It was his time in Princeton that Mike started to learn the world of the IBM computer. No longer bound to the 30 Kb of available RAM the Commodore 64 had, Mike experimented with programming and operating systems. It wasn't long before he tired of Microsoft's poor entry into the market and reached out to Linux in the era of the 2.0.34 kernel. He learned Linux to the fullest extent of command based control and was master of his network domain.

High school was great for Mike, he went to the School for Advanced Studies at Miami Dade Community College. He started school at 10 AM and did college classes until 2 PM, at which time he went to high school classes. The freedom allowed him to have fun and socialize and get out with 70 credits, a 4.0 college GPA, and a National Merit Scholarship.

Mike started his college career in Fall of 2000 and had quite a few difficulties adjusting to college life. He had an aborted attempt at fraternity life with Tau Kappa Epsilon which went bankrupt over spring break 2001 and kicked him and all the other members to the curb. Mike spent another year struggling through sophomore classes until summer 2002 when he learned to sail. Mike sailed 3 to 5 days a week, Mike sailed in no wind and full wind, Mike sailed fast and he sailed slow, Mike sailed and sailed until the Lake Wauburg employees made him go. That's when Mike got the bug, and he didn't have much time to sail during the school year, but he remembered fun sailing.

Another year of school and he was doing better. He got a job working in a wind tunnel lab with fancy things like lasers, lenses, accelerometers, OOH my! What fun it was. Summer 2003 was a fun time, Mike actually had money for the first time so he set about building a boat. He chose the plans for a cute 12' boat he could build in the living room of his apartment, and he set right to work. After his 40 hr/week working in the machine shop and lab, he would come home and put in another 40 hr/week constructing *Wicked Wind*. Within 6 weeks he had her woodwork completed, and a month later was her first sail. Mike kept working on that boat bringing her improvements and sails and spars and shiny hardware, but alas sailing her just wasn't as fun as he had hoped.

Senior year of school, Mike had a cute engineer girlfriend and he got involved in even more projects. His biggest and most fun bit of work was Redbull Flugtag, and Mike led a team of 12 engineers to build a 28' span, 4' chord flying alligator on a shoestring budget. They built the big gator in 4 weeks, and went down to Miami to compete but were blown out by hurricane weather. Mike went back to school to get involved in Design Build Fly, but when competition time came he opted to go for Flugtag, round II. The UF team made a heck of a showing, but did not place due to political difficulties (the judges were UM fans).

Mike worked that summer after graduating to build the turning vanes for the new anechoic aeroacoustic wind tunnel. He then started research on MAV wing aerodynamics using his PIV skills and tenacious personality to attack experiments and to try and find meaning amidst seas of data. He was tasked to write the IMAVC paper and got a chance to travel to S. Korea which was super cool and they won first place, then he spent the rest of the summer sailing his little boat and working in the wind tunnel.

His second year he had saved up enough money to buy himself a mighty jewel, *Sapphire*, a 22' Catalina sailboat. *Sapphire* required all Mike's love, time and money which he freely gave. Mike had many fun trips on *Sapphire*, and she enjoyed it too.

Over spring break 2006 Mike had his first job interview in the panhandle, so he dragged *Sapphire* out there to have some windy fun and try to get a job. Alas, but *Sapphire* perished in a tragic rollover incident. She was the only casualty, aside from Mike's broken heart.

Mike wouldn't be kept down though, he secured the job with the USAF and got an offer from Lockheed Martin also. He quickly located another Catalina 22 that wanted

love and went about repairing *Sapphire II*. He edited the IMAVC 2006 paper which won first place again, and finished up his classes with a good GPA. Life was good.

Mike now looks forward to blasting out of Gainesville to a fantastic sailing location where he plans to save up and buy a bigger sailboat that he can live on with aspirations of world circumnavigation.